

A DIODE LASER SOURCE FOR DIAL METHANE  
MEASUREMENTS IN COAL MINES

Richard K. DeFrez  
B.S., Sonoma State University, Rohnert Park, California, 1980


A dissertation submitted to the faculty  
of the Oregon Graduate Center  
in partial fulfillment of the  
requirements for the degree  
Doctor of Philosophy  
in  
Applied Physics


April, 1985

The dissertation "A Diode Laser Source for DIAL Methane Measurements in Coal Mines" by Richard K. DeFreez has been examined and approved by the following Examination Committee:

---

Richard A. Elliott, Advisor  
Professor

 J. Fred Holmes  
Professor

 Dae M. Kim  
Professor

---

M. A. K. Khalil  
Professor

## ACKNOWLEDGMENTS

I would like to express my gratitude to Dr. Richard A. Elliott for his support and encouragement during my years at the Oregon Graduate Center. He has been both a teacher and friend to me. I also thank Dr. Fred Holmes for his many helpful technical suggestions. Thanks are also due Dr. John Blakemore for getting me started on this project.

Much gratitude is due to the Homer Research Laboratories of Bethlehem Steel Corporation and the United States Bureau of Mines for continuing material support for this project. I particularly wish to thank Walter Egan and Roger Boos for cooperation that has extended over years.

I wish to thank John Hunt and Robert Cary for their skillful technical assistance. Early on in the project Bruce Odekirk helped me define my goals and lately Mark Foster has given me invaluable assistance in achieving them. I want to thank my friend Robin Fautley for her continuing support. As we have worked together, Mark Gesley has helped me in many ways.

To my wife, Toni, and my son, Dan, I dedicate this work. They have been my inspiration to succeed.

## Table of Contents

ACKNOWLEDGEMENTS .....	iii
LIST OF FIGURES .....	vii
LIST OF TABLES .....	xi
ABSTRACT .....	xii
1. INTRODUCTION .....	1
2. THE DIAL TECHNIQUE .....	6
2.1 LIDAR: Fluorescence, Raman Scattering, Absorption .....	7
2.2 Overview of Range Resolved DIAL .....	11
2.3 Prior Uses of DIAL to Remotely Measure Methane .....	14
3. SPECTROSCOPIC CONSIDERATIONS .....	16
3.1 The Near Infrared Spectroscopy of Methane .....	17
3.2 Effects of Other Atmospheric Ingredients on Band Selection .....	19
3.3 Band Selection .....	21
4. InGaAs/InP INJECTION LASERS .....	35
4.1 Laser Fabrication and Physical Form .....	37
4.2 Laser Output Spectral Characteristics .....	40
4.3 Output Polarization .....	43
4.4 Output Beam Spatial Characteristics .....	45
4.5 Laser Threshold, Output, and Efficiency .....	46

4.6	Laser Lifetimes .....	51
4.7	Discussion .....	53
5.	METHANOMETER REQUIREMENTS .....	56
5.1	Federal Regulations .....	56
5.2	Laser Power: Safety Considerations .....	57
5.3	Laser Power: Detection Considerations .....	58
5.4	SNR: Pulse Repetition Frequency Considerations .....	63
6.	SOURCE OPTICAL DESIGN .....	69
6.1	Review of Diode Source Characteristics and the DIAL Requirements .....	69
6.2	External Resonator Diode Lasers .....	70
6.3	Reflective Optics for an External Grating Cavity .....	75
6.4	Aberrations in an Off-Axis Parabolic Cavity .....	79
7.	AN EXTERNAL CAVITY SOURCE .....	87
7.1	Mechanical Construction .....	87
7.2	Antireflection Coating .....	98
7.3	Electronic Construction .....	106
7.4	Source Performance .....	114
	REFERENCES .....	122
	APPENDIX A .....	139
	APPENDIX B .....	144

APPENDIX C .....	147
C.1 Inversion .....	147
C.2 Error Propagation .....	150
APPENDIX D .....	154
D.1 Background Noise .....	154
D.2 Detector Dark Current Noise .....	155
D.3 Signal Shot Noise .....	155
D.4 Load (Johnson) and Amplifier Noise .....	156
APPENDIX E .....	158
APPENDIX F .....	165
VITA .....	173

## List of Figures

2.1 A monostatic LIDAR system. ....	8
2.2 A spatially range-resolved DIAL system. ....	13
3.1 P branch spectral transmittance at a $2\text{cm}^{-1}$ bandwidth. ....	23
3.2 Q branch spectral transmittance at a $2\text{cm}^{-1}$ bandwidth. ....	24
3.3 R branch spectral transmittance at a $2\text{cm}^{-1}$ bandwidth. ....	25
3.4 P branch spectral transmittance at a $1\text{cm}^{-1}$ bandwidth. ....	27
3.5 Q branch spectral transmittance at a $1\text{cm}^{-1}$ bandwidth. ....	28
3.6 R branch spectral transmittance at a $1\text{cm}^{-1}$ bandwidth. ....	29
3.7 P branch spectral transmittance at a $0.2\text{cm}^{-1}$ bandwidth. ....	31
3.8 Q branch spectral transmittance at a $0.2\text{cm}^{-1}$ bandwidth. ....	32
3.9 R branch spectral transmittance at a $0.2\text{cm}^{-1}$ bandwidth. ....	33
4.1 SEM micrograph of a broad area InGaAs/InP laser. ....	37
4.2 SEM micrograph of part of an InGaAs/InP laser facet. ....	38
4.3 Optical output vs. wavelength for a broad area InGaAs/InP laser. ....	41
4.4 Optical output polarization ratio vs. drive current for a broad area InGaAs/InP laser. ....	44
4.5 Near field spatial distribution of optical intensity of a broad area InGaAs/InP laser. ....	47

4.6 Optical output vs. drive current for three broad area InGaAs/InP lasers. ....	49
4.7 Reciprocal external differential quantum efficiency vs. laser cavity length for 84 broad area InGaAs/InP lasers. ....	52
4.8 SEM Micrograph of facet of InGaAs/InP laser after catastrophic failure. ....	54
6.1 Cross-section of the external grating cavity parallel to optic axis of parabolic mirror. ....	78
6.2 Graphic output from ray trace program CAVITY for the off-axis parabolic external grating diode laser cavity. ....	81
6.3 CAVITY generated spot diagram. ....	82
6.4 CAVITY generated spot diagram. ....	83
6.5 CAVITY generated spot diagram. ....	84
6.6 CAVITY generated spot diagram. ....	86
7.1 The dual diode laser external off-axis parabolic mirror grating cavity source. ....	88
7.2 The off-axis parabolic mirror with the diamond-machined surface presented. ....	89
7.3 Technical specification drawing for mirror of Figure 7.2. ....	90
7.4 Surface reflected light vs. scattered angle for the mirror of Figure. 7.2. ....	92



7.5 Perspective drawing of the dual diode laser mount. ....	95
7.6 Detail drawing of the dual diode laser mount. ....	96
7.7 Photograph of that portion of the dual diode mount shown in Figure 7.6. ....	97
7.8 Setup for in situ monitoring of the antireflection coating thickness dur- ing deposition. ....	100
7.9 Optical output vs. time during deposition of a SiO antireflection coat- ing on a Laser Diode Labs LCW-5 diode laser. ....	102
7.10 Optical output vs. time during deposition of a SiO antireflection coat- ing of an InGaAs/InP diode laser. ....	104
7.11 Optical output vs. drive current for an InGaAs/InP diode laser before and after coating with SiO. ....	105
7.12 The wavelength controller and its associated hardware. ....	108
7.13 Timing circuitry for the dual diode laser pulser. ....	111
7.14 One current driver channel of the dual diode laser pulser. ....	112
7.15 An example of the tuning range accessible by the dual diode external cavity. ....	115
7.16 Optical output vs. Fabry-Perot mirror displacement for the dual diode external cavity. ....	117

7.17 An example of optical absorption in methane as a function of wavelength measured by the dual diode laser cavity wavelength controller. .....	119
E.1 Schematic representation of the dual diode laser cavity showing the diode laser circulating guided wave and the grating returned optical mode. .....	159

## List of Tables

3.1 AFCRL Methane Absorption Regions .....	18
3.2 Naturally Occurring Constituents of Air .....	20
3.3 The Composition of Coal Gas .....	20
5.1 Allowable Variations in Scale Reading .....	58

## ABSTRACT

### A DIODE LASER SOURCE FOR DIAL METHANE

### MEASUREMENTS IN COAL MINES

Richard K. DeFreez, Ph.D.

Oregon Graduate Center, 1985

Supervising Professor: Richard A. Elliott

The research reported in this dissertation was directed toward the development of a coal mine methanometer source. The project encompassed two tasks. The first was a study conducted to determine if room-temperature injection lasers could be used as the source for a DIAL methanometer for coal mine applications. As part of that study, prior DIAL measurements of methane were reviewed and the measurement technique was explored in a general way. The absorption spectroscopy of methane was then examined in detail and found to contain an appropriate absorption feature near a wavelength of  $1.65 \mu\text{m}$  provided the spectral width of the light source was approximately  $0.2 \text{ cm}^{-1}$ . As an additional part of the study the operating characteristics of broad area high optical output InGaAs/InP injection lasers were examined. A detailed calculation of the requirements for a diode laser DIAL measurement of methane in a coal mine was then performed. By comparing the observed diode laser properties with the DIAL requirements, it was found that

broad area InGaAs/InP injection lasers were suitable in most respects for coal methane measurements. The exception was the diode laser spectral bandwidth. It was found to be some 400 times too large.

The second task was the design and fabrication of an external grating cavity to reduce the bandwidth of the injection lasers. The optical design of an off-axis parabolic mirror grating cavity was developed. Geometric optics was used to determine the physical parameters for an external cavity which would produce the desired spectral bandwidth of  $0.2 \text{ cm}^{-1}$ . The fabrication and performance of this external resonator source is described. Measurement of the source linewidth showed it to be two to three times larger than the design value. An explanation of the resultant bandwidth based on coupled mode theory is presented. In summary, an external grating cavity for a diode laser was designed, assembled, and tested. It was shown to approximate the optical properties required for a DIAL coal mine methane measurement.

## 1. INTRODUCTION

The presence of noxious and explosive gases in underground mine atmospheres has always posed a serious threat to the well-being of miners. Increases in mining mechanization, particularly since World War II, have enlarged the gas burden facing miners<sup>1</sup>. In the United States, this increased burden has stimulated federal mine-safety legislation<sup>2</sup>. In turn, these same regulations have reduced the productivity gained through mechanization.

Nearly two-thirds of all underground U.S. coal tonnage is extracted using continuous mining machines in room-and-pillar mining operations<sup>1</sup>. As a result of the Mine and Safety act of 1969<sup>2</sup> and various state laws, present practice in the room-and-pillar mine is to stop mining every twenty minutes to measure the concentration of methane gas at one foot from the working face. After the mining machine is withdrawn, temporary roof supports are installed to the working face so that a miner can approach the face and measure the methane concentration with a hand-held catalytic combustion methane detector and/or flame safety lamp<sup>3,4</sup>. When the measurement is completed, the temporary roof supports are removed and the mining machine begins mining again<sup>5,6</sup>. Obviously, this procedure reduces productivity and is in itself a safety hazard as temporary roof supports can well be dangerous.

It has been estimated that remote methane measurements could provide up to a 5 percent improvement in room-and-pillar coal mining productivity<sup>7</sup>. Such a pro-

ductivity increase would represent about 11,000,000 tons of coal annually in the U.S. alone<sup>1</sup>. The ability to make remote methane measurements would also be useful in other underground mines, for example in salt mines.

The need for a remote measurement of methane concentration at the working face of an underground coal mine was identified at Bethlehem Steel Corporation in the spring of 1977<sup>8</sup>. Specifications for a methane measurement instrument were drawn up in 1978 at Bethlehem Steel Corporation's Homer Research Laboratories (HRL), and evaluation of remote gas sensing techniques was begun. That evaluation process included contacting Prof. R. L. Byer, well known in remote detection of pollutants, about the potential use of LIDAR (light detection and ranging) methods. In August of 1978, Prof. Byer wrote<sup>9</sup> that remote methane detection could be achieved by differential absorption LIDAR (DIAL) techniques.

As of 1978, Raman-shifted neodymium glass, Raman-shifted Nd:YAG, and Erbium doped YAG (Er:YAG) were all considered as potentially feasible sources for the stated task. Er:YAG was selected as the simplest of these for experimental work, which was carried out at HRL by the present author in the summer of 1979.

The work at HRL in 1979 demonstrated that methane could be remotely detected and measured in a laboratory, using the DIAL technique, an Er:YAG source, and Mie retroreflection from coal dust<sup>7</sup>. However, the Er:YAG laser is inherently a device of low conversion efficiency, with a theoretical upper efficiency limit of only a few percent<sup>10</sup>. Moreover, a flash lamp driven device (such as the Er:YAG laser used at HRL in 1979) requires high voltages and driving currents. Redesign to satisfy the Federal Code<sup>11</sup> in terms of safety hazards would clearly be difficult.

Fortunately, a different kind of laser source for a wavelength compatible with methane absorption ( $1.65 \mu\text{m}$ ) became realizable at about the time the 1979 HRL study was completed. This alternative is a sophisticated form of semiconductor injection diode laser. Room-temperature injection diode lasers for the "long-wavelength" region from  $1 \mu\text{m}$  to  $1.7 \mu\text{m}$  have been reported only during the last few years<sup>12-18</sup>. Thus a study<sup>19</sup> was initiated by Bethlehem Steel Corporation at the Oregon Graduate Center (OGC) at the end of 1980 to determine the feasibility of using an injection laser as the source in a portable methanometer.

During that 9 month study, it was found that  $\text{In}_{0.53}\text{Ga}_{0.47}\text{As}$  diode lasers could indeed be suitable as a methanometer source if their spectral output could be modified to match the requirements of a DIAL measurement. The study indicated the proper modification could be realized by mounting the semiconductor laser in an external diffraction grating tuned cavity and design parameters for such a cavity were specified.

Subsequently in 1982 Bethlehem Steel Corporation contracted with the U.S. Bureau of Mines (Contract No. H0123031) to build a dual wavelength light source for a proof of concept demonstration in collaboration with the Oregon Graduate Center. This thesis discusses the DIAL measurement requirements, and describes the diode laser characteristics, optical design of the external cavity, and the implementation of the design. The work on the external diode laser cavity source described here is, to this author's knowledge, unique in four ways. First, it is the first planned use of room-temperature diode lasers for a DIAL source. Second, the resonator is the first third-order aberration-free off-axis external cavity diode laser built. Third, the cavity is the first to use diamond-machined optics for an external cavity diode laser. Fourth, it is the first wavelength dispersive external grating diode laser with



closed loop electronic wavelength control capabilities.

The organization of the thesis is as follows. Chapter 2 presents an overview of the DIAL technique for remote sensing. In Section 2.1, DIAL is compared with, and contrasted to, other LIDAR methods. This is accomplished through an explanation of the fundamental LIDAR formula, Equation 2.1. Section 2.2 explores the background of range resolved DIAL and describes its potential application in coal mines. A history of previous attempts to remotely monitor methane is given in Section 2.3.

Chapter 3 deals with the spectroscopic considerations pertinent to a DIAL methane measurement in a coal mine. Section 3.1 describes the near infrared spectroscopy of methane. The potential effects of other atmospheric constituents is presented in Section 3.2. In Section 3.3, the absorption band most appropriate to a room temperature diode laser DIAL measurement is found.

Chapter 4 describes in detail the operating characteristics of the high power diode lasers used on the present project. Section 4.1 explains their fabrication and physical form. Sections 4.2 through 4.4 delineate the laser output: spectral properties, polarization tendencies, and beam spatial characteristics, respectively. The polarization is found to be unusual. Results of experimental lasing threshold and efficiency measurements are presented in Section 4.5. The resulting patterns are contrasted to those of standard diode laser models. Section 4.6 discusses diode lifetimes. A brief explanation of the unusual properties found in Sections 4.3 and 4.5 is attempted in Section 4.7.

The requirements for a diode laser DIAL measurement of methane in a coal mine are presented in Chapter 5. Section 5.1 the applicable federal regulations. Laser safety considerations are discussed in Section 5.2. The detection restrictions

on the laser optical output power and pulse repetition frequency are derived with help from the appendices in Sections 5.3 and 5.4.

Chapter 6 develops the optical design for a dual diode laser external grating cavity methanometer source. A brief summary of the DIAL requirements and diode laser properties presented in earlier chapters is given in Section 6.1. Section 6.2 presents external resonator diode lasers as a means of matching the DIAL requirements with the diode properties. Section 6.3 then discusses the use of reflective optics for an external grating diode laser cavity. Specifically, the application of aluminum off-axis paraboloids is presented as advantageous. In the chapter's last section, 6.4, The optical aberrations of such an off-axis cavity are discussed theoretically through analogy to monochromator theory and through application of a ray-tracing program.

Chapter 7 describes the construction and performance of a dual diode source. Section 7.1 explains the source mechanical construction. Section 7.2 lays out the antireflection coating process used to decouple the diode laser from its normal oscillating modes. In Section 7.3, the cavity electronic components are described. The last section, 7.4, shows the source performance.

The final chapter, Chapter 8, summarizes the preceding pages. In addition, that chapter attempts to point out new techniques using diode lasers that might be applied to remote sensing problems. Specifically, recent work on cleaved-coupled-cavity high optical power phased array diode lasers is discussed as a potential means to achieve the spectrally narrow output necessary for remote measurements of chemical species.

## 2. THE DIAL TECHNIQUE

To satisfy various state and federal regulations, present practice in room-and-pillar coal mines is to stop mining operations to measure methane levels at one foot from the working face. By law, the measurement must occur every 20 minutes. The measurement is made with a hand-held device either extended to the face on a telescoping pole or carried to the face after temporary roof supports are installed. The modern hand-held methane monitor is a far cry from the caged canaries once used to detect high levels of noxious gass, and more certainly, contemporary monitoring techniques are far superior to the ancient practice of sending the "fire-boss" through the mine before each working shift with a flaming torch to burn out any methane accumulations. The present monitoring technology does, however, hamper production and endanger miner safety leading to less than perfect compliance with regulations<sup>20</sup>. Further, some types of gas detection instrumentation currently employed have been used since early in the last century with little or no improvements. The flame safety lamp, for example, has been used to measure methane since 1816. In the last fifteen years there have been several attempts to improve local coal and natural gas measurement methods, <sup>21,4,22,3,23</sup> but until recently there have been no attempts at a truly remote measurement for mines.

A new direction in the process of improving mine methane monitoring was taken in 1978 when specifications for a remote methane measurement instrument

were drawn up at HRL. Researchers at HRL, after a thorough study of available techniques, concluded that the LIDAR method could best be applied in the coal mine environment to remotely detect methane in coal gas.

## 2.1 LIDAR: Fluorescence, Raman Scattering, Absorption

The first uses of lasers for remote sensing were in radar type applications. Consequently, the acronym LIDAR for Light Detection and Ranging was applied to laser ranging systems. The first use of LIDAR, in 1963, located turbidity in the upper atmosphere<sup>24</sup>. Soon thereafter LIDAR sensing techniques took on many new tasks, such as remote pollutant detection. There exist currently three different means of measuring from a single location remote gas concentrations with LIDAR: fluorescence, Raman backscatter, and long path or differential absorption. These three methods have been thoroughly reviewed<sup>25,26</sup>.

All three techniques may be explained and compared by means of the fundamental LIDAR equation<sup>26</sup>.

$$P_r(R) = \left( \frac{\rho}{\pi} \right) K P_o \left( \frac{A}{R^2} \right) e^{-2 \int_0^R \alpha(r) dr} \quad (2.1)$$

where  $P_r$  is the backscattered light signal from a target at range  $R$ ,  $P_o$  is the transmitted power,  $K$  is the optical receiver system efficiency,  $(\rho/\pi)$  is the effective reflectivity of the target,  $A$  is the area of the receiving telescope, and  $\alpha$  is the volume extinction coefficient of the atmosphere traversed by the transmitted and reflected light. Figure 2.1 shows schematically a typical single-ended LIDAR system. In the figure, light is transmitted to a remote location and is backscattered to

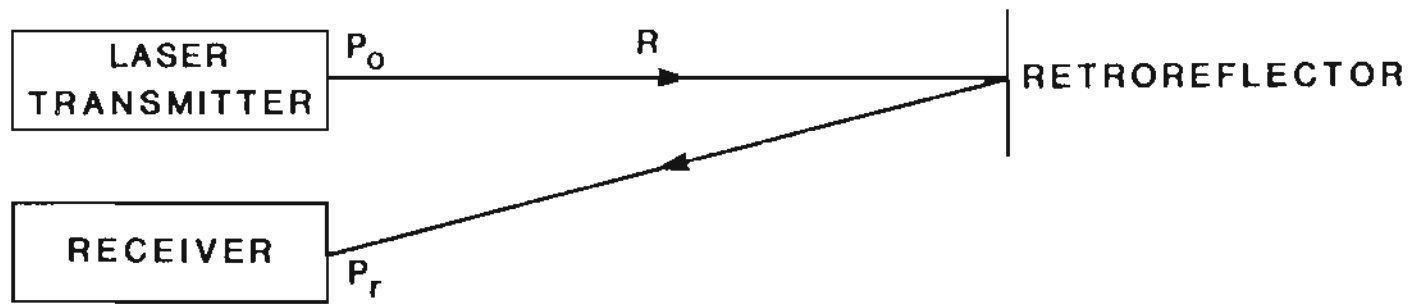


Figure 2.1 A monostatic LIDAR system.

the transceiver. In the case of fluorescence and Raman backscatter, the return signal is scattered by the species to be detected; which is to say,  $\rho$  is proportional to the respective backscatter cross sections. When absorption methods are employed, atmospheric Rayleigh, Mie and/or localized retroreflectors scatter back the transmitted light.

Fluorescence techniques have little use at atmospheric pressures and temperatures. In the application of this method, transmitted laser light excites the remote species to be detected to a higher energy state and subsequently backscattered fluorescence is measured. However, at normal temperatures and pressures rotational state relaxation processes and quenching fluctuations<sup>25</sup> preclude sufficient signal levels ( $\rho$  small) and signal stability ( $\rho$  not well known), respectively.

Conversely, Raman methods have enjoyed some experimental field success. In applications, short wavelength laser light is transmitted to a remote chemical species and the backscattered Stokes radiation is detected. This technique has been used, for example, to measure the temperature and pressure of atmospheric water vapor<sup>27</sup>. Recent reviews of remote Raman methods may be found in the literature<sup>28,29</sup>.

Indeed, Raman backscattering from methane is currently being pursued for potential coal mine applications by the USBM through its Pittsburgh Research Center<sup>30</sup>. In this scheme, 337.1 nm. light from a nitrogen laser is transmitted into a nitrogen and methane atmosphere. The Raman return signals are detected at 365.84 nm. and 373.82 nm., respectively. In practice, the ratio of the methane return signal to the nitrogen (assumed to be of known and constant concentration) return signal is used to calculate the methane density. This system, if employed in a mine, would have the advantage of easily being adapted to other potentially

hazardous gases by a simple replacement of filters in the receiving optics. Additionally, it is advantageous that the Raman technique relies only on the species to be detected for backscattering; consequently, no other backscatter source need be present to create a return signal. Moreover, it is beneficial that Raman LIDAR systems require only a single frequency transmitter, as opposed to a dual frequency source for absorption LIDAR setups.

There are, however, a number of problems that would be encountered by any attempted implementation of such a technique in coal mines. These technical concerns have been outlined previously<sup>31</sup>. The principal probable problems are weak return signals ( $P_r \approx 75$  photons/sec. for methane), potentially explosion inducing high voltages (20 kV in the nitrogen laser), and ultraviolet transmitted light levels near safety limits for eye exposures.

In the absorption mode, LIDAR systems transmit light alternately on and off an absorption wavelength characteristic of and particular to the species to be detected. The return signal from the light transmitted off the absorption line provides a measure of the attenuation due to Mie and Rayleigh scattering along the path. The return signal from light transmitted at the absorption wavelength includes the effect of absorption by the species of interest. The difference in the two signals then yields the effect of absorption alone. Thus, in this mode, a sensitive measure of species concentrations is possible. This is the same as to say  $\alpha_{on} - \alpha_{off}$  from Equation 2.1 can be large; and consequently,  $P_{r_{on}} - P_{r_{off}}$  can be significant. However, in order for  $\rho$  to be large enough for a sufficient signal-to-noise ratio (SNR) at the receiver, it is often necessary for some retroreflector to be introduced into the absorption LIDAR path<sup>32-34</sup>. Fortunately for the potential use of absorption

LIDAR in coal mines large amounts (10-200 mg/m<sup>3</sup>) of coal dust are present near a working face during mining operations. Thus, the location and timing mandated by statute for methane measurements in coal mines would seem to ensure a high value of  $\rho$  in Equation 2.1. This large value of  $\rho$  coupled with the intrinsic sensitivity led Byer to recommend absorption LIDAR to HRL in 1978 as a means to remotely measure coal gas methane<sup>9</sup>.

Absorption LIDAR schemes may be divided into two categories: path averaged and range-resolved. The first category yields the integrated species concentration over the entire light path of Figure 2.1. In this mode, no information about the spatial distribution of the gas is available. The second category gives the desired gas density as a function of one or more spatial coordinates. This distribution may be derived from light time of flight measurements or optical triangulation. To meet the statutory requirement of measurement one foot from the working face, the geometric range resolved method was chosen at HRL in 1978 for experimental work in 1979.

## 2.2 Overview of Range Resolved DIAL

In the same year that LIDAR was first demonstrated, 1963, Schotland<sup>35</sup> measured atmospheric water vapor using range resolved DIAL (RDIAL) and a temperature tuned ruby laser. (An early convention<sup>26</sup> of reserving the acronym DIAL for range resolved absorption LIDAR is now largely ignored in the literature and so shall be here.) During the last decade numerous reports of DIAL experiments have appeared in the literature. The laser systems employed have included CO<sub>2</sub><sup>36-39</sup>, argon-ion<sup>40</sup>, IR optical parametric oscillator<sup>41</sup>, dye<sup>42,43</sup>, dye+SHG<sup>44</sup>, and cryogeni-



cally cooled lead-salt diode lasers (also known as tunable-diode-lasers or TDLs)<sup>45-48</sup> among others. Examples of DIAL review papers may also be found<sup>32,49,50</sup>. Two papers in particular give a theoretical and experimental treatment of RDIAL<sup>32,50</sup>.

As was mentioned in the last section, regulatory requirements necessitate the use of RDIAL for coal mine applications. The fundamental equation for RDIAL is given by Equation 2.1 with:

$$\frac{\rho}{\pi} = \left( \frac{c\tau}{2} \right) \left( \frac{\beta}{4\pi} \right) \quad (2.2)$$

for temporal ranging and

$$\frac{\rho}{\pi} = \left( \frac{\beta\Delta R}{4\pi} \right) \quad (2.3)$$

for spatially resolved ranging, where  $c$  is the speed of light,  $\tau$  is the laser light pulse duration,  $\beta$  is the backscatter coefficient at  $R$ , and  $\Delta R$  is the geometrically determined sample depth as shown in Figure 2.2. The spatial resolution required for methane measurements in coal mines is approximately one foot since law requires measurement at one foot of the face. Thus in temporal ranging

$$\frac{c\tau}{2} < 1 \text{ foot} \quad (2.4)$$

is required. This requirement implies a laser pulse duration of less than 2 ns and is the ranging contemplated for the USBM Raman work described above. With a geometrically determined sample depth, there is no restriction on laser pulse duration; and consequently, smaller detector electronic bandwidths are possible. This latter ranging method was chosen by HRL for the 1979 experimental work mentioned previously. This latter technique is also the one that the 1981 OGC report<sup>19</sup>

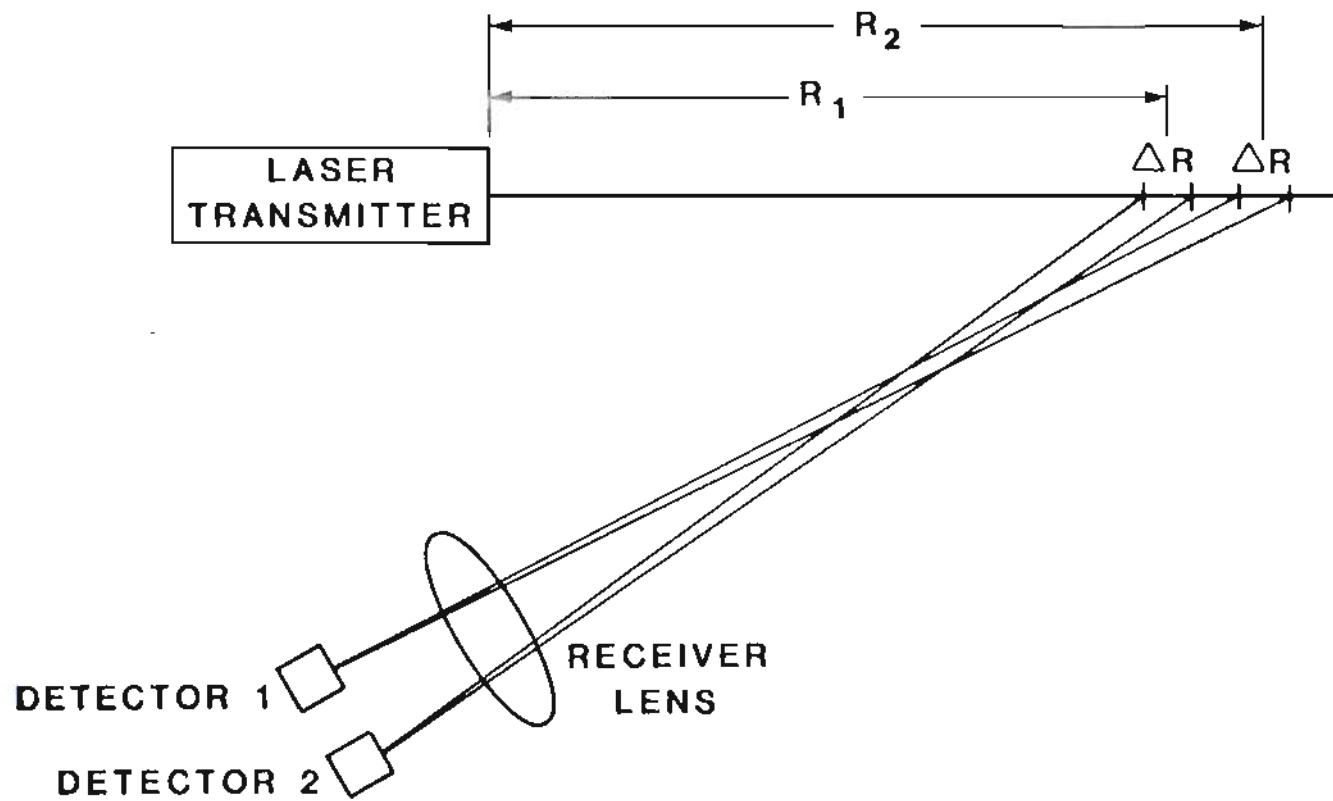


Figure 2.2 A spatially range-resolved DIAL system.

considered for use with diode lasers.

Hence for the work described here, the basic RDIAL equation is given by:

$$P_r(R) = \left( \frac{\beta \Delta R}{4\pi} \right) K P_o \left( \frac{A}{R^2} \right) e^{-2 \int_0^R \alpha(r) dr} \quad (2.5)$$

In this equation

$$\alpha = \alpha_R + \alpha_{MIE} + \alpha_{ABS} \quad (2.6)$$

where  $\alpha_R$  and  $\alpha_{MIE}$  are the Rayleigh and Mie scattering coefficients of the coal mine atmosphere and  $\alpha_{ABS} = N\sigma_{ABS}$  is the molecular absorption coefficient due to a molecular density  $N$  with an absorption cross-section  $\sigma_{ABS}$

In practice, Equation 2.5 must be inverted to solve for  $N$ . This will be discussed in detail in Chapter 5 and in the appendices.

### 2.3 Prior Uses of DIAL to Remotely Measure Methane

Methane is released into the atmosphere by numerous sources. It leaks from natural gas delivery lines, garbage dumps, and water-logged soils. Autos and coal mines spew it. It evolves from animal feces. The global atmospheric concentration is about 1.5 ppmv and is increasing at a rate of 1-2% per year<sup>51</sup>.

The many sources of atmospheric methane have generated considerable interest in attempts to remotely detect the gas. There have been several reports during last decade of successful detection by DIAL methods. The overlap of methane absorption lines with He-Ne and Er:YAG emissions was noted in 1965 and 1972, respectively<sup>52, 53</sup>. Soon thereafter LIDAR techniques were applied. Murray and co-workers at Stanford Research Institute (SRI) used a DF laser and long-path

techniques to demonstrate measurement at  $3.7 \mu\text{m}$ <sup>54-56</sup>. Baumgartner and Byer used a tunable IR optical parametric oscillator to detect methane in the open atmosphere at  $3.39$  and  $1.66 \mu\text{m}$ <sup>57</sup>. Grant and others at the Jet Propulsion Laboratory have developed He-Ne systems for use along gas delivery pipe lines and at garbage dumps<sup>58-60</sup>. Rosengreen and Altpeter have reported on upconversion of  $\text{CO}_2$  light in  $\text{AgGaS}_2$  and  $\text{AgGaSe}_2$  for detection of  $\text{CH}_4$  in the  $3$  to  $3.5 \mu\text{m}$  range<sup>61</sup>. Recently, Chan et al. reported using InGaAsP LEDs to measure absorption in methane at  $1.33 \mu\text{m}$  and  $1.66 \mu\text{m}$  by a method analogous to DIAL<sup>62</sup>.

In 1975, White and Watkins proposed<sup>63</sup> the Er:YAG laser as a remote sensor of methane. Later they conducted long-path absorption experiments with the same device<sup>64</sup>. In 1979, Egan, DeFreez, Boos, and Byer demonstrated the first geometrically range resolved DIAL measurement of methane<sup>65,66</sup>. In their experiments, Er:YAG laser light was Mie backscattered from remotely situated coal dust suspended in a methane and air mixture simulating a working coal mine face. Recently, a transportable Er:YAG RDIAL-MIE backscatter methanometer, built for Bethlehem Steel Corporation (BSC) following the 1979 design, has been successfully demonstrated at a USBM above ground mine simulator and in a BSC under ground working coal mine<sup>67</sup>. The goal of the present project has been to design and build a dual wavelength diode laser light source capable of replacing the Er:YAG source in that methanometer<sup>68,69</sup>.

### 3. SPECTROSCOPIC CONSIDERATIONS

One of the first tasks in the present study was to determine which line or lines of the methane absorption spectrum were most suitable for a diode laser RDIAL methanometer. That determination had to be based on the absorption characteristics of the various methane lines, and on the compatibility of the line wavelengths with the technology of diode lasers. Further, it needed to be based on the absorption characteristics of any other relatively abundant naturally occurring atmospheric constituent or any abundant coal gas component.

Three criteria determine the suitability of absorption lines for a diode laser RDIAL methanometer. First, the line or lines must be within the spectral region accessible to high power diode lasers exhibiting reasonable efficiency and lifetime at or near room temperature<sup>5</sup>. This requirement restricts consideration to injection diode lasers in the near IR<sup>70</sup>. Second, the line or lines must be of appropriate absorption strength, so that the RDIAL measurement process is not impaired either by lack of sensitivity or by excessive attenuation. Based on the experimental work performed at HRL in 1979, an appropriate absorption strength, S, was determined to be between  $10^{-22}$  to  $10^{-21}$  cm/molecule. For a source of better understanding of the somewhat obtuse unit cm/molecule see reference (71). S is proportional to the absorption cross-section per molecule at the absorption line center times the line width. Thus S has units of  $\frac{\text{cm}^2}{\text{molecule}} \times \text{cm}^{-1}$ . Third, the absorption line or lines

must have an effective overlap with other coal mine atmospheric constituents of much less than  $10^{-22}$  cm/molecule. For this criterion, it was assumed that interference from sources other than coal gas, such as diesel exhaust, could be ignored<sup>20</sup>.

The first criterion above limits the spectral region that needs to be examined to the range from 2500 to 12,500  $\text{cm}^{-1}$  (ie. wavelengths from 4  $\mu\text{m}$  down to 800 nm.)<sup>70</sup>. Further, the room temperature condition mentioned above highly favors the shorter wavelength portion of this region<sup>72</sup>. Hence the near infrared (NIR) spectral region holds the most promise for a diode laser RDIAL methanometer.

### 3.1 The Near Infrared Spectroscopy of Methane

Methane is second only to  $\text{H}_2$  in abundance among polyatomic molecules in the solar system<sup>73</sup>. Yet its spectroscopy, particularly in the near infrared, is not well known<sup>74</sup>.

In 1980, as part of the present project, the most comprehensive source of methane absorption parameters, the 1978 AFCRL Atmospheric Absorption Line Parameters Compilation<sup>71,75</sup>, was explored. The compilation was stored on the HRL IBM-370 computer and its NIR region was interrogated by telephone-linked computer analysis from OGC. The analysis yielded three methane absorption regions of potential interest. A total of 1741 absorption lines were identified within these three bands and tabulated below in Table 3.1. In the table, the band assignment was given following the notation of Herzberg<sup>76</sup>.

As has been pointed out, the near infrared spectrum of methane is not well known. Although the AFCRL compilation is the most definitive information available, its contents are lacking. For example, there are many absorption lines

Band Label	Wavelength Range ( $\mu\text{m}$ )	Wavenumber Range ( $\text{cm}^{-1}$ )	Assignment
I	3.16-4.00	3167-2500	$\nu_3$
II	2.34-2.42	4270-4136	$\nu_1 + \nu_4$
III	1.64-1.70	6106-5891	$2\nu_3$

between 5000 and 6000  $\text{cm}^{-1}$  not due to  $2\nu_3$  and not found in the compilation. This is because no systematic absorption measurements have been made in the 1.6-2.0  $\mu\text{m}$  range<sup>74</sup>. As recently as 1983, the  $\nu_2 + 2\nu_3$  band at 1.33  $\mu\text{m}$  was measured<sup>77</sup> apparently for the first time since it was originally characterized in 1933<sup>78</sup>. This band was then used for DIAL-like remote methane measurements using optical fibers and InGaAsP LED's<sup>62</sup>. Maximum absorption coefficients of 0.03  $\text{cm}^{-1}\text{atm}^{-1}$  at 0.05 nm resolution to 0.054  $\text{cm}^{-1}\text{atm}^{-1}$  at 0.3 nm resolution are obtainable at this wavelength depending upon which of the two articles cited<sup>77,62</sup> above is believed. These coefficients are weaker than the absorption obtainable in band III, as will be shown in Section 3.3 with the help of the AFCRL data, and as has been noted<sup>79</sup> recently by Chan et al. Also, Fox recently suggested<sup>80</sup> that laser light absorption in  $\text{CH}_4$  near the 1.645  $\mu\text{m}$  wavelength<sup>68,65,63,53</sup> may be due to  $^{13}\text{CH}_4$  not  $^{12}\text{CH}_4$  as previously suggested<sup>53,81</sup>

Absorption lines with a strength in the range mentioned in the second DIAL criterion above occur in all three bands noted in Table 3.1. However, band I is undesirable because of the requirement of room temperature laser operation. Further, not all bands are equally desirable in other respects, such as the possibility

of interference from other atmospheric constituents.

### 3.2 Effects of Other Atmospheric Ingredients on Band Selection

In addition to the problem that no diode lasers operate in band I at ambient temperatures, the band has other major drawbacks. For example, it encompasses nearly 3100 H<sub>2</sub>O vapor absorption lines, some with strengths up to  $2 \times 10^{-21}$  cm/molecule. Room temperature air at 100% humidity has an H<sub>2</sub>O molecular concentration<sup>82</sup> of some  $6 \times 10^{17}$  cm<sup>-3</sup>. Thus it appears that water vapor alone is enough to preclude band I from use, since the present need<sup>5</sup> is for methane detection down to a concentration of some  $3 \times 10^{16}$  cm<sup>-3</sup>.

Table 3.2 below shows naturally occurring components of air<sup>83,84</sup>. Table 3.3 shows the constituents of coal gas<sup>85</sup>. Of the table constituents, the AFCRL atmospheric absorption tapes show only H<sub>2</sub>O and CO as methane's competitors in band II. CO competition is negligible for the distance range of the present application, since this species does not normally exceed 1 ppm in either the atmosphere or in coal gas.

While some H<sub>2</sub>O lines in band II have a strength approaching  $10^{-21}$  cm/molecule, these have a spectral density smaller than the more intense lines of band I. Also it is possible to find a few methane lines in regions where they are surrounded by water vapor lines of strengths not exceeding  $10^{-26}$  cm/molecule. Consideration of the usual coal gas constituents poses only one other possible problem for band II: that of a conceivably significant abundance of ethane. However, C<sub>2</sub>H<sub>6</sub> has no strong absorption spectra<sup>76</sup> above  $3200$  cm<sup>-1</sup>. Thus band II could be used if an appropriate diode laser were available.



Constituent	Listed in AFCRL Tape	percent	ppm	Absorption NIR Bands I or II
N <sub>2</sub>		78.1		No
O <sub>2</sub>	Yes	20.9		No
CO <sub>2</sub>	Yes	0.03		Yes
Ar		0.9		No
Ne			18	No
He			5	No
Kr			1	No
Xe			0.09	No
H <sub>2</sub>			0.5	No
CO	Yes		0.08	Yes
CH <sub>4</sub>	Yes		2	No
N <sub>2</sub> O	Yes		0.3	Yes
H <sub>2</sub> O	Yes	Varies	Varies	Yes

Constituent	Listed in AFCRL Tape	Maximum Amount Present (Volume %)
CH <sub>4</sub>	Yes	99
C <sub>2</sub> H <sub>6</sub>		1.6
C <sub>3</sub> H <sub>8</sub>		0.05
C <sub>4</sub> H <sub>10</sub>		0.02
C <sub>5</sub> H <sub>12</sub>		< 1 ppm
CO <sub>2</sub>	Yes	14.8
O <sub>2</sub>	Yes	0.5
N <sub>2</sub>		36
H <sub>2</sub>		0.02
He		0.05

It may be noted that until recently no semiconductor diode laser has been available in the spectral region corresponding to band II. However a review of the plots of band gaps and compatible lattice constants in the III-V compound family (see, for example, Thompson (70) or Kobayashi and Horikoshi (86) ) shows that GaSb or InAs could be a binary substrate for lattice matching to AlInAsSb. InGaAsP or InAsPSb quaternary alloys with a bandgap appropriate for band II. A group at the State Rare Metal Research Institute in Moscow has reported work with  $\text{Al}_x\text{Ga}_{1-x}\text{As}_y\text{Sb}_{1-y}$  lasers that are matched to GaSb substrates<sup>87</sup>, but these particular devices provide wavelengths no longer than  $1.8 \mu\text{m}$ . Also, some work on DH InGaAsSb lasers with an emission wavelength near  $2 \mu\text{m}$  has been reported<sup>88</sup>. To this point, work in the United States has concentrated on shorter wavelengths, although reduced Rayleigh scattering in optical fibers may drive future research to longer wavelengths.

Band III is one of the better known methane NIR absorption bands<sup>73,89,90</sup>. The search of the AFCRL data revealed some 150 band III absorption lines of appropriate absorption strength. Competition in this band is provided only by a scattering of  $\text{H}_2\text{O}$  and  $\text{CO}_2$  lines, none of which has strength appreciably exceeding  $10^{-24}$  cm/molecule. Thus band III has desirable spectroscopic properties for a RDIAL methanometer.

### 3.3 Band Selection

Selection of band III for further study was based on the absorption characteristics described in the previous section and the technology of diode lasers. At the time of the selection several groups had reported epitaxial growth of room tempera-

ture injection diode lasers in the wavelength range of 1.6 to 1.7  $\mu\text{m}$ <sup>12,15 14,16</sup>. The devices were made with ternary or quaternary alloys in the  $\text{In}_x\text{Ga}_{1-x}\text{As}_y\text{P}_{1-y}$  system lattice matched to InP. It however remained to be seen whether DIAL measurements of band III methane lines were compatible with the performance characteristics of this type of diode laser.

First it was necessary to examine the methane absorption lines of band III in greater detail. The emission of a moderate to high power pulsed diode laser typically has a full width half maximum (FWHM) spectral bandwidth of several wavenumbers<sup>70</sup>. So, computer-calculated light transmittance curves were generated for the P, Q, and R branches of the  $2\nu_3$  methane absorption band, assuming a 2  $\text{cm}^{-1}$  laser bandwidth. A copy of the source program used in generating the curves may be found in Appendix A.

The P, Q, and R branches correspond to the spectral sub-regions 5890-5995, 5998-6005, and 6010-6107  $\text{cm}^{-1}$  respectively. The necessary line absorption strength information was digitally filed from the AFCRL tape at increments of 0.1  $\text{cm}^{-1}$  between 5890  $\text{cm}^{-1}$  and 6107  $\text{cm}^{-1}$ . Transmittance curves were then generated around local transmission minima (i.e. absorption maxima) for a supposed  $\text{CH}_4$  concentration path length product of  $3.2 \times 10^{19}$  molecules/ $\text{cm}^2$ . That number was chosen to model a potential coal mine DIAL measurement situation: 0.1%  $\text{CH}_4$  assumed over a 40 ft. path with 2%  $\text{CH}_4$  postulated for the 1 foot of path nearest the working face.

Figures 3.1 through 3.3 show the local minima in the transmittance curves so generated for the P, Q, and R branches of the  $2\nu_3$  band. It may be seen from the figures that no minimum falls below 95% in the entire range. Even though it is

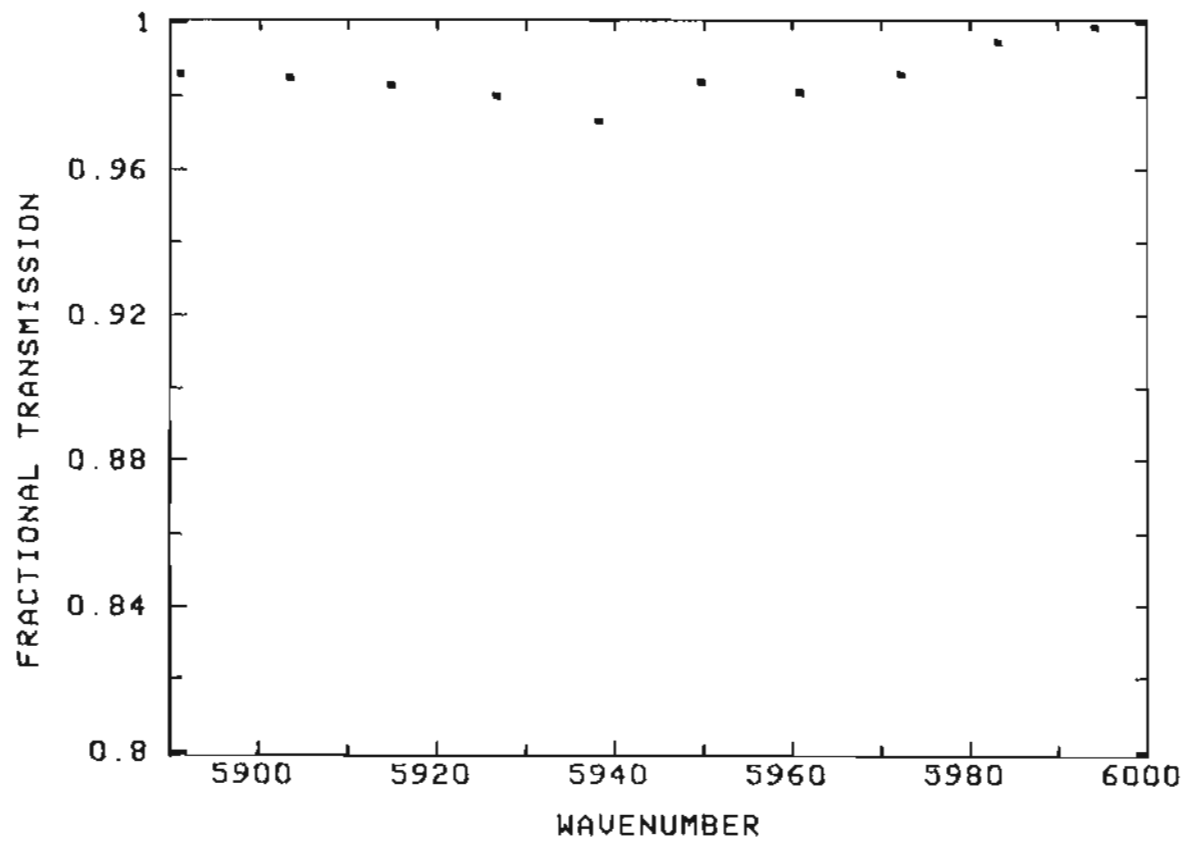


Figure 3.1 Transmittance through 1.2 cm-atm of CH<sub>4</sub> in the P branch of 2ν<sub>3</sub> at a spectral bandwidth of 2cm<sup>-1</sup>.

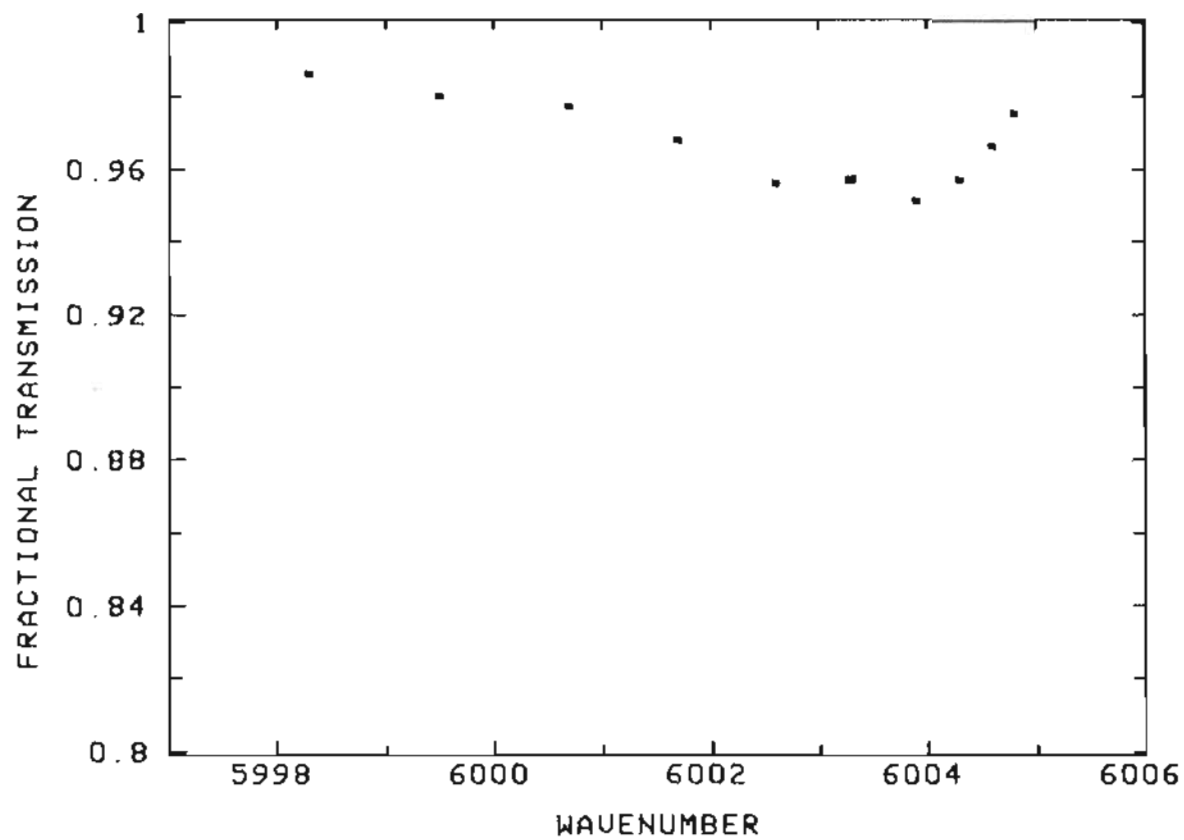


Figure 3.2 Transmittance through 1.2 cm-atm of CH<sub>4</sub> in the Q branch of  $2\nu_3$  at a spectral bandwidth of  $2\text{cm}^{-1}$ .

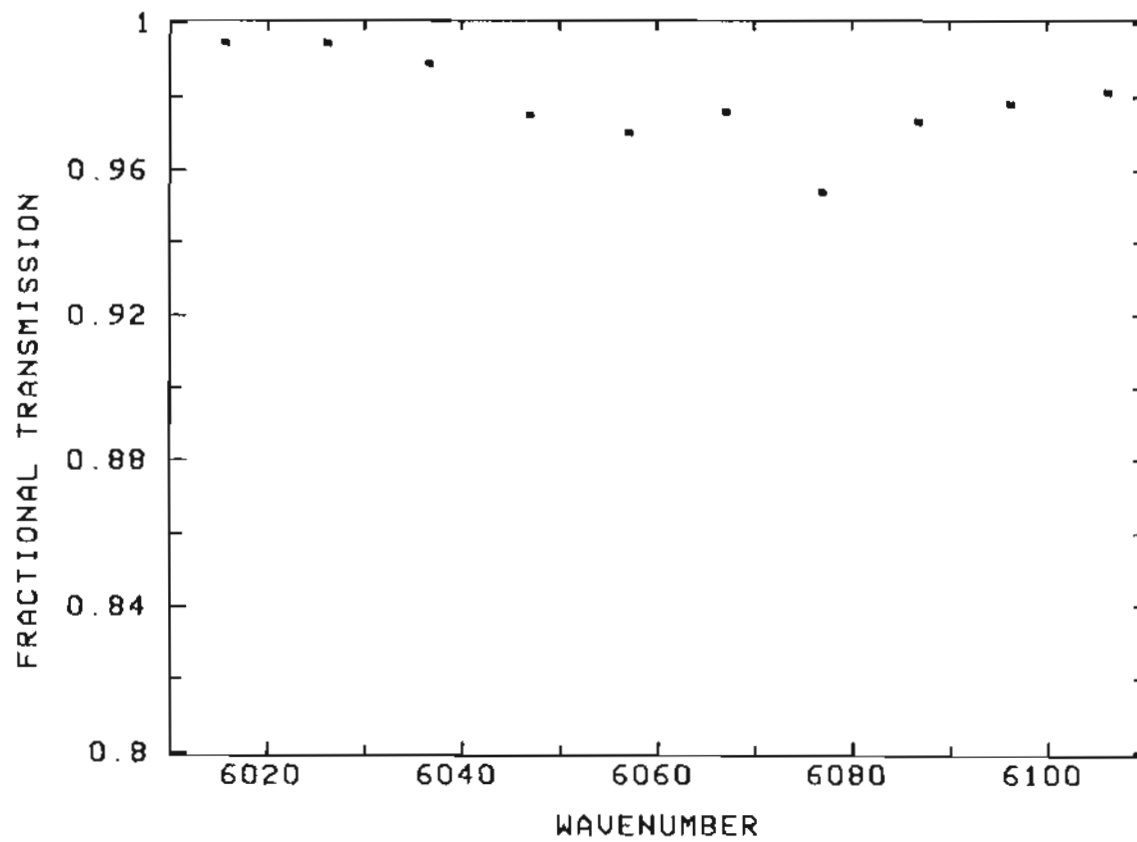


Figure 3.3 Transmittance through 1.2 cm-atm of  $\text{CH}_4$  in the R branch of  $2\nu_3$  at a spectral bandwidth of  $2\text{cm}^{-1}$ .

necessary to know the noise limitations of a proposed DIAL detection system, to determine the optimum absorption cross-section<sup>32</sup>, it is apparent from Figures 3.1 through 3.3 that this cross-section is too small if a 0.1% methane concentration is to be detectable.

Curves were subsequently generated for similar parameters except for the substitution of a  $1 \text{ cm}^{-1}$  laser bandwidth (Figures 3.4 through 3.6) and a  $0.2 \text{ cm}^{-1}$  bandwidth (Figures 3.7 through 3.9). Chan et al.<sup>79</sup> have recently measured the absorption spectra of the  $2\nu_3$  methane band at a resolution of  $1.1 \text{ cm}^{-1}$ . The relative absorption strengths that they measured agree with Figures 3.4 through 3.6 in most respects. The most notable exception is their finding of anomalously large absorption for lines R8, and R9. Byer previously measured<sup>80</sup> the R branch of  $2\nu_3$  at a resolution near  $2 \text{ cm}^{-1}$  and found a much smaller relative strength for these two lines. (It should be noted that the AFCRL tapes used for Figures 3.1 through 3.9 may be in error for line R6 as it appears that duplicate fine structure lines were included at  $6076.954 \text{ cm}^{-1}$  thus causing a somewhat overly large absorption to appear there.) It is interesting to compare the absolute absorption strengths represented in Figures 3.3 and 3.6 with the measured values of references (79) and (90). Chan et al. found the absorption coefficient of R7 to be  $0.07 \text{ cm}^{-1}\text{atm}^{-1}$  at a spectral resolution of about  $1 \text{ cm}^{-1}$ . From Figure 3.6 a coefficient of  $0.038 \text{ cm}^{-1}\text{atm}^{-1}$  may be calculated for the same line. This ratio between the measured and calculated values is also typical to that of most of the other  $2\nu_3$  lines. This may be so because the calculated values include the effects of pressure broadening at atmospheric pressure while Chan et al. measured absorption strengths at 60 torr. Byer measured an absorption strength of  $0.01 \text{ cm}^{-1}\text{atm}^{-1}$  at a resolution of nearly  $2 \text{ cm}^{-1}$  for R7 with 50 torr of methane buffered to atmospheric pressure in  $\text{N}_2$ . On

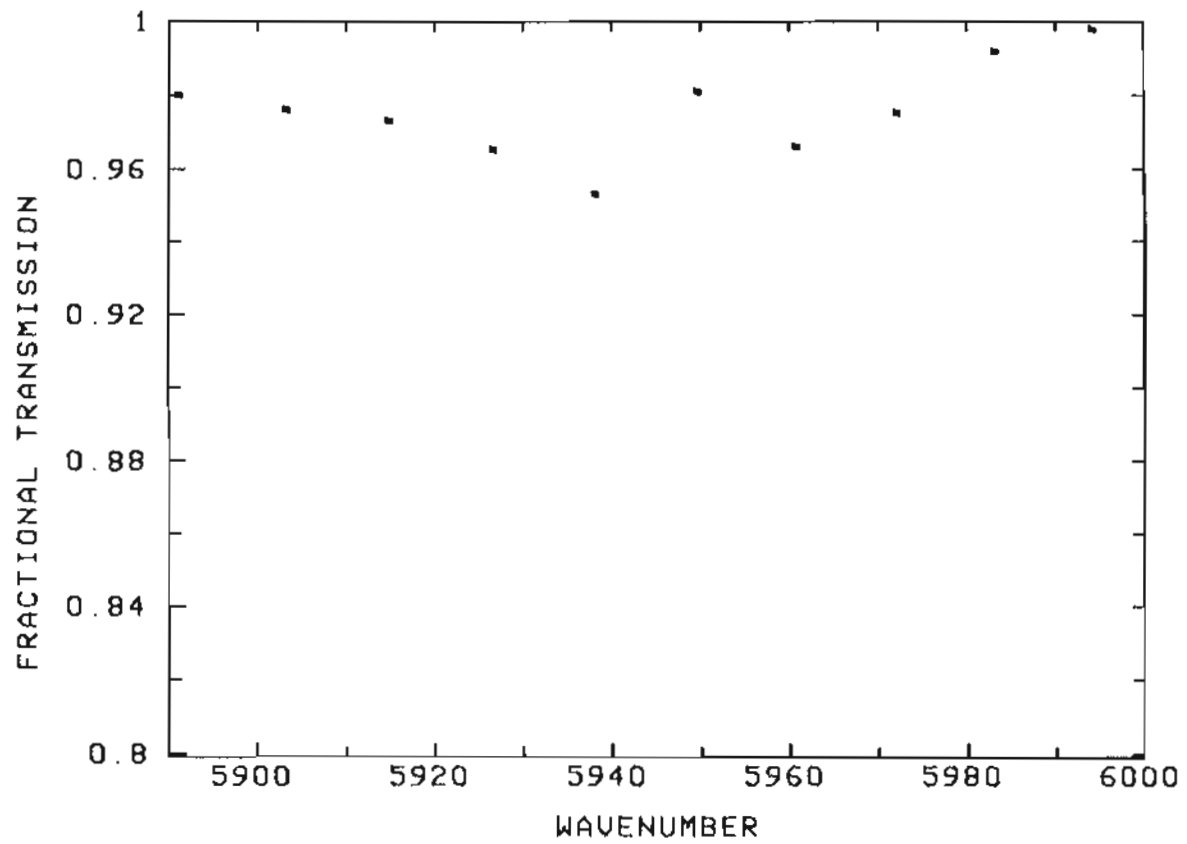


Figure 3.4 Transmittance through 1.2 cm-atm of CH<sub>4</sub> in the P branch of  $2\nu_3$  at a spectral bandwidth of  $1\text{cm}^{-1}$ .



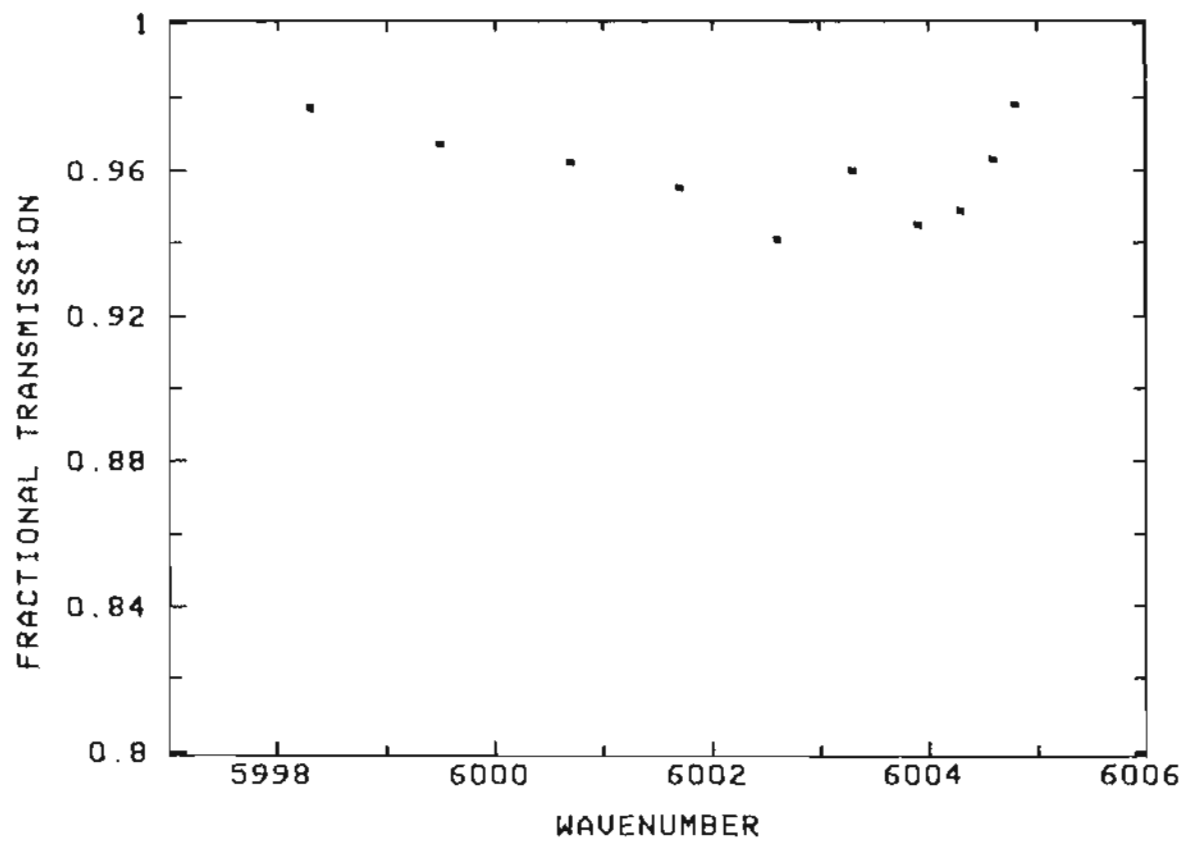


Figure 3.5 Transmittance through 1.2 cm-atm of CH<sub>4</sub> in the Q branch of 2ν<sub>3</sub> at a spectral bandwidth of 1cm<sup>-1</sup>.

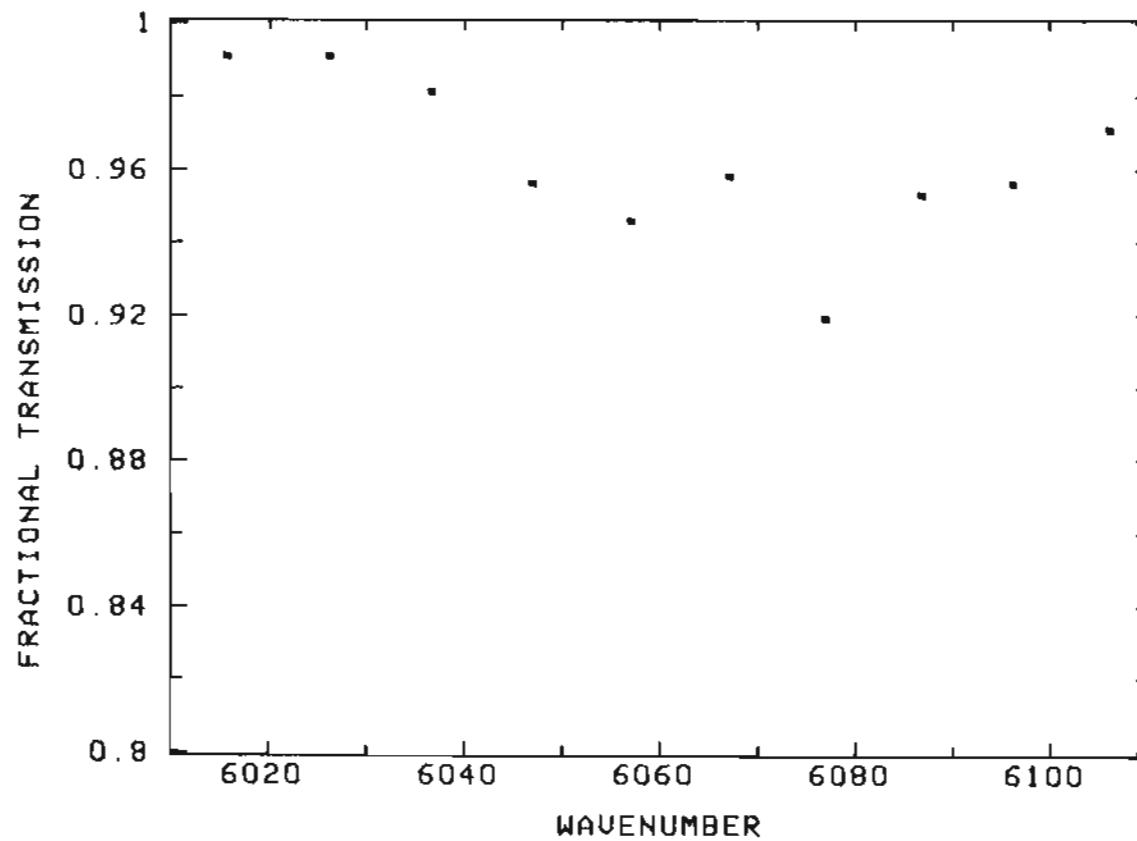


Figure 3.6 Transmittance through 1.2 cm-atm of CH<sub>4</sub> in the R branch of 2ν<sub>3</sub> at a spectral bandwidth of 1cm<sup>-1</sup>.

the other hand, Figure 3.3 yields a strength of  $0.02 \text{ cm}^{-1}\text{atm}^{-1}$  at the same resolution. Thus, the absorption shown in Figures 3.1 to 3.6, although not agreeing exactly with measured values, gives a reasonable estimate of the usefulness of the  $2\nu_3$  band at those spectral bandwidths for the DIAL process. While Figures 3.4 through 3.6 show narrowing of the spectral bandwidth to  $1 \text{ cm}^{-1}$  offers little improvement in absorption over that of  $2 \text{ cm}^{-1}$  bandwidth, it can be seen from Figures 3.7 to 3.9 that further reduction in bandwidth would be useful.

Figures 3.7 through 3.9 show that a source with a  $0.2 \text{ cm}^{-1}$  (FWHM) bandwidth would have a transmission of only some 85% when tuned on to one of the more powerful  $\text{CH}_4$  absorption lines. The peak absorption seen in Figure 3.9 on the R4 line corresponds to an absorption coefficient of approximately  $0.15 \text{ cm}^{-1} \text{ atm}^{-1}$ . This is three to five times the absorption found at  $1.3 \mu\text{m}$  as mentioned in Section 3.1. This absorption strength would offer large light transmission (85%) over 40 feet and reasonable discrimination (15%) over the 1 foot nearest the working face.

It should be noted here that for Equation 2.5 to be valid the DIAL laser source bandwidth must be equal to or less than the absorption line width<sup>91</sup>. For methane lines broadened in atmospheric pressure air the linewidth<sup>84,92,93,94</sup> is approximately  $0.2 \text{ cm}^{-1}$ . Thus to use Equation 2.5 without situation dependent correction factors<sup>91</sup> the source bandwidth must be less than equal to  $0.2 \text{ cm}^{-1}$ .

On the other hand, further reduction in the source bandwidth could lead to difficulties. If the laser line were narrower than the absorption line and tuned to its center the intensity of the returned light signal could be low due to absorption over the 40 foot distance while tuning instabilities could result if the laser were to be

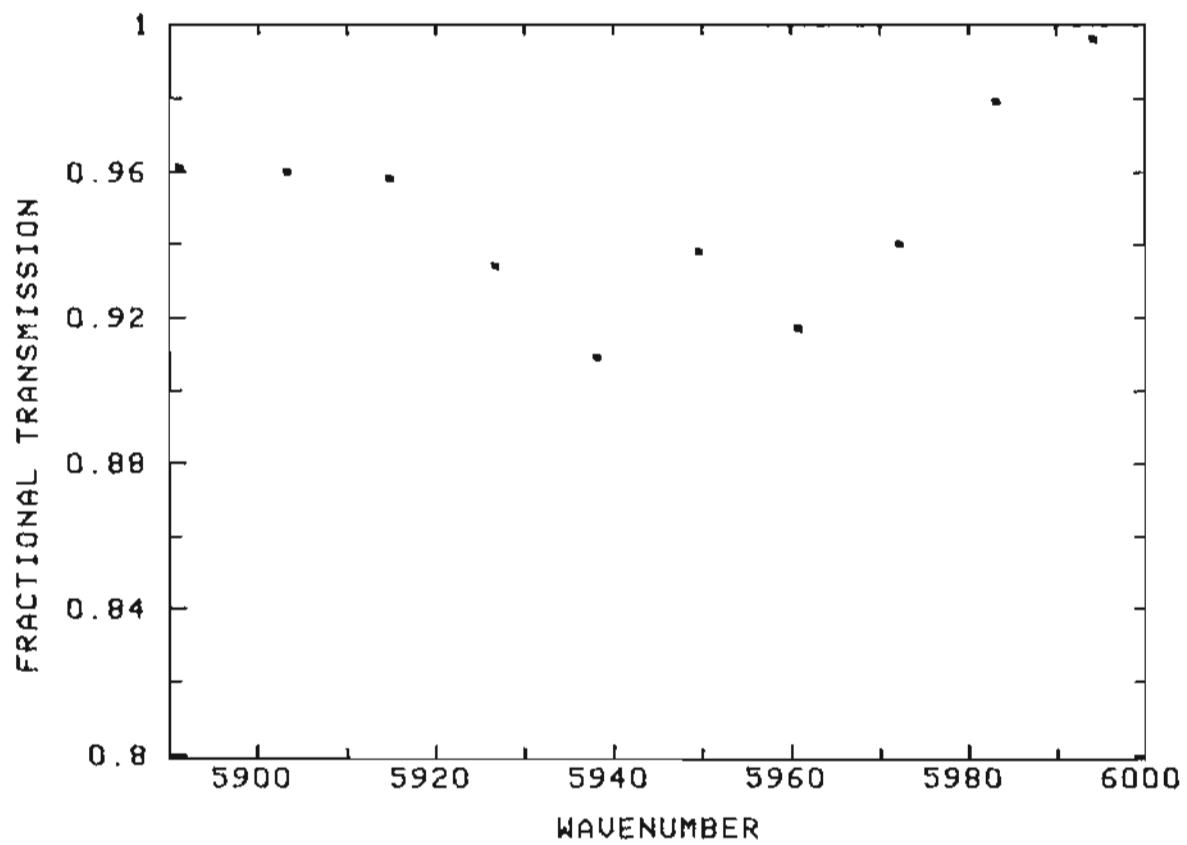


Figure 3.7 Transmittance through 1.2 cm-atm of CH<sub>4</sub> in the P branch of 2ν<sub>3</sub> at a spectral bandwidth of 0.2cm<sup>-1</sup>.

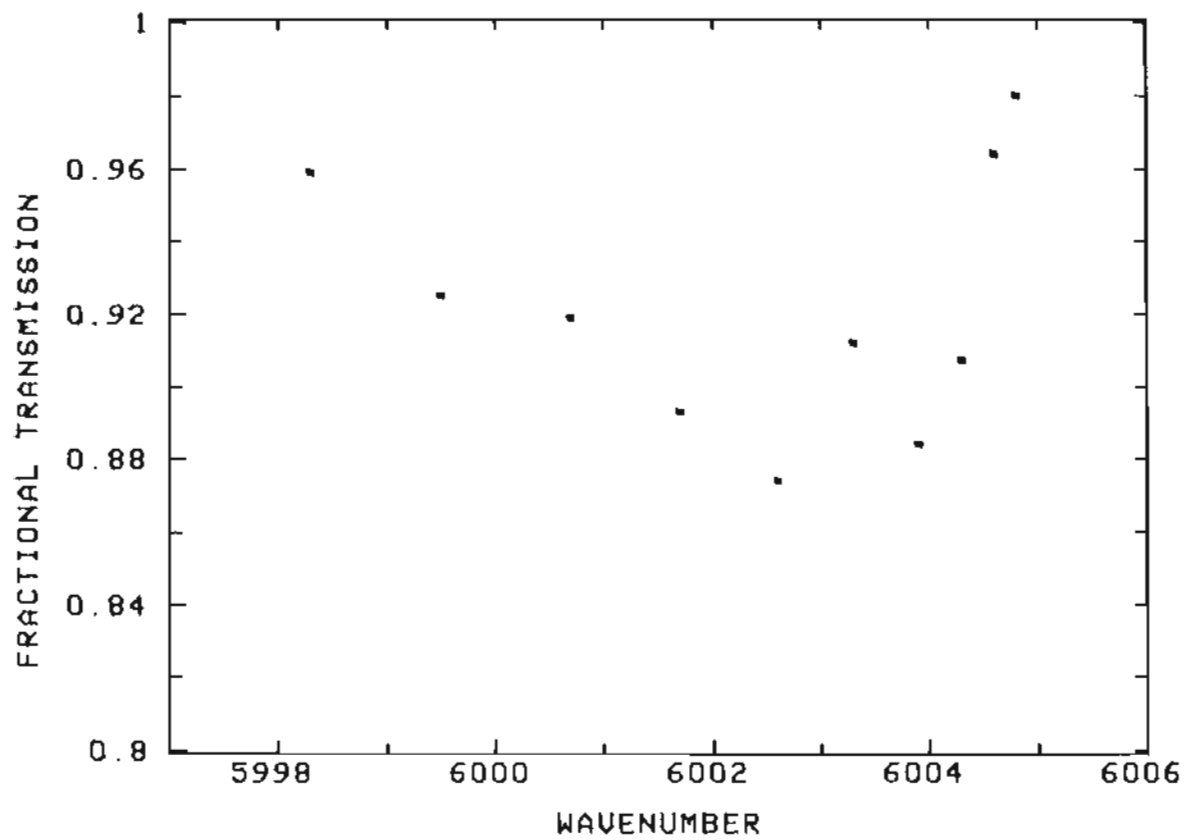


Figure 3.8 Transmittance through 1.2 cm-atm of CH<sub>4</sub> in the Q branch of 2ν<sub>3</sub> at a spectral bandwidth of 0.2cm<sup>-1</sup>.

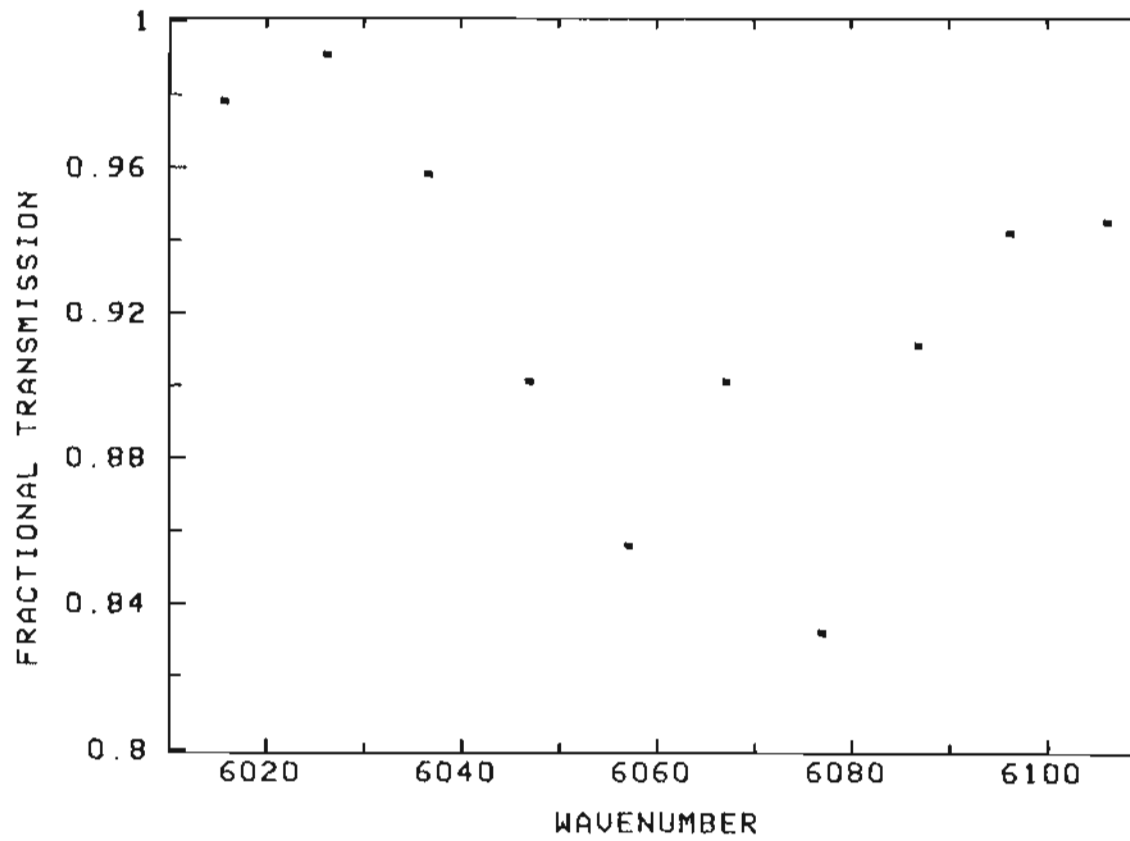


Figure 3.9 Transmittance through 1.2 cm-atm of CH<sub>4</sub> in the R branch of 2ν<sub>3</sub> at a spectral bandwidth of 0.2cm<sup>-1</sup>.

tuned to the edge of an absorption line due to the steepness of the line edges. Moreover, speckle noise would be promoted if the coherence length of the laser output became comparable to or less than that of the envisaged sample volume  $\left( \text{coherence length} = \frac{1}{\text{bandwidth in wavenumbers}} \right)$ . Thus a spectral resolution of less than, say,  $0.05 \text{ cm}^{-1}$  would be a handicap.

As Figures 3.8 and 3.9 show, the Q and R branches of band III both offer methane lines of appropriate strength for a laser bandwidth of  $0.2 \text{ cm}^{-1}$  FWHM. However, the Q branch lines have typical separations of only  $1 \text{ cm}^{-1}$  or so, while those of the other two branches have line separations of about  $10 \text{ cm}^{-1}$ . The Q branch line proximity could cause difficulties for tuning during the off-line segment of the DIAL process.

In summary, the spectroscopy of methane has been examined to study the applicability of injection diode lasers in a DIAL detection process. The  $2\nu_3$  band has been found to be spectroscopically suitable with the Q and R branches therein showing the most favorable absorption strengths. This observation then leads to examination in detail of injection semiconductor laser properties at the band III wavelength in the next chapter. In particular, the diode lasers used for this project are discussed.

#### 4. InGaAs/InP INJECTION LASERS

The last chapter demonstrated the  $2\nu_3$  absorption band of methane ( $\lambda \approx 1.65 \mu\text{m}$ ) to be spectroscopically suitable for a coal mine RDIAL methanometer. The spectral overlap of that band with the light output of  $\text{In}_x\text{Ga}_{1-x}\text{As}_y\text{P}_{1-y}/\text{InP}$  injection lasers for particular values of  $x$  and  $y$  was noted. The present chapter describes the room-temperature properties of such injection lasers operating in  $2\nu_3$  band. In particular, the attributes of the diode lasers used in this project are delineated.

There has been considerable interest in recent years in double-heterostructure (DH) semiconductor lasers having an output wavelength longer than that of GaAs ( $\lambda \approx 0.9 \mu\text{m}$ ). In all room-temperature injection devices, these lasers have been formed of III-V compound materials. Usually, these have used a quaternary  $\text{In}_x\text{Ga}_{1-x}\text{As}_y\text{P}_{1-y}$  light emitting layer with  $x$  and  $y$  chosen<sup>95</sup> to match the  $a_0 = 5.87$  Angstrom lattice constant of InP. The wavelength range thus possible is interesting for room-temperature sources<sup>96, 14.97-99</sup>, for detectors<sup>100-102</sup>, and for fiber optic communication with minimum loss and/or dispersion<sup>103</sup>, in addition to other applications.

$\text{In}_x\text{Ga}_{1-x}\text{As}_y\text{P}_{1-y}$  lattice matched to InP has a room-temperature long-wavelength limit of  $\lambda \approx 1.65 \mu\text{m}$  for the ternary composition  $\text{In}_{0.53}\text{Ga}_{0.47}\text{As}$ . This



alloy has been studied for a diversity of applications including both photoconductive<sup>104</sup> and photovoltaic<sup>106,102,107</sup> types of optical detectors and microwave FET's<sup>108</sup>. Additionally, room-temperature lasing has been obtained in InP/In<sub>0.53</sub>Ga<sub>0.47</sub>As/InP structures by three different techniques of layer deposition. The three methods are molecular beam epitaxy (MBE)<sup>15</sup>, liquid phase epitaxy (LPE)<sup>14</sup>, and vapor phase epitaxy (VPE)<sup>97</sup>.

Remote measurements using NIR DIAL require pulsed and high peak power light sources owing to detector dark current limitations<sup>32</sup>. In fact, in the next chapter it will be shown that  $P_o$  of Equation 2.5 should be greater than 100 mW for a successful RDIAL coal mine methanometer. In the realm of injection lasers, 100 mW of light output implies either broad area<sup>70</sup> or phased array devices<sup>109,110</sup>. Only recently has there been a report<sup>111</sup> on the construction of InGaAsP phased array devices. Thus in the spring of 1981 efforts were started at OGC to locate sources and secure samples of broad area diode lasers capable of high light power pulsed operation in the 1.65  $\mu$ m spectral region.

Only one of the numerous attempts to secure diode lasers was successful. During 1981 and 1982, B. I. Miller of A.T.T. Bell Labs, Holmdel graciously supplied In<sub>0.53</sub>Ga<sub>0.47</sub>As lasers to this project. These devices<sup>15</sup> have been used throughout the course of this project and their properties are described in the following sections. All the properties described represent experiments on several devices and some measurements were conducted on hundreds of lasers. Some of the material presented in the sections below was previously reported by DeFrez et al<sup>18</sup>.

#### 4.1 Laser Fabrication and Physical Form

The MBE process<sup>112,15</sup> used to grow the lasers described here started with an n-type InP substrate of (100) orientation. On this substrate, a 1  $\mu\text{m}$  thick  $n \approx 10^{18}\text{cm}^{-3}$  Ge-doped InP buffer and cladding layer was grown at a substrate temperature of 450  $^{\circ}\text{C}$  to provide a smoother foundation for the GaInAs active layer. The substrate temperature was raised to 510  $^{\circ}\text{C}$  for growth of a lattice-matched  $\text{Ga}_{0.47}\text{In}_{0.53}\text{As}$  layer and then lowered to 450  $^{\circ}\text{C}$  for growth of the  $\approx 5 \mu\text{m}$  thick top InP cladding layer. The latter layer was subsequently doped p-type by Cd diffusion with a duration intended to place a p-n junction at the InP/InGaAs interface.

Plating and sintering was used to create metallic contacts layers over both faces of the large-area sandwich, which was then ready for isolation into individual lasers. The end facets were created by (011) cleavage. The sides were partially string sawn and then broken to fashion separate lasers. The lengths of the lasers thus created varied from 300 to 650  $\mu\text{m}$ . The widths varied from 130 to 175  $\mu\text{m}$ . Figure 4.1 is a scanning electron microscope (SEM) micrograph of an individual laser.

Figure 4.2 is a SEM micrograph of part of an end facet. The figure shows one feature common to all such micrographs taken, one unusual feature, and rounded artifacts extraneous to the laser. As in all other SEM photos taken, the InGaAs active region is shown as a dark horizontal band of approximately 0.65  $\mu\text{m}$  thickness. This is the thickness that was planned in the MBE deposition<sup>15</sup>. Figure 4.2 also shows several diagonal dark lines. Only one other facet photographed showed such lines. These lines appear to be inclined at a 63  $^{\circ}$  angle to the junction

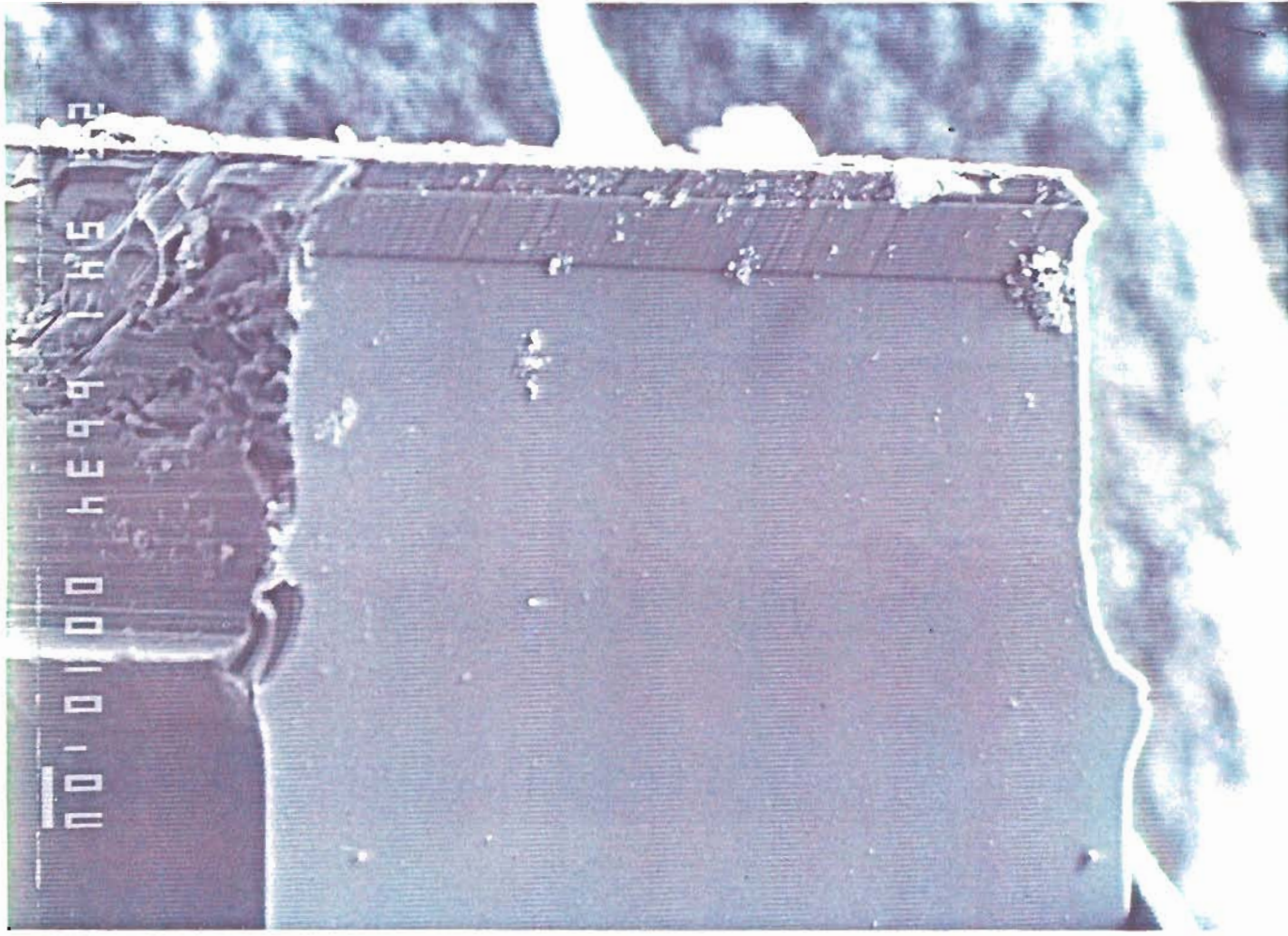


Figure 4.1 SEM micrograph of a broad area InGaAs/InP laser. The InP substrate, InP cladding layer, InGaAs active region, and top InP cladding layer are visible.

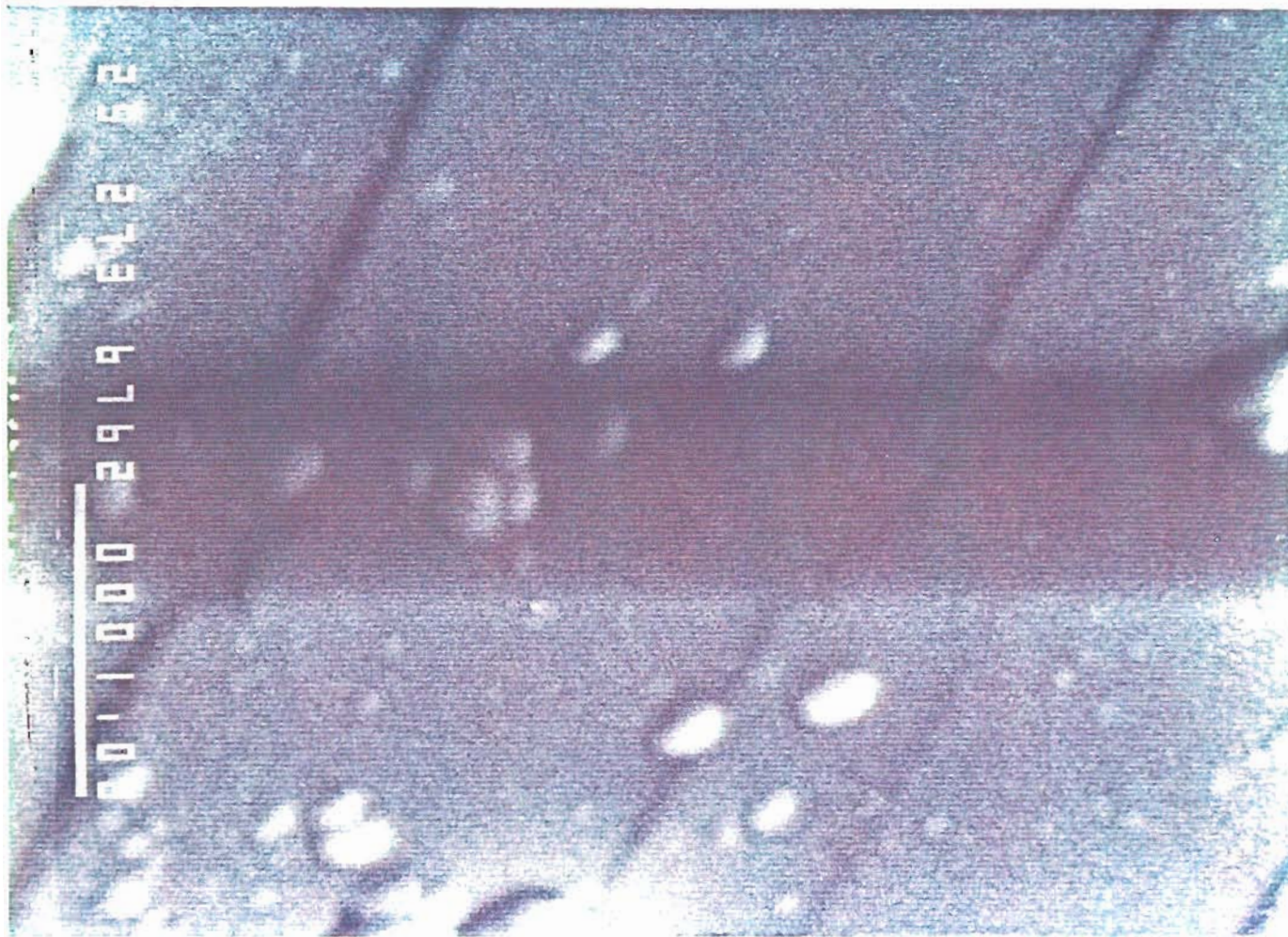


Figure 4.2 SEM micrograph of part of an InGaAs/InP laser facet. The two light areas are the InP cladding layers and the dark region is the In-GaAs active region.

plane. When correction is made for viewing direction, the diagonals are found to lie along the intersection of the  $(11\bar{1})$  planes with the end facet  $(011)$  plane.

It would thus appear that, in cleaving this facet, some jog planes were created as occasional interruptions of the  $(011)$  facet surface. Any such interruption that passes across the end of the active region can be expected to weaken the spatial coherence of the laser output and be a source of non-radiative carrier recombination. This latter circumstance could lead to catastrophic failure at high injection levels. Indeed, the reason this device was used for SEM viewing was its catastrophic failure at a high drive current.

#### 4.2 Laser Output Spectral Characteristics

The spectral output for 15 of these lasers was measured at  $T \approx 293$  K with low duty cycle high current pulses. The pulse repetition frequency (PRF) was between 100 and 500 Hz resulting in a duty factor of  $< 10^{-4}$  using 150 ns pulses. Owing to the low duty cycle, average input power was low, but peak input power reached as high as 10 W. The drive current used for the spectral runs was from 1.5 to 3 times lasing threshold. The various lasers measured had threshold currents ranging from 1.7 to 4.7 Amps, which is equivalent to an area and thickness normalized threshold of 4 to 10  $\text{kA}/\text{cm}^2\mu\text{m}$ .

The spectral response curves showed from 4 to 8 maxima in each case. As would be expected for the pulsed mode operation, the various spectral maxima represent multiple longitudinal mode operation<sup>113</sup>. Figure 4.3 shows the extreme case of 8 modes spanning the range 1.626 to 1.651  $\mu\text{m}$ . The spectral width shown is greater than 20 nm. Of the various lasers measured while in contact with a room

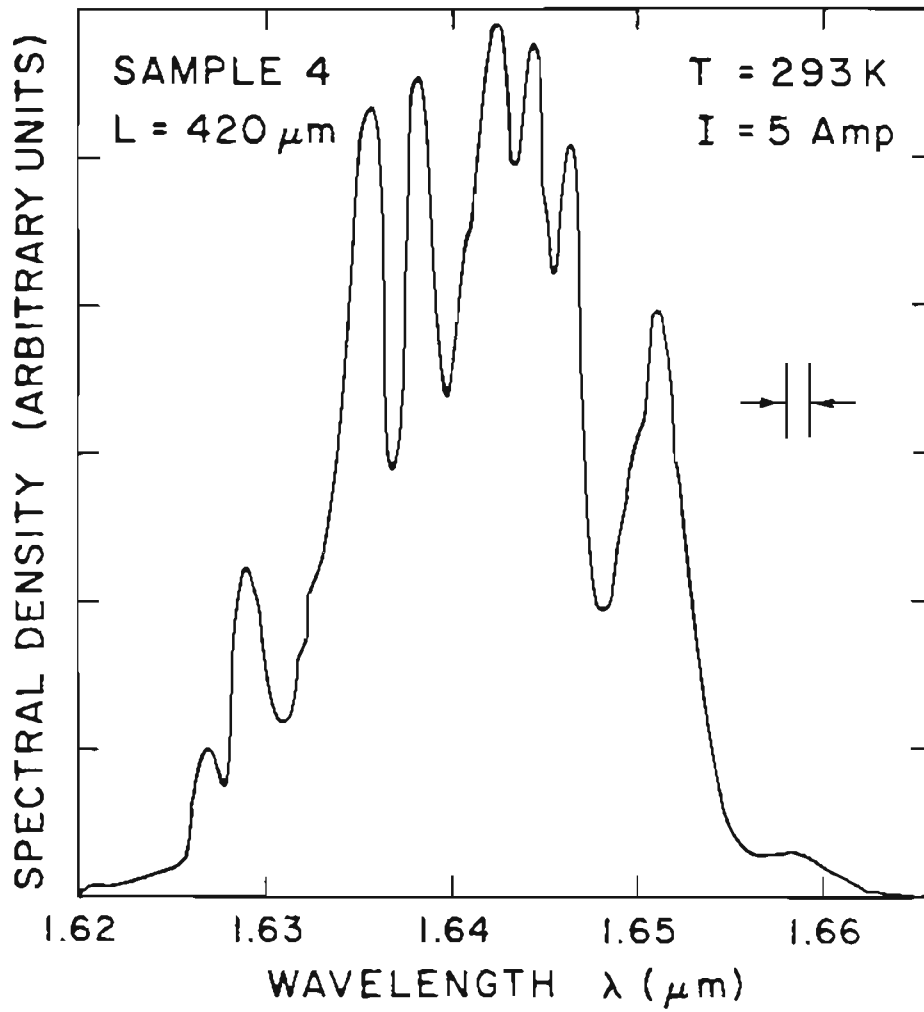


Figure 4.3 Optical output vs. wavelength for a broad area InGaAs/InP laser. The laser is operated in a low duty cycle with a 150 nsec optical pulse.

temperature heat sink, none had modal wavelengths outside the limits of those in Figure 4.3. The spectral curves were obtained by synchronous detection of the output with a germanium photodiode and a Jarrell-Ash Mark X 0.275 m monochromator.

For one of this group of lasers, of length 420  $\mu\text{m}$ , the modes were separated by 1.3 nm. However, for most spectral scans the modal separation was two or three times larger, indicating missing modes.

The minimum modal separation for a diode laser is related to its group index of refraction through the equation<sup>70</sup>.

$$\delta\lambda = \frac{\lambda^2}{\left(\mu_{\text{eff}} - \lambda \frac{d\mu_{\text{eff}}}{d\lambda}\right)2L} \quad (4.1)$$

where  $\lambda$  is the emission wavelength,  $\delta\lambda$  is the modal separation,  $L$  is the cavity length,  $\mu_{\text{eff}}$  is the effective refractive index for light in the active region, and  $\mu_{\text{eff}} - \lambda \frac{d\mu_{\text{eff}}}{d\lambda}$  is the group index of refraction. For  $\delta\lambda = 1.3$  nm, the group index is 2.5. Using an effective refractive index of about 3.5<sup>114</sup>, where equal TM and TE optical confinement in the active layer is assumed<sup>115</sup>, yields  $\frac{d\mu_{\text{eff}}}{d\lambda} = -0.6$  at the lasing wavelength. This experimental group index is less than the 4.5 index normally found in GaAs diode lasers<sup>70</sup> and the only one, to this author's knowledge, reported for InGaAsP/InP lasers. It should be noted that if the minimum  $\delta\lambda$  observed here also has missing modes, then the group index would be larger by some positive integer factor. Thus the group index could theoretically take on the values 2.5, 5.0, 7.5, etc.

### 4.3 Output Polarization

The active region of a DH injection laser, the laser type used on this project, is cladded with material of lower index of refraction than that of the active region itself. The low index cladding forms a dielectric waveguide<sup>116</sup> for the laser light and thus increases operating efficiency<sup>117</sup>. When the guided wave has its E field in the plane of the waveguide, it is said to be a transverse electric (TE) mode<sup>117</sup>. Conversely, when the guided wave has its H field in the plane of the waveguide, it is called a transverse magnetic (TM) mode.

Most recent analyses of the properties of InP/InGaAsP/InP lasers have concentrated on the behavior to be expected with TE mode polarization<sup>119,114</sup>. However, the lasers of this project were found to be TM polarized. Under the pulsed room-temperature operation described above, the ratio of TM to TE polarization is much greater than 1. No Attempt was made to determine the phase relationship between the TM and TE components of the light output. Figure 4.4 shows the ratio of TM to TE emission plotted versus drive current for one device. The figure was generated by passing the light from the diode laser through a rotating Nicol Prism and plotting the ratio of the extrema of the AC current produced in a Ge photodiode versus laser drive current. In the figure, the onset of TM polarization coincides with the lasing threshold. Below threshold, the ratio is slightly greater than 1.

The semiconductor laser monograph literature<sup>120,70,117</sup> has tended to treat only TE polarization for DH lasers, since this is the mode usually seen. That mode is usually dominant because of the higher facet reflectivity for TE modes<sup>121 119,122</sup>. TM-mode dominance thus implies that the gain minus internal absorption losses for such modes is greater than for the TE modes by an amount sufficient to compensate



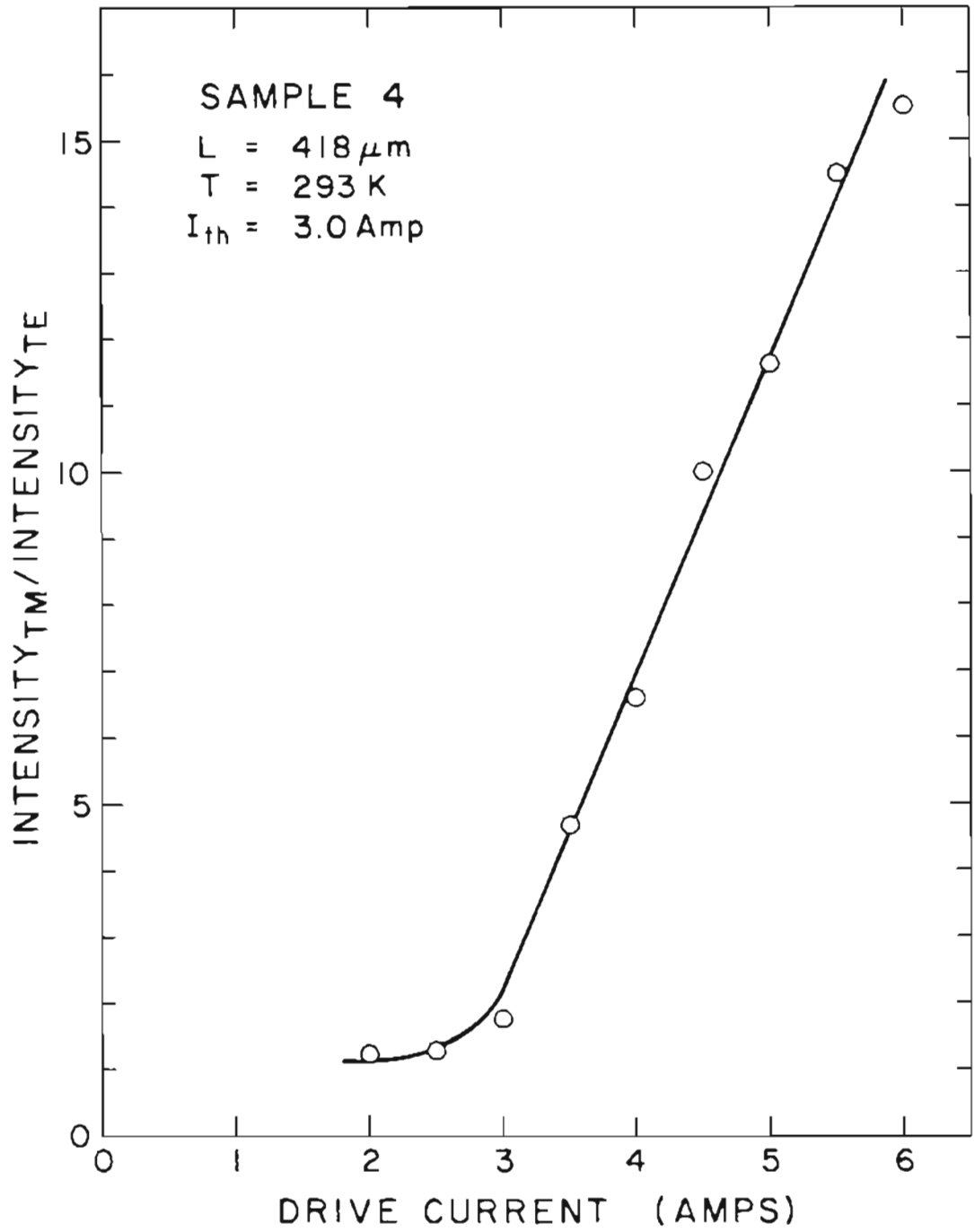


Figure 4.4 Optical output polarization ratio vs. drive current for a broad area InGaAs/InP laser. The laser is operated in a low duty cycle with a 150 nsec optical pulse.

for the higher reflection losses. In short, for the fundamental transverse mode (the only transverse mode observed, as explained in the next section)<sup>70</sup>:

$$(g_{\text{TM}_0} - \alpha_{\text{TM}_0}) > (g_{\text{TE}_0} - \alpha_{\text{TE}_0}) + \left(\frac{1}{L}\right) \ln \left( \frac{R_{\text{TE}_0}}{R_{\text{TM}_0}} \right) \quad (4.2)$$

where  $g$  is the gain,  $\alpha$  is the absorption coefficient,  $L$  is the laser length, and  $R$  is the geometric mean of the facet reflectivities. For the lasers in the present study,  $L \approx 400 \mu\text{m}$ ,  $R_{\text{TM}_0} \approx 0.26$ ,  $R_{\text{TE}_0} \approx 0.38$ . These numbers are consistent with:

$$(g_{\text{TM}_0} - \alpha_{\text{TM}_0}) > (g_{\text{TE}_0} - \alpha_{\text{TE}_0}) + 10 \text{ cm}^{-1} \quad (4.3)$$

The possible relations between the various gains and losses will be discussed further in Section 4.7.

#### 4.4 Output Beam Spatial Characteristics

Far-field beam divergence measurements were made on 15 of the diodes. The divergence was measured perpendicular to the active region by rotation of the diode laser relative to a fixed Ge photodiode. In each case the far-field distribution appeared to be  $\text{TM}_0$ , although the active layer is thick enough to support the  $\text{TM}_1$  mode as well<sup>116</sup>. Numerical values for the FWHM angular divergence were calculated by least-squares fitting of the data to Gaussian functions, and were all in the range from  $62^\circ$  to  $70^\circ$ .

This large divergence is consistent with an active layer thickness in the range 500-700 nm, based on the work of Butler and Kressel<sup>123</sup>, and others<sup>124-126, 118</sup>, and on the noted similarity of TE and TM mode behavior with respect to angular divergence<sup>117</sup>.

An output-beam imaging system, using an IR vidicon, monitor, and associated electronics and optics, was set up to examine the diode laser near field spatial distribution. Figure 4.5 shows one example of the results obtained. The figure was formed by reproduction of a photograph taken directly from the television monitor. The horizontal streaking is an artifact of the television raster. Note that this laser has a filamentary output, with four dominant areas of lasing activity. Such filamentary lasing is often characteristic of broad area lasers because of mode self-focusing<sup>70</sup>. The brighter filaments correspond to regions of smallest threshold current density, since observations while the current pulse amplitude was progressively reduced showed the lasing output more and more confined to the brightest of these regions.

#### 4.5 Laser Threshold, Output, and Efficiency

InGaAsP/InP lasers with various structures have been developed in recent years. Usually these devices exhibit a larger temperature dependence of threshold current,  $I_{th}$ , and external differential quantum efficiency,  $\eta_{ext}$ , than do similarly fabricated GaAs lasers<sup>97</sup>. This general characteristic of InGaAsP lasers degrades their operating performance at room temperature and above.

Several models have been proposed to explain the temperature dependence of  $I_{th}$  and  $\eta_{ext}$ . The proposed models include Auger recombination<sup>127-132</sup>, free-carrier losses<sup>128</sup>, carrier leakage over the InP cladding layer barriers<sup>133</sup>, and intervalence band absorption<sup>134</sup>.

Some of the proposed models have been subsequently shown to be of little significance. By changing internal losses through varying facet reflectivity and

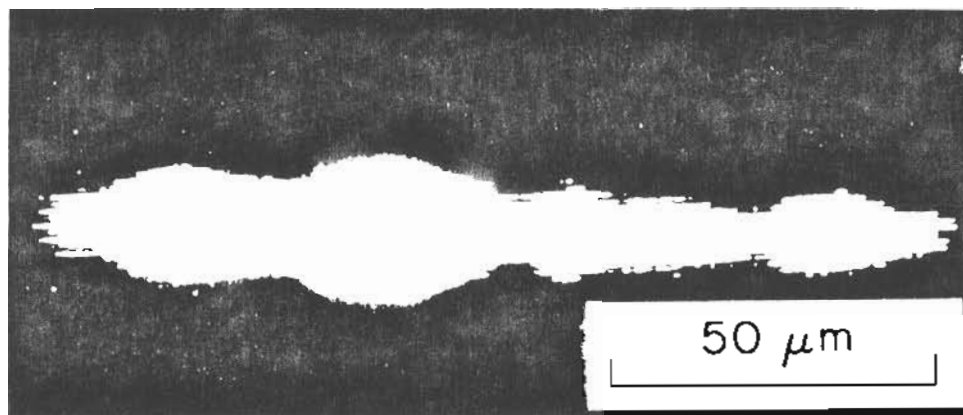


Figure 4.5 Near field spatial distribution of optical intensity of a broad area InGaAs/InP laser. The laser is operated in a low duty cycle with a 150 nsec optical pulse.

operating temperature, Higuchi et al. demonstrated intervalence band absorption to be unimportant<sup>135</sup>. Chiu et al. have shown Auger enhanced field and hot carrier leakage to be the prime source of the temperature dependence of  $I_{th}$  and  $\eta_{ext}$ <sup>133</sup>. Their work showed that the temperature dependence was primarily due to the p doping level in the InP cladding layer a conclusion supported by other recent work<sup>108</sup>.

Tamari et al<sup>136</sup>. have constructed stripe geometry lasers of high efficiency ( $\eta_{ext} = 74\%$ ) with no temperature dependence between 20 °C and 70 °C, contrary to previous results.

Some of the data from the present project is presented below and is interpreted in terms of the Auger theory. Data on output power versus drive current were obtained for 84 lasers. Figure 4.6 shows point by point data for three of the devices. These include sample 11, which had the largest threshold current, and sample 13, which had one of the smallest threshold currents in the group.

The subthreshold data in Figure 4.6 for sample 11 show a markedly sublinear (ie. concave down) behavior. Sublinearity in this region is also vestigially apparent for sample 4. Dutta and Nelson<sup>127</sup> have shown Auger recombination to be the source of this type of operating characteristic, since radiative recombination increases as  $n^2$  while Auger recombination grows as  $n^x$  where  $x$  is between 2 and 3 and where  $n$  is the injected carrier density. This result has been corroborated by the other work<sup>129</sup>.

However,  $I_{th}$  and  $\eta_D$  are less than ideal even for those lasers not exhibiting Auger characteristics. For example, the threshold current  $I_{th} \approx 1.8$  A for sample 13, as illustrated in Figure 4.6. is equivalent to a threshold current density  $J_{th} \approx 2.8$

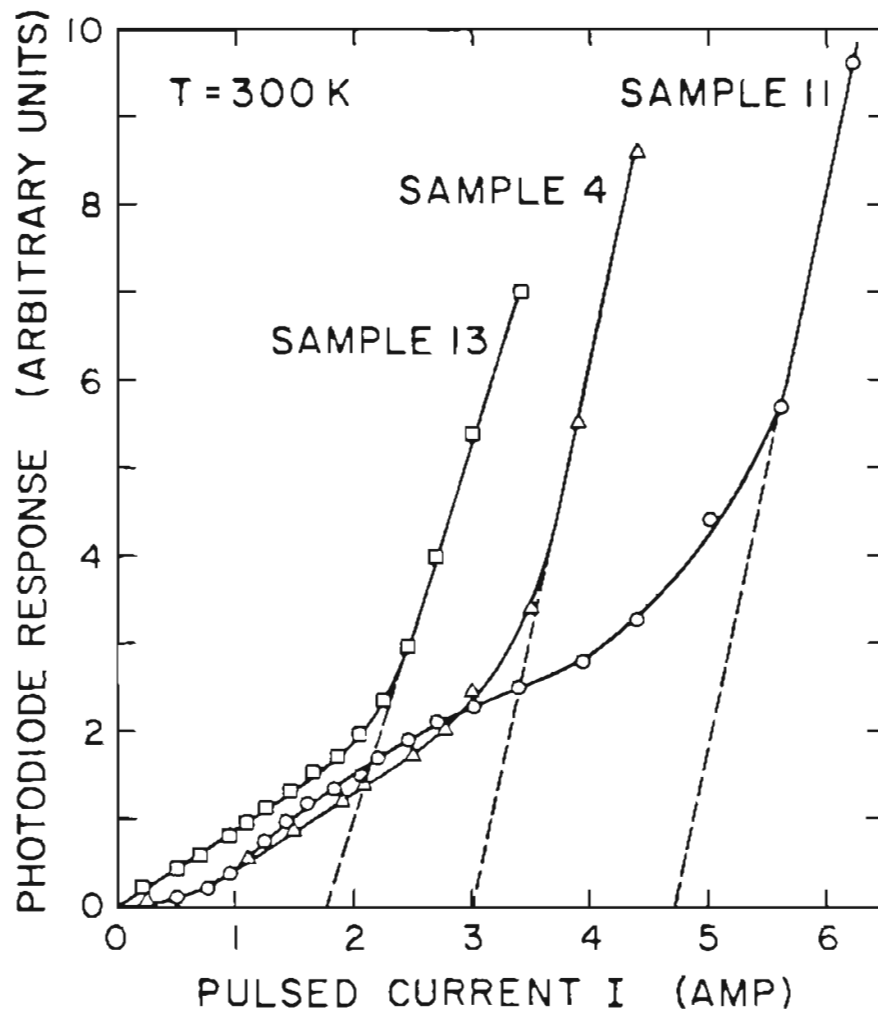


Figure 4.6 Optical output vs. drive current for three broad area InGaAs/InP lasers.

kA/cm<sup>2</sup>. This is about 40% larger than the lowest threshold density given by the model of Botez<sup>118</sup> for an active layer thickness of  $d \approx 600$  nm. For some of the measured devices,  $J_{th}$  was as much as 2.5 times greater again.

The external differential quantum efficiency was calculated from the slope above threshold of output power versus drive current for 84 lasers. Whereas Figure 4.6 expresses an ordinate in arbitrary units, these data were taken using a calibrated Ge photodiode. Thus, the absolute slope of light output versus drive current could be measured. Often 100 mW or more of light power, single facet, was observed at drive currents less than 3 times  $I_{th}$ . Values for  $\eta_{ext}$  were found to lie in the range  $0.030 < \eta_{ext} < 0.116$  (double facet). All values in this range are far less than those recently reported for broad area InGaAsP devices<sup>136</sup>.

It is a normal practice to deduce the internal quantum efficiency ( $\eta_i$ ) and the effective internal absorption coefficient ( $\alpha_i$ ) by using the equation<sup>70</sup>:

$$\eta_D = \frac{\eta_i}{\left[1 + \alpha_i L / \ln(1/R)\right]} \quad (4.4)$$

where  $L$  is the cavity length, and  $R$  is the geometric mean of the end facet reflectivities, and  $\eta_D$  is the abbreviated expression for the the external differential quantum efficiency. From Equation 4.4, a plot of  $(1/\eta_D)$  should yield a straight line with positive slope proportional to  $\alpha_i$  and with intercept  $1/\eta_i$ . However, when  $1/\eta_D$  for the sample of 84 lasers was plotted against length, in Figure 4.7, a minimum occurred near  $L=400$   $\mu\text{m}$  with the slope of the curve being negative below this value. The negative slope implies a negative, nonphysical, absorption coefficient in Equation 4.4, which leads to the discussion in Section 4.7.

#### 4.6 Laser Lifetimes

There has been interest recently in the operating lifetimes of InGaAsP/InP injection lasers. It has been noted that the InGaAsP devices have a potentially longer operating life than their AlGaAs counterparts<sup>70</sup>.

The InGaAsP potential for long lifetimes is caused by a number of factors. The dark line defects<sup>70</sup> common to AlGaAs devices have been found to be scarce in InGaAsP structures at both room<sup>137</sup> and elevated<sup>138</sup> temperatures. Long term facet oxidation has been found to be source of degradation in InGaAsP lasers. However, the degradation rate is about two orders of magnitude smaller<sup>139</sup> than for AlGaAs lasers when operated at room temperature with an optical output of  $\approx 1\text{MW}/\text{cm}^2$ . In fact, the change in the threshold current for InGaAsP diodes has been measured to be less than 1% when operated for 1000 hours in a CW mode at room temperature<sup>140</sup>. Also, catastrophic dark line defects, common to AlGaAs laser facets, are not generated in InGaAsP devices below  $100\text{MW}/\text{cm}^2$  of light output<sup>141</sup>. The diodes of the present project operating at 100 mW of output power, have a power density of  $\approx 0.1\text{MW}/\text{cm}^2$ .

During this project, no long term laser degradation has been observed for the drive currents and output powers used. A life test was conducted on one sample. It was pulsed at 6 Amps and 400 Hz PRF with 160 ns pulses. The diode was observed to stay within  $\pm 15\%$  of its average output for  $10^8$  sequential pulses, with no sign of any downward trend. The diode was then pulsed at 9 Amps, resulting in a 60% increase in the output power. After operation for  $10^8$  more pulses there was no apparent degradation. Additionally, many devices have been run intermittently over much longer periods, weeks to months, at a 10 kHz prf with no sign of degrada-



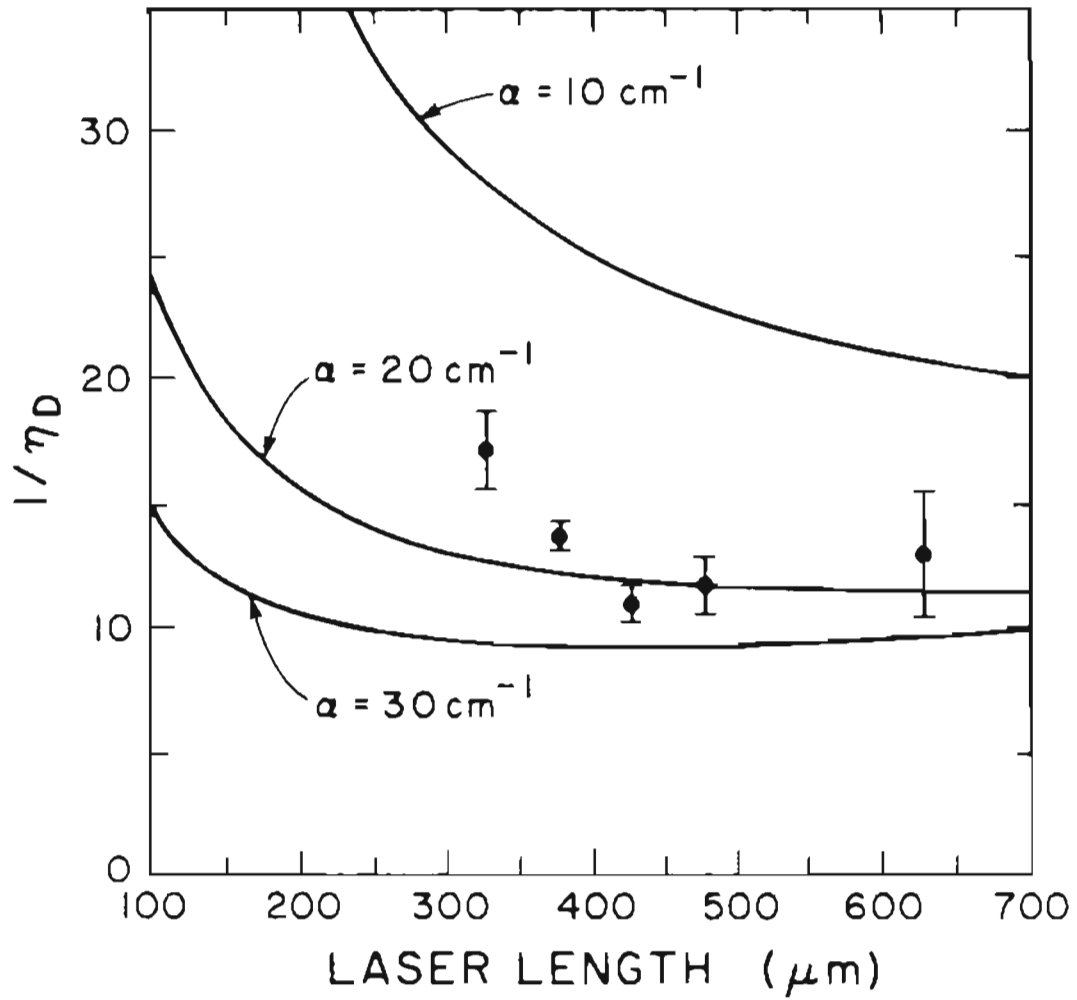


Figure 4.7 Reciprocal external differential quantum efficiency vs. laser cavity length for 84 broad area InGaAs/InP lasers.

tion.

However, during the project, several devices catastrophically failed at injection current densities of about 20 kAmps/cm<sup>2</sup>. No attempt was made to identify the mechanism associated with this failure mode although the failure symptom is facet damage. Figure 4.8 shows the facet of one such device. In the figure, the horizontal band, labeled "A", was caused by localized melting at high drive currents. In light of recent work reporting 100 MW/cm<sup>2</sup> thresholds<sup>141</sup> for optically induced facet damage in the InGaAsP device family, it is likely that the observed melting is caused by nonradiative carrier recombination. Chapter 7, in its discussion of antireflection coatings for laser facets, presents further evidence for nonradiative carrier recombination.

#### 4.7 Discussion

As outlined above, the experimental data provided two unexpected results. First, deduction of the internal absorption coefficient using the standard method (Equation 4.4) produced a nonphysical value. Second, while most DH injection lasers are TE polarized, all the devices measured were TM polarized.

Figure 4.7 shows a plot of the inverse external differential quantum efficiency ( $1/\eta_D$ ) versus laser length for 84 lasers. The lasers were grouped according to length in 50  $\mu\text{m}$  intervals. The error bars show the standard error in the mean. If the usual equation for  $\eta_D$  versus length were to hold here, a straight line plot would be expected. This is clearly not the case in the figure.

In this connection, Whiteaway and Thompson<sup>142</sup> have described a different loss model for a DH laser not far above threshold. Not far above threshold means, here,

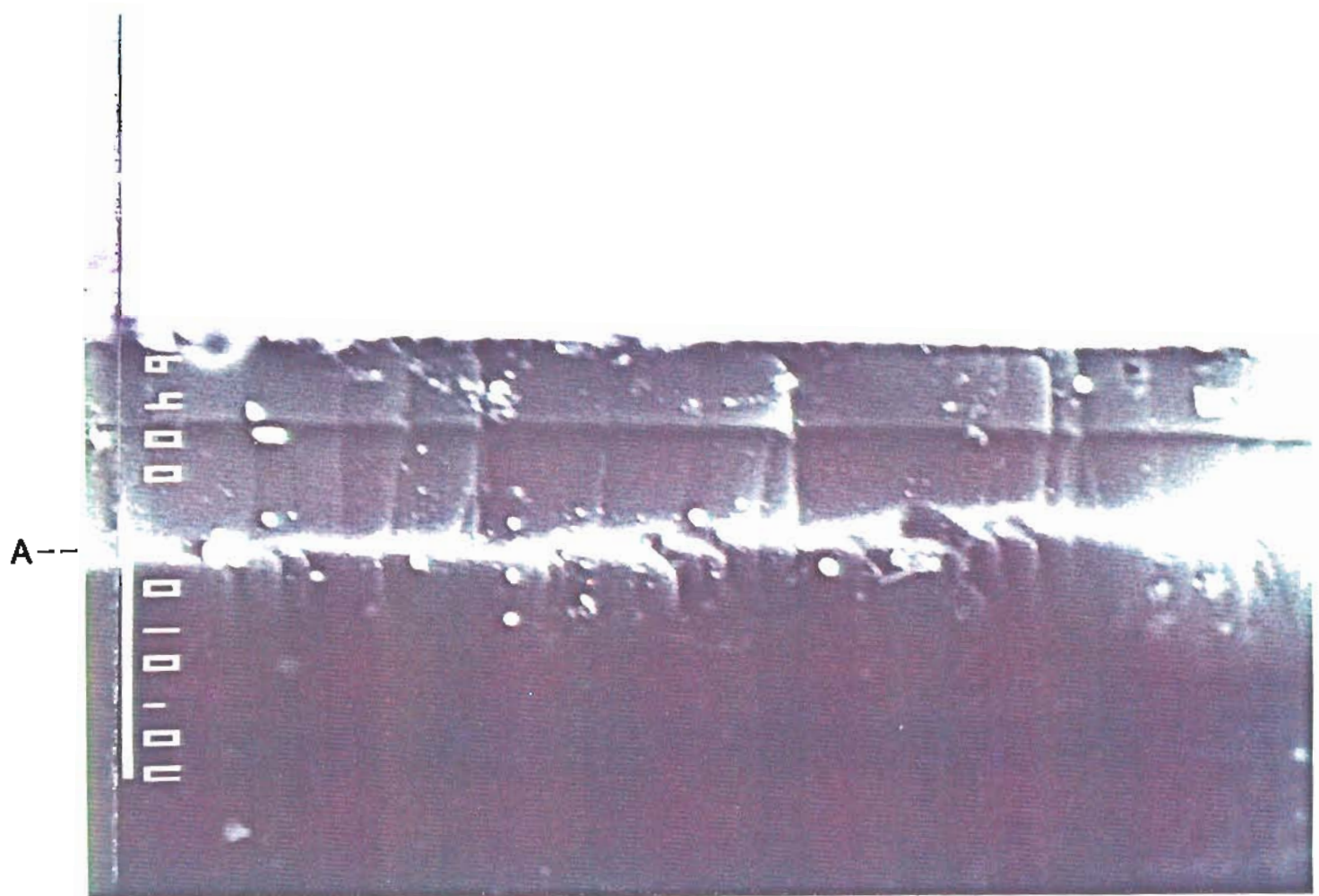


Figure 4.8 SEM micrograph of facet of InGaAs/InP laser after catastrophic failure.

operation at drive currents corresponding to that part of the light versus current curve above threshold but before any inflection. The model of Whiteaway and Thompson is consistent with  $(1/\eta_D)$  first decreasing with length and then increasing at larger lengths. This is consistent with the pattern observed in Figure 4.7.

Indeed, when the constants appropriate to TM mode reflectance losses and to the operational conditions used are inserted into the provisions of a slightly simplified Whiteaway and Thompson model, interesting families of curves can be plotted for  $(\eta_i/\eta_D)$  versus  $L$ . The families are generated with the internal absorption coefficient  $\alpha_i$  as a parameter. Such a family with  $\eta_i=0.4^{143}$  is plotted in 4.7. As the figure shows, the experimental points are consistent with an absorption coefficient  $\alpha_i \approx 20\text{cm}^{-1}$ . The discrepancy in the figure at shorter wavelengths must be caused by something other than the small statistical sample shown.

This chapter has explained in detail the properties of high power diode lasers that possess a spectral overlap with the  $\text{CH}_4$   $2\nu_3$  absorption band mentioned in Chapter 3. Chapter 5 examines the requirements for a diode laser DIAL methanometer for coal mines. Chapter 6 will then bring together these topics. That chapter introduces external resonator diode lasers as a means of matching the diode laser characteristics presented here to the DIAL requirements presented in the next chapter.

## 5. METHANOMETER REQUIREMENTS

Both statutory and technical considerations determine the design requirements for a diode laser DIAL methanometer for use in coal mines. The statutory criteria determine the accuracy, frequency, and safety requirements of methane measurements in underground mines. Technical considerations set, along with other parameters, the laser optical power and spectral bandwidth. This chapter presents the pertinent requirements and lays out the means by which a remote diode laser DIAL methanometer can meet them.

### 5.1 Federal Regulations

Federal regulations apply to remote measurements of methane in coal mines in two ways. First, federal law <sup>2</sup> requires a methane measurement every twenty minutes at one foot from a working mine face. This same law specifies that mining must cease whenever the measured methane concentration exceeds 4%. As was mentioned in Chapter 2, this regulatory requirement necessitates the use of range resolved DIAL (RDIAL) techniques in the present context. The basic RDIAL expression, Equation 2.5, was derived in the same chapter. In this chapter, in Section 5.3, that equation will be inverted to solve for the methane concentration.

Second, federal law<sup>144</sup> also specifies several particular requirements for portable methane detectors. In addition to general requirements about such matters as durability, practicality of operation, and serviceability underground that will not be discussed here, the law lays out specific performance requirements for indicating detectors. Indicating detectors are defined as devices "that will show, within certain limits of error, on an adequate scale, the percentage of methane in a gassy atmosphere" and are the devices appropriate to the present discussion. To be specific, an indicating detector must give indications (read measurements) as low as 0.25% methane and should give readings as high as 4% with a minimum upper capability of 2%. The indications for the various percentages must be within the limits of error shown in Table 5.1. The law further specifies that during tests of the instrument made at several percentages within the range of the detector neither the average of 10 readings nor more than 2 readings for each percentage may exceed the limits of error given in Table 5.1. Sections 5.3 and 5.4 will discuss the implications of the law on such system properties as optical output power and detector sensitivities. First, however, the maximum amount of safe laser emission near the 1.65  $\mu\text{m}$  wavelength specified in Section 3.3 must be calculated.

## 5.2 Laser Power: Safety Considerations

An eye and skin safety calculation was carried out using the 1980 ANSI Standard<sup>145</sup> and again using the Bureau of Radiological Health regulations<sup>146</sup>. The two approaches yielded equivalent results and the explicit calculation using the ANSI Standard is presented in Appendix B. That calculation assumes a 100 ns pulse duration at a pulse repetition frequency of 10 kHz and gives an allowable peak opti-

Table 5.1 Allowable Variations in Scale Reading		
Methane in Mixtures (%)	Minimum Indication (%)	Maximum Indication (%)
0.25	0.10	0.40
0.50	0.35	0.65
1.00	0.80	1.20
2.00	1.80	2.20
3.00	2.70	3.30
4.00	3.70	4.30

cal power per pulse of 4.3 watts. The use of the pulse parameters given above is motivated by the lifetest data mentioned in Chapter 4 and the calculations of Sections 5.3 and 5.4.

The allowable peak optical power indicated by the safety calculation is much larger than that achieved to date with diode lasers operating with a narrow spectral output in pulsed mode. Thus safety is not a limiting factor for a diode laser DIAL methanometer. The required optical power is calculated in the next section.

### 5.3 Laser Power: Detection Considerations

An analysis of the optical output requirements must start with the fundamental RDIAL equation for the Mie backscattered signal (ie. Equation 2.5):

$$P_r(R) = \left[ \frac{\beta_{Mie} \Delta R}{4\pi} \right] K P_o \left[ \frac{A}{R^2} \right] e^{-2 \int_0^R \alpha(r) dr} \quad (5.1)$$

where  $P_r$  is the backscattered light signal from a target at range  $R$ ,  $P_o$  is the

transmitted power,  $K$  is the optical receiver system efficiency,  $\frac{\beta_{\text{Mie}}}{4\pi}$  is the effective reflectivity of the Mie scatter volumes,  $A$  is the area of the receiving telescope, and  $\alpha$  is the volume absorption coefficient of the atmosphere traversed by the transmitted and reflected light. Not all the above parameters are well known. In particular,  $\beta_{\text{Mie}}$  and  $\kappa$  can only be approximated. However, experiments<sup>147</sup> conducted by this author at HRL in 1979 provide data relevant to the Mie backscatter coefficient of airborne coal dust.

In those experiments,  $\approx 2.5$  watts of  $1.65 \mu\text{m}$  radiation was directed onto a coal dust cloud with a concentration of approximately  $40 \text{ mg/m}^3$  and the backscattered portion was detected at a distance of 16 feet from the scattering volume. The returned optical power,  $P_r$ , detector responsivity,  $R_D$ , detected voltage,  $V_r$ , and the amplifier gain,  $g$ , follow the relationship:

$$P_r = \frac{V_r}{gR_D} . \quad (5.2)$$

Since the experiments suggested  $V_r \approx 100 \text{ mv}$  for  $g = 10^7 \text{ V/A}$  and a detector responsivity  $R_D \approx 0.4 \text{ A/W}$ ,  $P_r$  must approximately equal  $2.5 \times 10^{-8}$  watts. It should be noted here that there was no observed wavelength dependence of the returned signal on the wavelength tuning of the Er:YAG laser during these experiments. Thus, for the given distance and coal dust level

$$P_r = 10^{-8} P_o . \quad (5.3)$$

Based on these results, the value of  $\beta_{\text{Mie}}$  is constant over a wavenumber range of few  $\text{cm}^{-1}$  range near  $1.645 \mu\text{m}$  and is approximately  $15 \text{ km}^{-1}$ , calculated from Equa-



tion 5.1 using the reasonable assumption of  $\kappa \approx 0.1$ . Recent experiments in a working mine<sup>67</sup> show that the coal dust concentration at the active face may be as high as 100 to 200 mg/m<sup>3</sup> and thus that  $\beta_{Mie}$  may be as large as 75 km<sup>-1</sup> at these dust levels. To further investigate the optical output requirements, an analysis of the various noise sources and their relative sizes must be made.

The signal-to-noise (S/N) power ratio of the returned signal in Equation 5.1 is given by<sup>148</sup>:

$$S/N = \frac{\overline{i_s^2}}{\overline{i_{SN}^2} + \overline{i_B^2} + \overline{i_D^2} + \overline{i_A^2}} \quad (5.4)$$

where  $\overline{i_s^2}$  = the averaged squared signal current,  $\overline{i_{SN}^2}$  = the averaged squared shot noise current,  $\overline{i_B^2}$  = the averaged squared background current,  $\overline{i_D^2}$  = the averaged squared detector dark current,  $\overline{i_A^2}$  = the averaged squared amplifier noise current. Standard expressions<sup>148</sup> for the various currents and their calculated numerical values are provided in Appendix D.

It can be ascertained from that appendix that

$$\overline{i_{SN}^2} : \overline{i_B^2} : \overline{i_D^2} : \overline{i_A^2} \approx 10^{-28} : 10^{-32} : 10^{-19} i_d : 10^{-31} \Delta\nu. \quad (5.5)$$

It has been shown<sup>149</sup> that  $\overline{i_A^2}$  can be reduced by orders of magnitude with current mode operational amplifiers so that noise source will not be considered further. It can also be seen from Equation 5.5 that  $\overline{i_B^2}$  is orders of magnitude less than  $\overline{i_{SN}^2}$  and thus may be ignored in the present context. To know more about the remaining two noise sources,  $\overline{i_{SN}^2}$  and  $\overline{i_D^2}$ , a numerical value must be attached to  $i_d$ , the detector dark current.

The magnitude of the detector dark current depends on a number device parameters and on the method of operation. When current mode operational amplification is used<sup>149</sup>, the best detection sensitivity is achieved at zero detector bias or for small reverse voltages. It is known<sup>150</sup> from load line analysis that linear operation is also achieved for near-zero bias. Thermally driven carrier generation-recombination is the source of dark noise near zero bias and its magnitude is given by

$$\overline{i_D^2} = \frac{4 K_B T \Delta\nu}{R_D} \quad (5.6)$$

where  $R_D$  is the detector shunt resistance. Substitution of a typical value  $\approx 10^6 \Omega$  for a typical small area commercial Ge detector<sup>150</sup> gives a value for  $\overline{i_D^2}$  some 60 times that of  $\overline{i_{SN}^2}$ , the quantum detection limit. Recently, extensive work has gone into the development and improvement of detectors for the 1.1 to 1.7  $\mu\text{m}$  range. That work has been spurred by the growth of optical fiber technology, and the desire to operate fiber optic systems at wavelengths of minimum absorption and dispersion<sup>151, 103</sup>. In efforts to develop new germanium avalanche photodiodes, dark current densities near  $10^{-3}$  Amp/cm<sup>2</sup> have been reported<sup>152, 153</sup> for room temperature large reverse bias operation. These current densities are slightly lower than those of the best commercially available devices and those of the HRL methanometer<sup>150</sup>. However, these kinds of devices cannot be expected to show decreased noise at zero bias since the generation-recombination noise source is the same as that of previous germanium devices.

Alternative detectors to germanium have been in active development. They are based on the quaternary  $\text{In}_x\text{Ga}_{1-x}\text{As}_y\text{P}_{1-y}$  system of direct-gap III-V semicon-

ductors. These can be lattice matched to GaAs for short wavelengths, and to InP for the longer wavelengths for fiber optics applications and for methane detection. This recent work on such detectors<sup>100,105,154-158,102,159,160</sup> parallels the work, based on much of the same technology, of laser diode source development in that quaternary system.

In particular, Pearsall reported<sup>102</sup> production of new InGaAs/InP photodiode structure with a dark current density of  $3 \times 10^{-7}$  Amps/cm<sup>2</sup> at room temperature and a 1 volt reverse bias. The novelty of this device arises from physical separation of the photon absorption and depletion regions. Such a separation would not be possible below the direct bandgap threshold in a semiconductor such as germanium (ie. for  $\lambda > 1.5 \mu\text{m}$ ). By placing the depletion region in the high bandgap ( $\lambda \approx 0.9 \mu\text{m}$ ) InP portion, generation-recombination of carriers is minimized thus reducing the dark current and the generation-recombination noise associated with it. Thus a back biased dark current of 3 to 4 orders of magnitude smaller than in the best Ge devices is achieved. Pearsall also notes that the photon quantum efficiency is nearly 100% for  $\lambda = 1.65 \mu\text{m}$  when the light is incident on the epitaxial side. That is a different situation from germanium for which the useful absorption decreases dramatically below the  $1.5 \mu\text{m}$  bandgap. Thus, with this type of detector, near shot noise limited operation is obtainable under the conditions described above and in Appendix D.

Due to the technical developments discussed above, high sensitivity back-side illuminated GaInAsP/InP detectors have recently been introduced to the commercial market. A typical such device<sup>161</sup> has a sensitivity of -55 dBm at a  $10^{-9}$  bit error rate (BER) and a bandwidth of 5 MHz. A BER of  $10^{-9}$  is equivalent<sup>148</sup> to a signal to noise ratio (SNR) of 11:1 and 5 MHz is the bandwidth appropriate to a 100

ns optical pulse. Thus, this detector can detect  $3 \times 10^{-9}$  watts of optical power near  $1.6 \mu\text{m}$  with a signal to noise ratio of 11:1. Using Equation 5.3, an optical output power of 100 mW would yield a SNR of 3.5:1 for a single pulse of light backscattered from  $40 \text{ mg/m}^3$  of coal dust at a distance of 16 feet or  $200 \text{ mg/m}^3$  at 35 feet.

Having obtained the value for the theoretically possible voltage SNR, the needed ratio for a DIAL measurement must be ascertained. This will be done in the next section.

#### 5.4 SNR: Pulse Repetition Frequency Considerations

The federal requirements for a portable methane detector are shown in Table 5.1. It may be seen from the table that the allowed fractional errors in the measured methane concentration vary from  $\pm 0.6$  at  $0.25\% \text{ CH}_4$  to  $\pm 0.075$  at  $4\% \text{ CH}_4$ . The law<sup>144</sup> further requires for approval that a methane monitor must fall within the indicated errors in at least eight out of ten trials.

In Appendix C the inversion of the fundamental RDIAL expression, Equation 5.1 is derived. Equation C.17, therein, shows the completed inversion and is given by

$$\bar{C} = \frac{C(r_2 - r_1)}{2(R_1 - R_2)} \frac{\ln \left( \frac{V_{r,on}(R_2)}{V_{r,on}(R_1)} \right) - \ln \left( \frac{V_{r,off}(R_2)}{V_{r,off}(R_1)} \right)}{\ln \left( \frac{V_{on,1}}{V_{on,2}} \right) - \ln \left( \frac{V_{off,1}}{V_{off,2}} \right)}. \quad (5.7)$$

in the notation of the appendix. That appendix in its second section also contains a detailed derivation of the error propagation inherent in the RDIAL measurement. A simple expression for the maximum allowable normalized standard deviation in

the measured voltages as a function of the required gas concentration and the amount of absorption in the sample volume during the on line portion of the RDIAL process is given in Equation C.28 and is given by

$$\frac{\sigma_V}{V} = \frac{1}{2} \frac{\sigma_C}{C} \left[ \ln \left( \frac{V_{r.on}(R_2)}{V_{r.on}(R_1)} \right) \right] \quad (5.8)$$

Substitution of  $\alpha C$  for the quantity inside the absolute value bars in Equation 5.8 yields

$$\frac{\sigma_V}{V} = \frac{\sigma_C \alpha}{2} \quad (5.9)$$

where  $\alpha$  is the on-line absorption coefficient  $\approx 8.1$  from Section 3.3 for a  $0.2 \text{ cm}^{-1}$  source bandwidth. Evaluation of Equation 5.9 using the most restrictive condition on  $\sigma_C$  in Table 5.1 yields a required voltage SNR of 160:1.

Further consideration of the required SNR is required here in light of the statutory stipulation that an indicating methane monitor must satisfy the requirements laid out by Table 5.1 in only eight out of ten trials. Assume that the source of error in the methane measurement is random with a zero mean normal distribution. Then the probability of the measured  $\text{CH}_4$  concentration differing from the true value by more than two standard deviations is  $4.54\%^{162}$ . The requirement that eight out of ten measurements meet a specified accuracy suggests that the failure probability in the trials be calculated using a binomial distribution, with  $p = 0.0454$ ,  $q = 1-p = 0.9546$ , and  $n = 10$ . It is easily shown by such a calculation that a  $\text{SNR} = 320:1$  would pass the federal requirements nearly  $99\%$  of any tests. Comparison of this SNR with the single pulse SNR of 3.5:1 derived above reveals the

need for a signal to noise improvement ratio (SNIR) of approximately 90:1. Signal averaging techniques can be used to improve the SNR.

One method of averaging often used with low duty cycle signals is the so-called boxcar method<sup>163</sup>. Boxcar averaging yields a SNIR<sup>164</sup>

$$\text{SNIR} = \left[ \frac{2N}{5} \right]^{1/2} \quad (5.10)$$

where  $N$  is the number of pulses to be integrated. This method of integration is best used for large instantaneous signal low duty cycle averaging. Further enhancement to the SNIR beyond that of Equation 5.10 can be produced in this mode through preintegration techniques<sup>163</sup> when sufficiently large instantaneous signals are available. However, in the present context the returned optical signal is not large relative to noise sources, so preintegration techniques are not feasible. Moreover, boxcar averaging is a nonlinear integration process that favors the last signals received and thus can introduce systematic errors in a non-stationary process. It will be seen below that the DIAL measurement process when averaged over many pulses is typically non-stationary. It will also be shown below that a SNIR greater than that of Equation 5.10 can be achieved by a digital signal processing method.

In recent years, there have been several investigations into the various sources of error in the DIAL measurement accuracy<sup>165-167,34,168,169</sup> and into the signal processing techniques needed to minimize the errors<sup>170-172,33,173,174</sup>. DIAL return signals are randomly affected by turbulence induced fluctuations in the absorber concentration, scintillation, beam wander, speckle, and the angle of arrival and by electronic noise. Additionally, differential reflectivity and differential background extinction are sources of systematic error in DIAL measurements.

It was shown in Chapter 3 that differential background extinction due to any of the normal constituents of air or coal gas is satisfactory for DIAL measurements in the wavelength region of the  $2\nu_3$  overtone of methane. Furthermore, it was mentioned in Section 5.2 that the differential reflectivity from coal dust aerosols typical to coal mines was observed to not affect the backscattered light over a few wavenumber region near the  $1.65 \mu\text{m}$  wavelength of an Er:YAG laser. So, the last two potential sources of systematic error are not a problem for a diode laser DIAL methane measurement at  $1.65 \mu\text{m}$  in coal mines. The various sources of potential random signal errors must now be considered in turn.

The signal fluctuations caused by atmospheric turbulence and electronic noise may be classified by the degree of temporal correlation that they possess between on- and off-line portions of the DIAL process. Electronic noise between signal channels in a DIAL system is uncorrelated and may be reduced through averaging techniques by the factor  $N^{-1/2}$  where  $N$  is the number of samples averaged. Thus a SNIR of  $N^{-1/2}$  is possible for signals affected by such noise.

Of the several atmospheric sources of potentially correlated noise, the latter four mentioned above should be minimal. Beam wander and angle of arrival variations would be negligible because of the short ( $\approx 10\text{m}$ ) path length for a coal mine measurement. Scintillation effects should also be negligible<sup>165</sup> for a receiver aperture radius

$$R \geq (\lambda L)^{1/2} \quad (5.11)$$

where  $\lambda$  is the laser wavelength and  $L$  is DIAL total path length.  $(\lambda L)^{1/2}$  is a transverse coherence length and is equal to approximately 4 mm for a 10 m path length and a wavelength of  $1.65 \mu\text{m}$ . Last, speckle effects should be nonexistent

since the bandwidth gives, as shown in Section 3.3, a longitudinal coherence length less than the length of the scattering volume.

For periods of less than 1 to 10 milliseconds the atmosphere is "frozen"<sup>166,175</sup>. That is to say, for such periods the effects of turbulence on the two returned signals of a DIAL process are correlated. Thus, fluctuations of the returned signals because of methane concentration variations are correlated during this time interval.

It has been shown by Menyuk and Killinger<sup>173</sup> that when the returned light pulses during the on- and off-line parts of the DIAL process arrive within the correlation time of the atmosphere subsequent signal averaging over many pulses diverges from the  $N^{-1/2}$  improvement mentioned above for independent measurements. They found that the SNIR was less than  $N^{-1/2}$  if the signals were averaged as

$$C = \text{constant} \times \ln \left[ \frac{\langle V_{i,1} \rangle}{\langle V_{i,2} \rangle} \right] \quad (5.12)$$

where  $\langle \rangle$  represents time averaging. On the other hand, they found that the SNIR was greater than  $N^{-1/2}$  for signals averaged as

$$C = \text{constant} \times \ln \left[ \left\langle \frac{V_{i,1}}{V_{i,2}} \right\rangle \right]. \quad (5.13)$$

They attribute these properties to a high cross-correlation between the on- and off-line pairs and residual auto-correlation over many pulses because of the non-stationary nature of the absorber concentration. Menyuk et al. have recently presented a summary<sup>176</sup> of the various parameters that influence DIAL measurement errors. Here it will be assumed that a SNIR of at least  $N^{-1/2}$  can be achieved



for a coal mine DIAL process with the latter signal processing method.

So, in a period of less than 1 second at a 10 kHz data collection rate a sufficient SNIR can be achieved to meet the SNR requirements derived earlier in this section provided the source properties presented in the last chapter can be modified to match those required by the derivations of this chapter. This is the next topic to be examined.

## 6. SOURCE OPTICAL DESIGN

This chapter brings together many of the previous topics. First, a review of the DIAL requirements and source properties is presented in Section 6.1. Next, in Section 6.2, external resonator diode lasers are introduced as a means of matching the diode laser characteristics to the DIAL requirements. In that section, the theory of linewidth narrowing in external grating cavities is discussed. Third, the advantages of reflective optics for an external cavity at a wavelength of  $1.65 \mu\text{m}$  are presented in Section 6.3. In the last section, 6.4, the development and application of a ray-trace computer program to an off-axis parabolic mirror cavity is explained.

### 6.1 Review of Diode Source Characteristics and the DIAL Requirements

The properties of high optical power diode lasers as presented in Chapter 4 do not all match well with those source requirements developed in Chapters 3 and 5. This section presents, in review, the various characteristics discussed in those three chapters.

Most properties of broad area  $\text{In}_{0.53}\text{Ga}_{0.47}\text{As}/\text{InP}$  diode lasers are suitable for a coal mine RDIAL methane measurement. The achievable optical output power,  $\approx 100 \text{ mW}$ , was shown to be sufficient in Chapter 5. The measured lifetimes at pulse

repetition frequencies of 10 kHz represent a potentially long period of service in a methanometer. The PRF possible is sufficient to obtain the necessary SNIR in less than one second. Also, the TM polarization characteristic described in Chapter 4, although not typical to most InGaAs/InP semiconductor lasers, is the polarization needed for operation in an external grating cavity.

Furthermore, the operating wavelength of  $\text{In}_{0.53}\text{Ga}_{0.47}\text{As}/\text{InP}$  lasers is near the  $2\nu_3$  absorption band of methane. However, the typical spectral bandwidth at this wavelength, as shown in Figure 4.3 is much greater than the  $\approx 0.05$  nm width required for sufficient absorption to make DIAL process feasible. Thus, a method is needed to control the bandwidth and wavelength while maintaining the other diode laser properties.

## 6.2 External Resonator Diode Lasers

No simple diode source can be made to satisfy, simultaneously all the requirements presented above. It is possible to achieve high optical power with broad active region or phase-locked array devices. However, this implies a broad spectral output as was shown, for example, in Chapter 4. Conversely, stripe geometry lasers yield a narrow spectral bandwidth but at low power. There are however means of solution of this circumstance.

All lasers consist of a gain medium and a resonator cavity for electromagnetic wave feedback. The cavity is physically defined by mirrors. For simple diode lasers the mirrors are cleaved facets parallel to the crystal planes of the as grown semiconductor. To modify the spectral, or any other, properties of a laser it is necessary to modify its internal characteristics (ie. the gain medium or resonator cavity).

External resonator diode lasers have been used for many purposes. The goals have been modification of the temporal<sup>177-182</sup> and spectral<sup>183-192</sup> properties normally observed. Numerous studies have been made of the intrinsic properties of diode lasers in external cavities or near reflecting surfaces, such as lens, optical fibres, or optical disks<sup>193-206</sup>. The most recent review paper<sup>207</sup> on diode lasers coupled to external resonators was published in 1979.

Almost all published accounts of **continuous** wavelength tuning and bandwidth control of diode lasers have reported on antireflection (AR) coated devices<sup>183-186,188,191</sup> in external cavities. The few exceptions<sup>208,209</sup> have involved low power single stripe devices in complicated temperature and current controlled servo-loops. By continuous wavelength tuning it is meant that the tuning resolution is much greater than the spectral separation of the diode laser modes. By AR coating the diode laser, its original facet reflectivity is nullified and thus the cavity can be extended to some external optical element. This allows access to the cavity and it is then possible to insert a wavelength controlling element such as an etalon, birefringent filter, or grating. In the present project an external 600 l/mm grating blazed for operation at  $\approx 1.6 \mu\text{m}$  was substituted for one facet mirror after the facet was AR coated with a SiO coating. The grating, by selectively feeding back only a narrow spectral bandwidth of optical power to the active volume of the diode, forces the laser to oscillate in a limited spectral region. It be should noted here that in at least one previous case<sup>193</sup> the facet reflectivity was nullified by lapping the facet at Brewster's angle with respect the active region. However, this method produces localized mechanical damage to the laser and severely degrades its lifetime.

It has been shown<sup>210, 211</sup> that a dielectric film with index of refraction given by

$$n_f = \left( n_L n_{ext} \right)^{1/2} \quad (6.1)$$

and thickness given by

$$t = \frac{\lambda}{4n_f} \quad (6.2)$$

where  $n_L$  is the effective index of refraction in the laser,  $n_{ext}$  is the external index,  $n_{ext} = 1$  for air, and  $\lambda$  is the vacuum wavelength of the laser radiation, gives a theoretical air-laser reflectivity of near zero. Thus by this coating technique a diode's emission may be decoupled from its normal oscillator modes and its spectral output may be controlled by substitution of a variable dispersion external cavity. This type of coating was used for this project. The results for a SiO coating are shown in Section 7.2.

Injection lasers exhibit homogeneous broadening<sup>212</sup> and thus may collapse<sup>195</sup> their wide filamentary lasing action into a narrow spectral region when they are employed in an external dispersive cavity. Furthermore this spectral narrowing may be done with little or no expense to the optical output power due to the homogeneous nature of the broadening.

The resulting bandwidth of an external grating cavity may be obtained from the standard grating equation as shown by Heckscher and Rossi<sup>186</sup> and is given by

$$\Delta\lambda = \frac{\lambda d}{2f \tan(\theta)} \quad (6.3)$$

where  $d$  is the active region thickness,  $f$  is the laser to grating collimating optics

focal length, and  $\theta$  is the grating angle of incidence for a grating in a Littrow mount. This formula was derived using geometric optics. Substitution of numerical values appropriate to the present project,  $\lambda = 1.65 \mu\text{m}$ ,  $d = 0.65 \mu\text{m}$ ,  $f = 25 \text{ mm}$ , and  $\theta = 30$  degrees as calculated from the grating equation<sup>210</sup> for a 600 1/mm grating, yields a bandwidth of  $\Delta\lambda = 0.04 \text{ nm}$ . It is demonstrated in Chapter 7 that the bandwidth achieved during this project has never equaled that predicted by Equation 6.3. Therefore, it is important to ascertain if indeed this formula holds under a more sophisticated analysis of the spectral bandwidth.

A better estimate of the bandwidth to be expected from an external grating cavity can be achieved using coupled-mode theory of guided electromagnetic waves<sup>213</sup>. Many recent developments<sup>214-217</sup> in coupled mode theory have been driven by the interest in coupling the optical output of diode lasers to various types of waveguides, for example to optical fibres or thin films. Since a diode laser active region is itself a waveguide, it is appropriate to think of the coupling of the returned light from an external grating to the diode laser as a diode laser to waveguide problem. A revised estimate of the achievable spectral bandwidth is calculated in Appendix E using coupled-mode theory.

The derivation presented in Appendix E yields an expected bandwidth of 0.1 nm for a 2 times threshold drive current. This spectral width is 2.5 times that calculated by the generally accepted geometric optics method and is, as shown in Chapter 7, closer to that observed in experiments. It should be pointed out that this wider bandwidth reduces the absorption that may be achieved below that calculated in Chapter 3.

The degree to which an external grating can control the wavelength and bandwidth depends on the efficiency of the AR coating in suppressing residual modes

of the diode laser cavity and on the reflective efficiency of the grating. It is known<sup>218</sup> that a diffraction grating is effective only for light polarized perpendicular to its grooves. In a narrow bandwidth external grating diode laser cavity the grating grooves must be in the plane of the active region to ensure that the small dimension of the junction acts as a slit that rejects all but the desired part of the spectrally dispersed fed-back light. Because of this alignment, the fed-back light is then polarized perpendicularly to the active region plane, that is it is TM polarized. If the diode laser is intrinsically TM polarized, the returned optical power couples with the laser gain medium better than does TE polarized light. It was shown in Chapter 4 that the lasers used in the present project are TM polarized which is advantageous for use in an external grating cavity.

It was shown in Section 5.4 that a significant signal to noise improvement ratio (SNIR) could be achieved for the DIAL process when the on- and off-line portions of the process were temporally separated by less than the decorrelation time of the atmosphere, ie. less than 1 to 10 ms. Double pulse DIAL systems have been used to take advantage of the improved SNIR. These systems have either used the combined output of two laser cavities operating at separate wavelengths<sup>219</sup> or have used a movable wavelength control element in a single cavity<sup>220</sup>. The former scheme suffers from duplication of all cavity components while the latter is necessarily slow because of mechanical inertia. For an external grating resonator diode laser system, a second diode laser may be placed adjacent to the first in the cavity. This second laser will be located at a slightly different angle to the grating relative to the angle of first laser and will oscillate at a different wavelength. So, the on- and off-line portions of the DIAL process could be initiated by alternate electrical drive pulses to the two diodes. This pulse scheme, with a 10 kHz interlace rate, was

implemented for this project and its mechanical and electronic construction are described in Chapter 7.

A final point about external resonator diode lasers: it is necessary to calculate the angular positioning stability required for the grating to maintain the wavelength of the light fed-back to the diode laser active volume within the bandwidth calculated in Appendix E. A simple trigonometric argument that ratios half the effective slit width to the focal length of the collimator optics gives that the angular stability must be given for small angles by

$$\Delta\theta < \frac{d}{2f} \tag{6.4}$$

where the symbols are those defined following Equation 6.3. Numerical substitution yields  $\Delta\theta < 25$  microradians.

Having explored external grating resonator diode lasers, it is now necessary to examine the means of optically coupling the diode laser and the grating. This is the topic of the next section.

### 6.3 Reflective Optics for an External Grating Cavity

Although exotic alternatives such as holographic optical elements are conceivable as the diode laser to grating coupler, common sense engineering suggests that refractive lenses or mirrors are more appropriate. Mirrors for use in the near infrared can be classified in turn into two categories: dielectric film and metal.

Work with refractive optics at the wavelength in question is both unusual and difficult. The difficulty arises from the low index of refraction of glasses,  $n \approx 1.4$ , at



1.65  $\mu\text{m}$  wavelength. So, it is necessary when using glasses to have either more, or more powerful, optical elements to duplicate the effects achieved at visible wavelengths. During this project, several optical design and fabrication businesses were contacted regarding design and construction of a lens system to couple a 1.65  $\mu\text{m}$  wavelength diode laser to a diffraction grating. Only one company, Research Optical Systems Group, Inc., (ROSG) was willing to bid on design and fabrication of such a device.

The pre-design plans from ROSG called for a five or six element glass lens system or a three or four element silicon lens system. The former would suffer from only 83-86 % optical throughput because of reflection and scattering from the large number of optical surfaces involved and additionally would be bulky. The latter would be difficult to align since silicon is opaque to visible radiation. Implementation of either design would have been prohibitive due to engineering and tooling costs. The large number of problems associated with refractive optics made reflective optics more attractive for this project. Hence, it was decided to design a reflective laser-grating coupling system.

Since the coupling of the diode laser to a grating is from a finite conjugate point to an infinite conjugate, the mirror shape that would seem to give minimum optical aberration is parabolic. Furthermore, an unobstructed optical path from the diode laser to the grating requires an off-axis parabola. The focal length,  $f$ , needed to give adequate bandwidth, as discussed in the preceding section, along with the lateral dimension of the mirror needed to capture most of the rapidly diverging light emitted by the diode laser, see Section 4.4, necessitate a drastically curved parabolic surface as will be explained below.

Dielectric thin film coatings are commonly used to achieve high reflectivity in the NIR. However, these coatings are difficult to fabricate on surfaces of much curvature. All the commercial coating houses contacted during the project declined to become involved in a job of this nature.

Metal mirrors are the other possibility for reflective optics in the NIR. In particular, aluminum mirrors are both light weight and have a reflectance of over 96% at a wavelength of 1.65  $\mu\text{m}$  at normal incidence<sup>221</sup>. At other than normal incidence the reflectance increases and at any angle the reflectance is much greater than the total transmission for a multi-element refractive collimator. On this basis, an aluminum off-axis paraboloid of revolution was chosen as best for this project. Furthermore, for ease in aligning the mirror to the rest of the external cavity components, it was decided to use a right-angle off-axis paraboloid. That is to say, the axis of rotation of the paraboloid would be perpendicular to the axis of the diode laser emission.

The required dimensions, such as focal length and angular swing, for a right angle paraboloid may be determined with the help of Figure 6.1. The figure shows a cross-section parallel to the axis of revolution of the paraboloid. The restricting conditions on parameters displayed in the figure are as follows. The diode laser is located at  $(F,0,0)$  where  $F$  is the focal length of the paraboloid.  $\alpha_1 - \alpha_2$  must equal the beam divergence of the diode laser to gather most of the light emitted.  $\frac{\alpha_1 + \alpha_2}{2} = 90$  degrees so that the paraboloid is right angle off-axis. The positions along the  $y$  axis where the laser half-angle points intersect the parabola are  $y_1$  and  $y_2$ . The apparent width of the diffraction grating as seen from the parabola is given by  $y_2 - y_1$ . That is  $y_2 - y_1 = D \cos \theta$  where  $D$  is the width of the grating and  $\theta$  is the

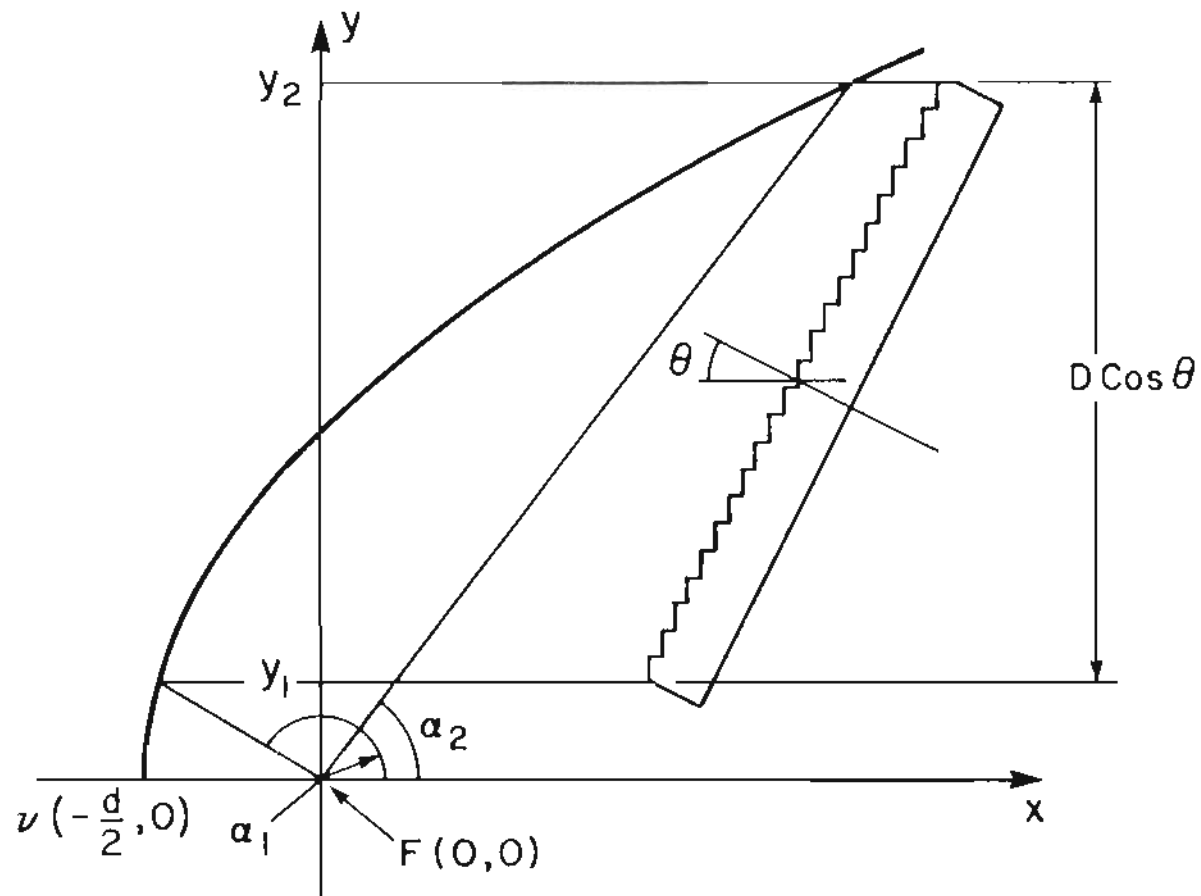


Figure 6.1 Cross-section of the external grating cavity parallel to optic axis of parabolic mirror.

angle of incidence of light on the grating which is  $\approx 30$  degrees for a 600 l/mm grating. The width of the grating used for the present work is approximately 58 mm. Simultaneous solution of the expressions for  $\alpha_1$  and  $\alpha_2$  gives  $\alpha_1 = 125$  degrees and  $\alpha_2 = 55$  degrees. Substitution of the polar formula for a parabola into the above equations and solution for  $f$ , the focal length of the parabola, yields  $f = 17.8519$  mm.

Before proceeding with construction of an off-axis parabolic mirror the optical aberrations that would be present in the folded external cavity as shown in Figure 6.1 were determined.

#### 6.4 Aberrations in an Off-Axis Parabolic Cavity

It was stated above that optical aberrations of an external cavity diode laser to grating coupler would be minimized with a parabolic collimator. It is the purpose of this section to show that such a mirror is indeed aberration free for the purposes at hand.

The cavity as shown in Figure 6.1 is optically equivalent to a folded Ebert-Fastie<sup>222</sup> monochromator modified to use off-axis parabolic mirrors in a Littrow configuration<sup>223</sup> as originally suggested by Welford<sup>224</sup> where the normal monochromator entrance and exit slit function is accomplished by the small dimension of the laser active region. Ebert-Fastie-Welford (EBW) monochromators are now widely used and their optical properties have been thoroughly studied<sup>225-227</sup>. It has been shown<sup>223</sup> that EBW devices are third order aberration free near the optic axis.

To determine how critical the placement of the diode laser in the right angle cavity of Figure 6.1 would be in determining its optical aberrations, a computer ray tracing program was written to simulate the cavity. The program name is

CAVITY and Appendix F contains the basic language source listing of this program as written for the OGC Prime computer. The program carries out its calculations using geometrical optics ray tracing; no diffraction effects are introduced into the calculations. Additionally, no aberration effects are introduced for the diffraction grating since gratings in a Littrow configuration are anamorphic<sup>223, 228</sup>.

The program can perform three functions. First, it can display, with graphical assistance from the OGC Prime Graphics Editor, the simulated off-axis parabolic cavity with optical rays shown. There may be as many rays as are convenient for the program user. Furthermore, the rays may be initialized by either direct specification of their origin and initial direction or a two dimensional Gaussian angular probability distribution with two independent full-width half maximum angles may be specified for a given origin. Figure 6.2 shows a typical ray-trace output. In the figure, the rays leave from the focal point of the paraboloid with angles perpendicular to the active region of  $\pm 35, \pm 25, \pm 15$ , and 0 degrees and at 0 degrees in the plane of the junction.

Second, the program can calculate and display spot diagrams of the light returned to the diode laser facet. For this latter type of display it is advantageous to be able to determine the spot diagram for laser facets that have been rotated in the plane of Figure 6.2 or translated. This capability is integral to the program. Here, the Gaussian angular probability distribution provisions of the program may be used to simulate the beam divergence of the diode lasers as described in Chapter 4. Moreover, the program creates, when used in this mode, statistical data in separate Prime disk files on the the beam size perpendicular and parallel to the active region.

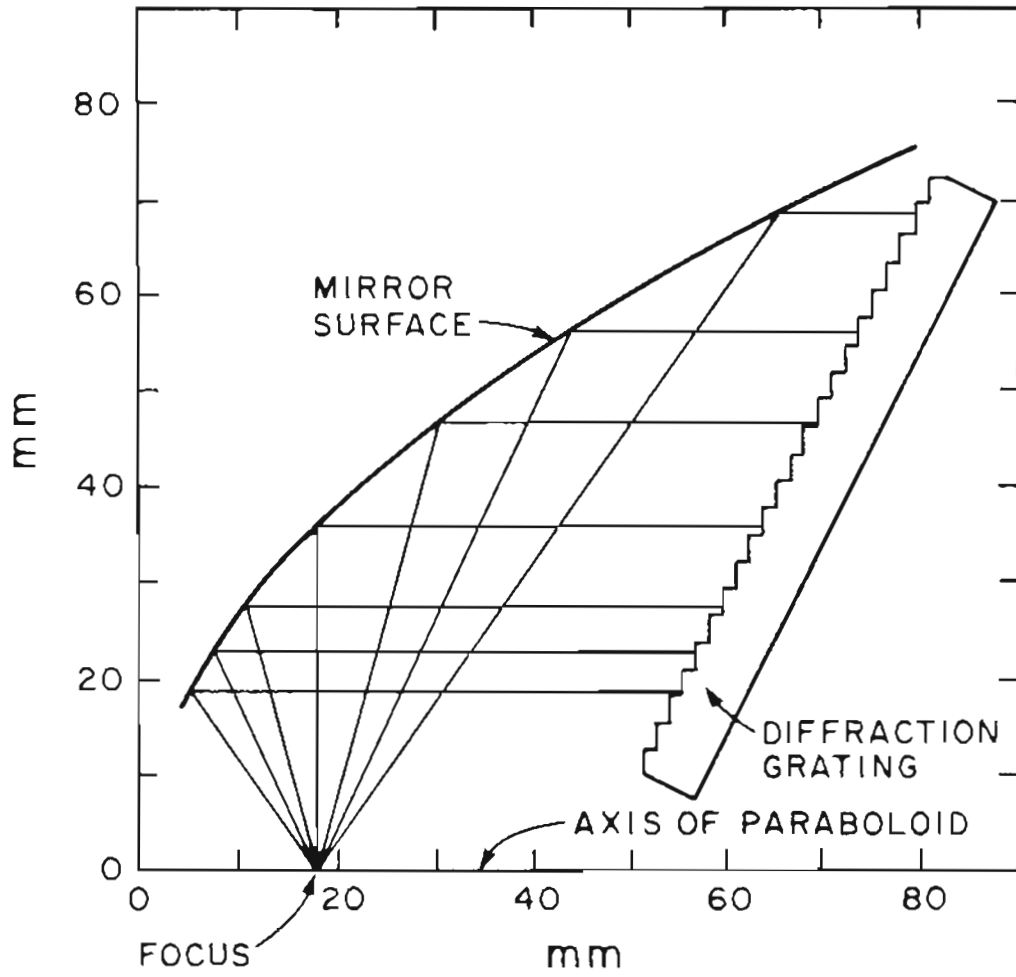


Figure 6.2 Graphic output from ray trace program CAVITY for the off-axis parabolic external grating diode laser cavity.

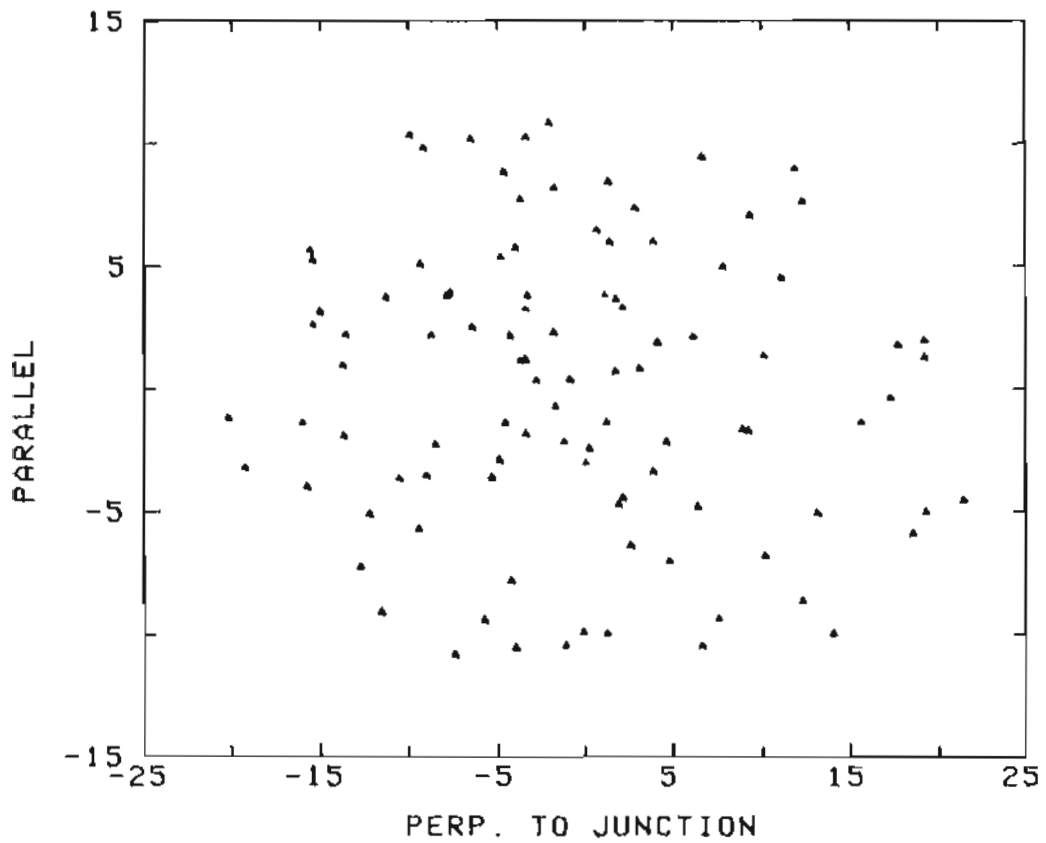


Figure 6.3 CAVITY generated spot diagram in the plane of the diode laser facet for Gaussian angular probability optical output distributions perpendicular and parallel to the active region. The diode laser is  $30 \mu\text{m}$  from the optic axis of the parabola. The axes units are  $\mu\text{m}$ .

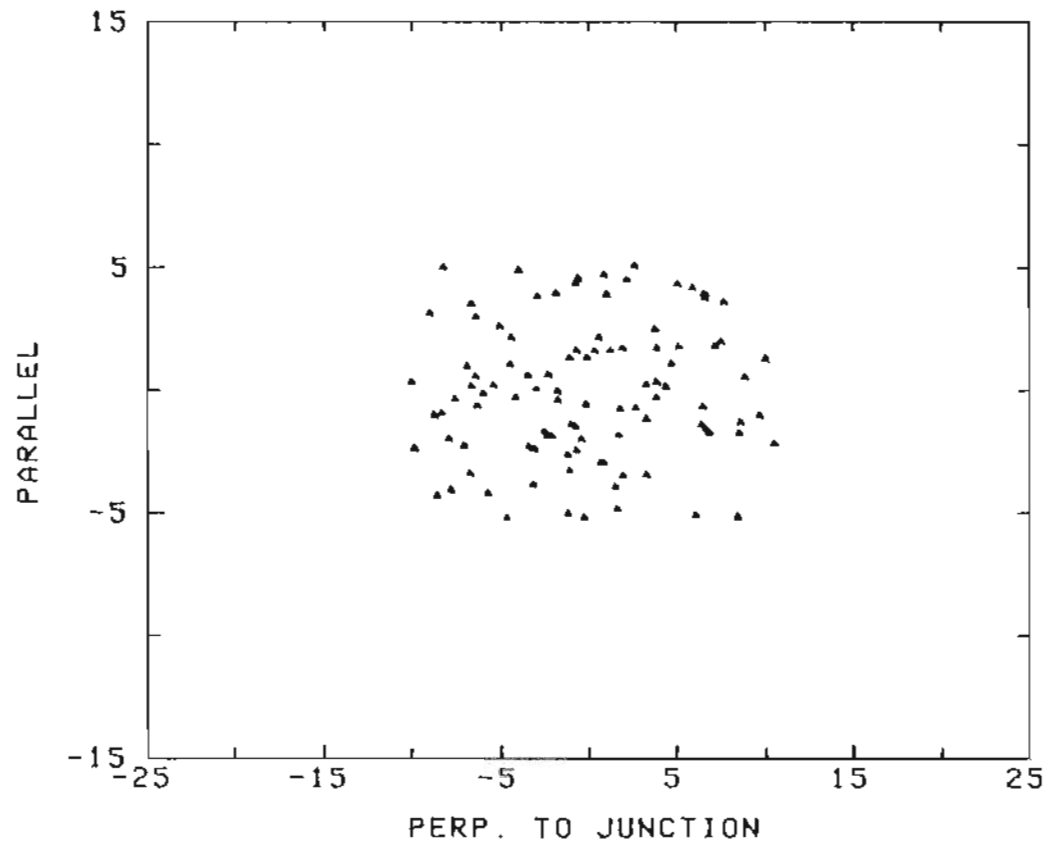


Figure 6.4 CAVITY generated spot diagram in the plane of the diode laser facet for Gaussian angular probability optical output distributions perpendicular and parallel to the active region. The diode laser is  $15 \mu\text{m}$  from the optic axis of the parabola. The axes units are  $\mu\text{m}$ .



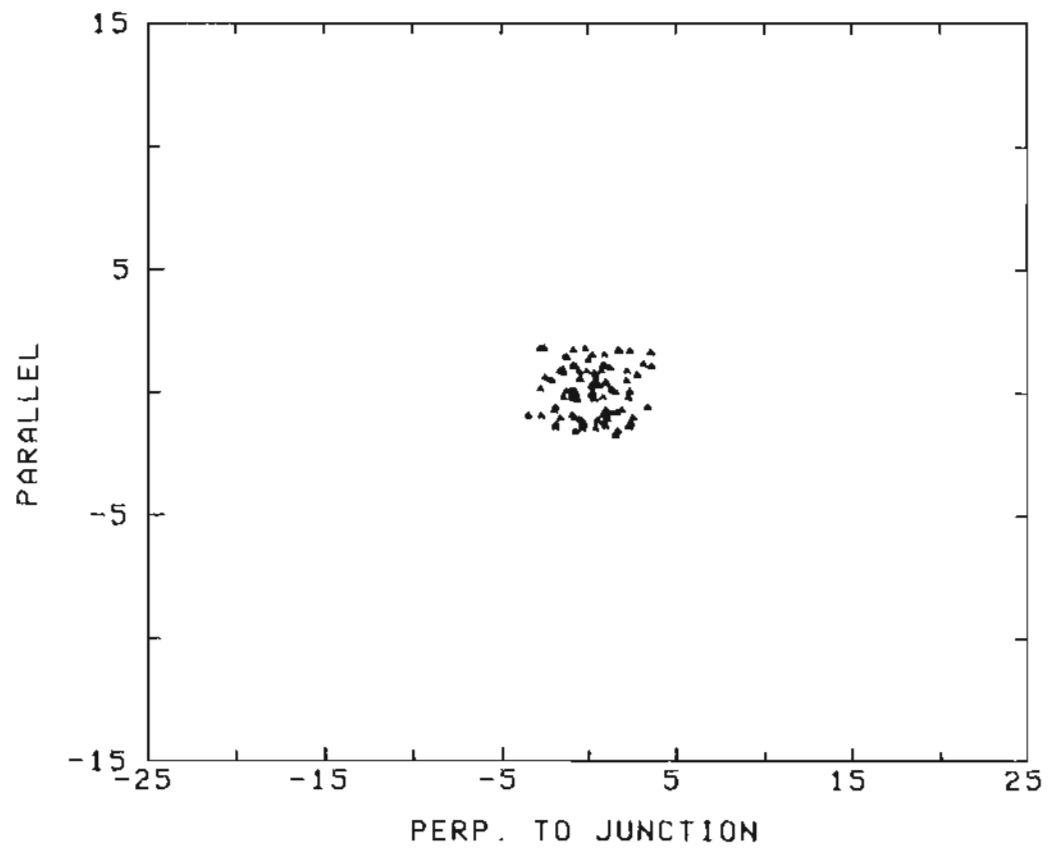


Figure 6.5 CAVITY generated spot diagram in the plane of the diode laser facet for Gaussian angular probability optical output distributions perpendicular and parallel to the active region. The diode laser is  $5 \mu\text{m}$  from the optic axis of the parabola. The axes units are  $\mu\text{m}$ .

Figures 6.3 through 6.5 show spot diagrams as generated by CAVITY. The figures represent the returning light spot for 100 rays initially launched from  $(F,0,0)$  with Gaussian angular probability distributions both perpendicular and parallel to the active layer. Full width half maximum angles of 70 and 50 degrees, respectively, were used to generate the diagrams. In Figure 6.3, the laser facet has been translated 30  $\mu\text{m}$  orthogonal to the axis of the paraboloid and away from it, i.e. away from the focal point. In Figures 6.4 and 6.5 the translation direction is the same but the distances are 15 and 5  $\mu\text{m}$ , respectively. From these figures it is easily seen that the spot size generated by the returning rays rapidly changes and so alignment along this direction is critical for optimal coupling of the returned light to the diode active layer. The spot diagram with no displacement shows a point spot on the scale of the previous diagrams. The radius of the spot is on the order of  $10^{-9}$  microns and the calculation is at this level double precision computationally limited. The operation for a properly placed diode is then aberration free and the figures indicate that placement of the diode laser along this direction must be within  $\pm 1\mu\text{m}$  for the aberration induced spot size to be less than the active region thickness. Similar diagrams with the ray origin at  $(F,\pm 0.050\text{mm},\pm 0.050\text{mm})$  yield spot radii less than the active region thickness. The external grating cavity diode laser is therefore optically aberration free under the restricted use described here.

Last, the program when operated in the Gaussian angle mode creates a spot diagram in the plane of the grating. Figure 6.6 is a graphical representation of that diagram. It may be seen from the figure that the illumination at the grating is not uniform and thus diffraction effects are not simply dependent on the grating width.

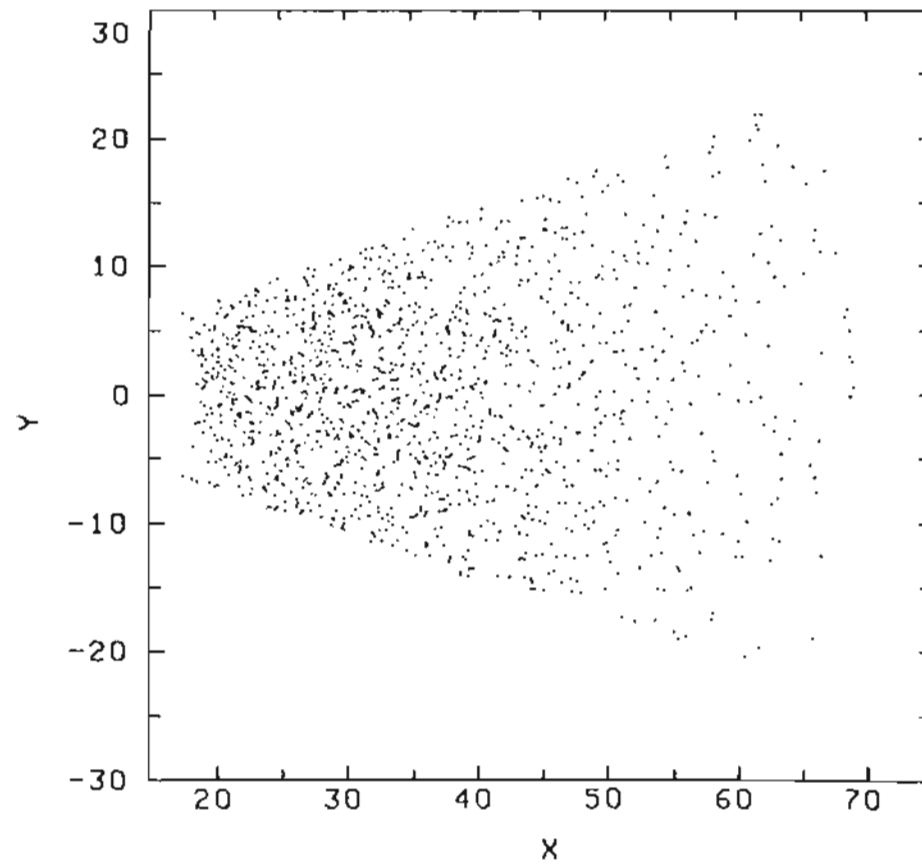


Figure 6.6 CAVITY generated spot diagram in a plane orthogonal to the optic axis of the parabolic mirror and at the position of the grating. The axes units are mm.

## 7. AN EXTERNAL CAVITY SOURCE

The previous chapters have presented the requirements for and the optical design of an external grating cavity diode laser source for a DIAL methanometer. This chapter describes the construction and performance of such a source. Section 7.1 delineates the source mechanical construction. Section 7.2 explains the antireflection coating process used to minimize the coupling between the diode laser and its normal oscillation modes. In the third section, 7.3, an electronic wavelength control system is described. Also in that section, a dual diode pulser is described. The last section, 7.4, shows the source performance.

### 7.1 Mechanical Construction

Figure 7.1 shows the physical realization of the off-axis parabolic cavity described in Chapter 6 and schematically shown in Figure 6.2. The cavity includes a diamond-machined off-axis parabolic mirror, a diffraction grating mounted on a gimbal mount, a motorized micrometer for positioning the grating, a mount for two diode lasers, and a XYZ translation stage for positioning of the two diode lasers in the cavity. Each of the cavity components is described below.

Figure 7.2 gives a view of the off-axis parabolic mirror. The drastic curvature of the diamond machined surface is evident from the figure. Figure 7.3 is a repro-

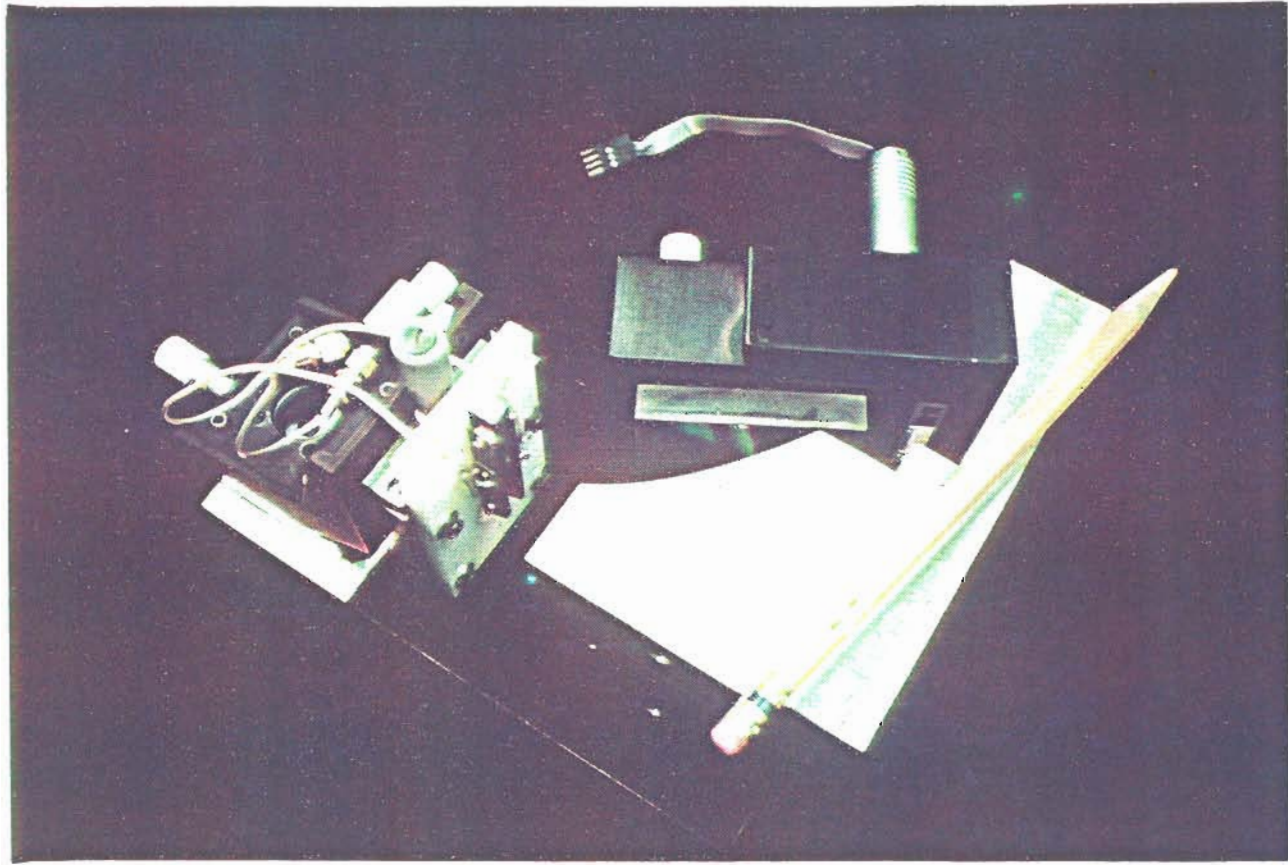


Figure 7.1 The dual diode laser external off-axis parabolic mirror grating cavity source. Shown are the off-axis parabolic mirror, the grating and its positioner, and the dual diode laser mount and its positioner.

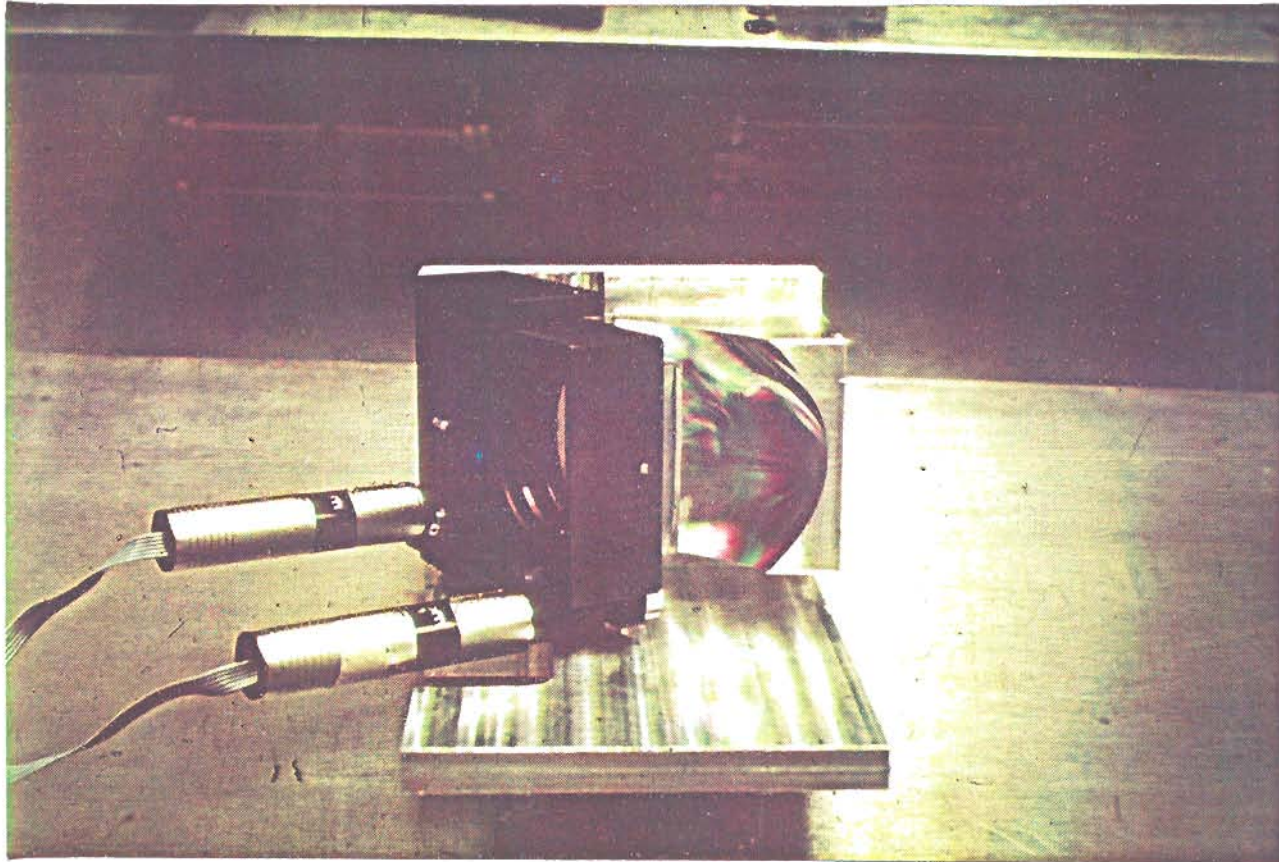


Figure 7.2 The off-axis parabolic mirror with the diamond-machined surface presented.

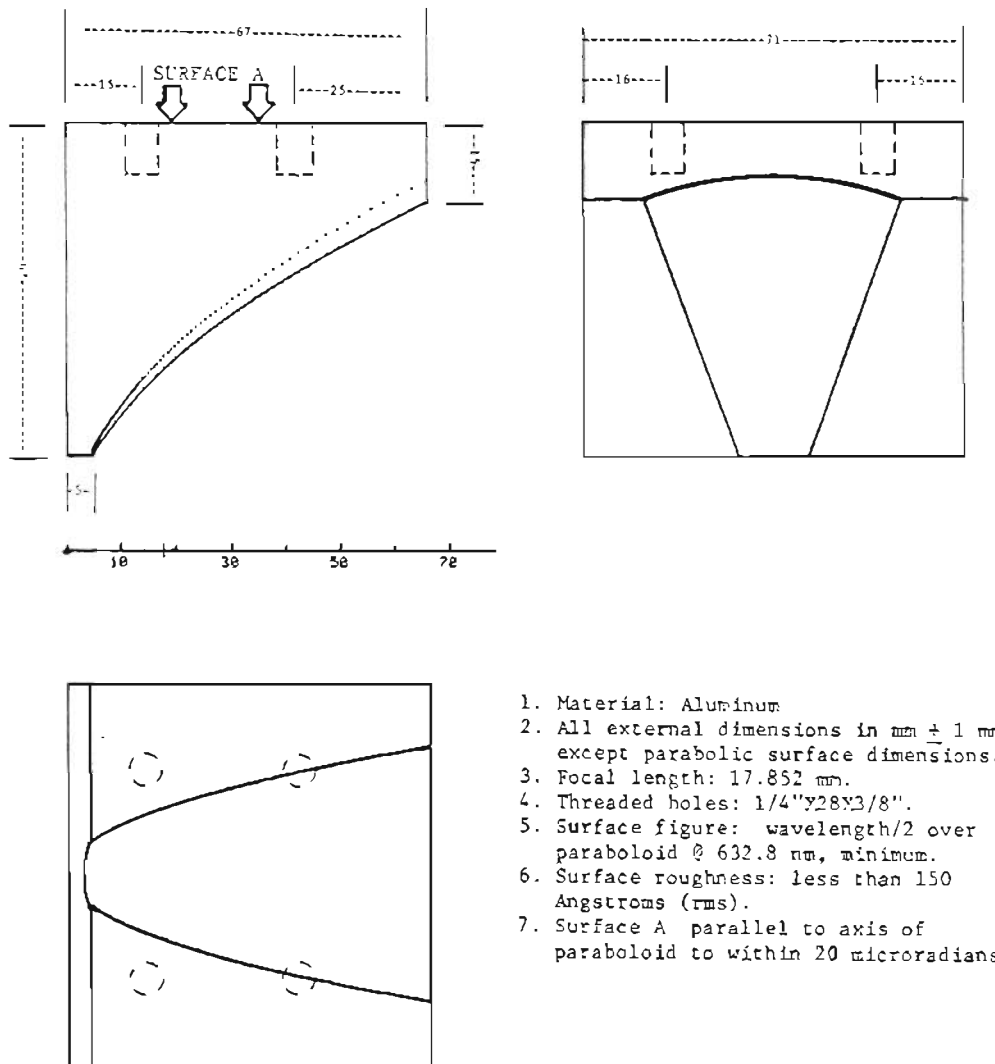


Figure 7.3 Technical specification drawing for mirror of Figure 7.2.

duction of the technical specification drawing for the mirror as given to Pneumo Precision, Inc. for machining in March 1983. The drawing was computer generated using the OGC Prime Graphics Editor. Included with the drawing are several technical requirements. In particular, the mirror is fabricated in aluminum with a 17.852 mm focal length as was suggested in Chapter 6. The surface figure is specified as  $\lambda/2$  at a He-Ne laser wavelength which is equivalent to  $\lambda/5.2$  at a wavelength of 1.65  $\mu\text{m}$ . Also, the RMS surface roughness is required to be 150 Angstroms or less.

The finished mirrors were tested against the specifications in tests at Pneumo Precision and at OGC. The focal length and surface figure were examined for compliance with specifications at Pneumo Precision. The surface figure was shown to meet specifications using optical interferometric techniques. Acceptance tests conducted at OGC included measurements of the mirror reflectivity and total integrated scattering. Reflectivity at  $45^\circ$  incidence with 633 nm He-Ne laser light was measured to be 87% for the sum of the specularly reflected spot and the scattered light. Figure 7.4 shows a trace of light output versus angular position for one location on the mirror. In the figure, the small fluctuations to the sides of the center spot are scattered light and represent less than 5% of the total reflected light at 633 nm. The total integrated scattering (TIS) is inversely proportional to the square of the wavelength through the relation<sup>229</sup>

$$\text{TIS} = \left[ \frac{4\pi\delta\cos(\theta)}{\lambda} \right]^2 \quad (7.1)$$

where  $\delta$  is the RMS surface roughness,  $\lambda$  is the wavelength, and  $\theta$  is the angle of incidence. Using Equation 7.1 and the measurement at 633 nm the TIS at 1.65  $\mu\text{m}$



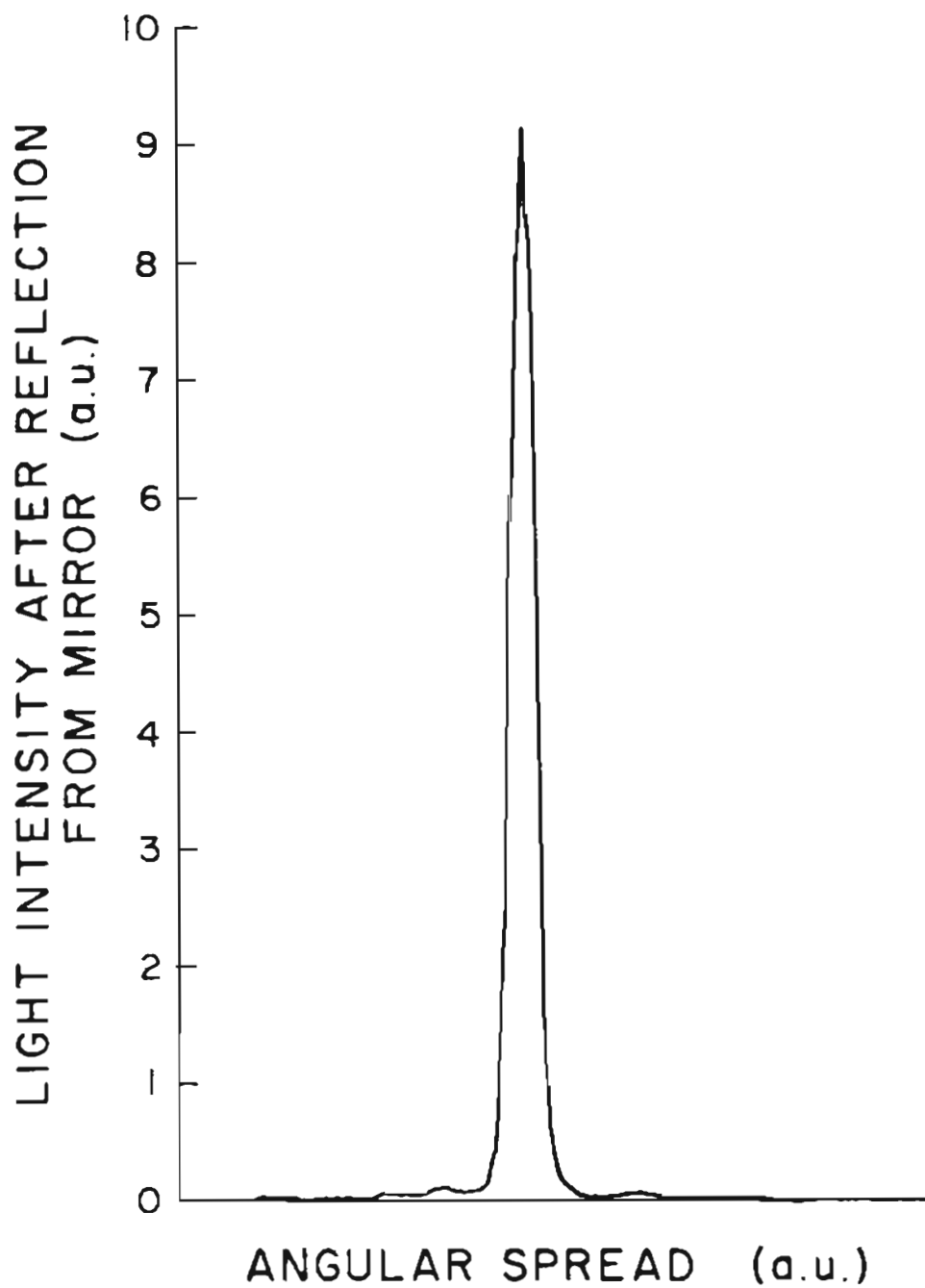


Figure 7.4 Surface reflected light vs. scattered angle for the mirror of Figure 7.2.

is calculated to be less than 1%. Coupled with the 87% reflectivity mentioned above and the higher reflectivity of aluminum at  $1.65 \mu\text{m}$ , a specular reflectivity of 96% is calculated. The RMS surface roughness, calculated from the measured values for TIS, angle of incidence, and wavelength, is 160 Angstroms, which is within the measurement uncertainty of the 150 Angstrom specification

The diffraction grating is a 600 l/mm replica fabricated with aluminum on epoxy on glass. It is blazed at  $29^\circ 41'$  for use in the first order at  $1.6 \mu\text{m}$  in a Littrow configuration. Nominal reflectivity at  $1.65 \mu\text{m}$  into the first order is 70%. The grating holder is an Ardel Gimbal 20-25 series mount.

There are three means by which the grating and gimbal mount could be automatically rotated and electronically controlled to ensure proper wavelength selection. The first method involves using piezoelectric translators<sup>230</sup> attached to manual micrometers. This technique suffers from the high voltages ( $\approx 1 \text{ kV}$ ) necessary to drive piezoelectric stacks over distances on the order of  $1 \mu\text{m}$ . The second method involves use of micro-stepped stepper motors<sup>231</sup>. The stepper motor technique is similar to that using DC motors with optical shaft encoder readout however the stepper motors are typically more bulky. The third method, and the one used for this project, entails use of DC motor driven micrometers with optical shaft encoder position readout.

The motorized micrometer shown in Figure 7.1 is an engineering run Ardel Kinematic MotorMike<sup>TM</sup> Model 17213 with position readout capability. Position readout is achieved via TTL level electrical pulses from an optical shaft encoder<sup>232</sup> and has a linear travel precision of  $0.1 \mu\text{m}$  with a backlash limited accuracy of approximately  $3 \mu\text{m}$ . A  $0.1 \mu\text{m}$  position precision is equivalent, through the 1 inch lever angle of the gimbal mount, to a 4 microradian angular position precision.

Such precision is six times the angular resolution required as determined by Equation 6.4. The means by which this precision is converted to angular positioning accuracy is described in Section 7.3.

Double pulse LIDAR measurements, with an interpulse temporal separation of less than 1 ms, were shown in Section 5.4 to be advantageous from a signal processing standpoint. In Section 6.2, the concept of using two diode lasers in the same external grating cavity was introduced as a means of achieving a short interpulse period where the two lasers were placed at slightly different angles to the diffraction grating thus producing slightly different lasing wavelengths. The external cavity displayed in Figure 7.1 contains two such diode lasers in a brass mount.

Figures 7.5 and 7.6 are perspective drawings of the dual diode mount. Figure 7.7 is a close-up photograph of part of the same mount. In the figures, two lasers are shown to be positioned with their p contacts adjacent and contacting a gold strap conductor. The strap has approximate dimensions of  $25\ \mu\text{m}$  by  $250\ \mu\text{m}$  by 1 cm and was machined at OGC from  $25\ \mu\text{m}$  thick commercial Au foil with a frequency doubled Nd:YAG laser. The n contacts of the lasers rest on gold plated diamond heat sinks<sup>233-237</sup>. Diamond heat sinks were chosen for this application because of their flat surface (cleaved planes) and parallel faces ( $< 10'$ ) and because the thermal conductivity of Type IIa diamond<sup>234</sup> is five times that of copper at room temperature. The lasers were hand positioned in the mount using a special function jig which featured an integral optical flat to ensure optical alignment of the diodes.

The aberrations in an off-axis parabolic grating cavity were discussed in Section 6.4. It was shown in that section that placement of the diode laser, regarding optical aberrations, was critical only along the the optic axis of laser. The

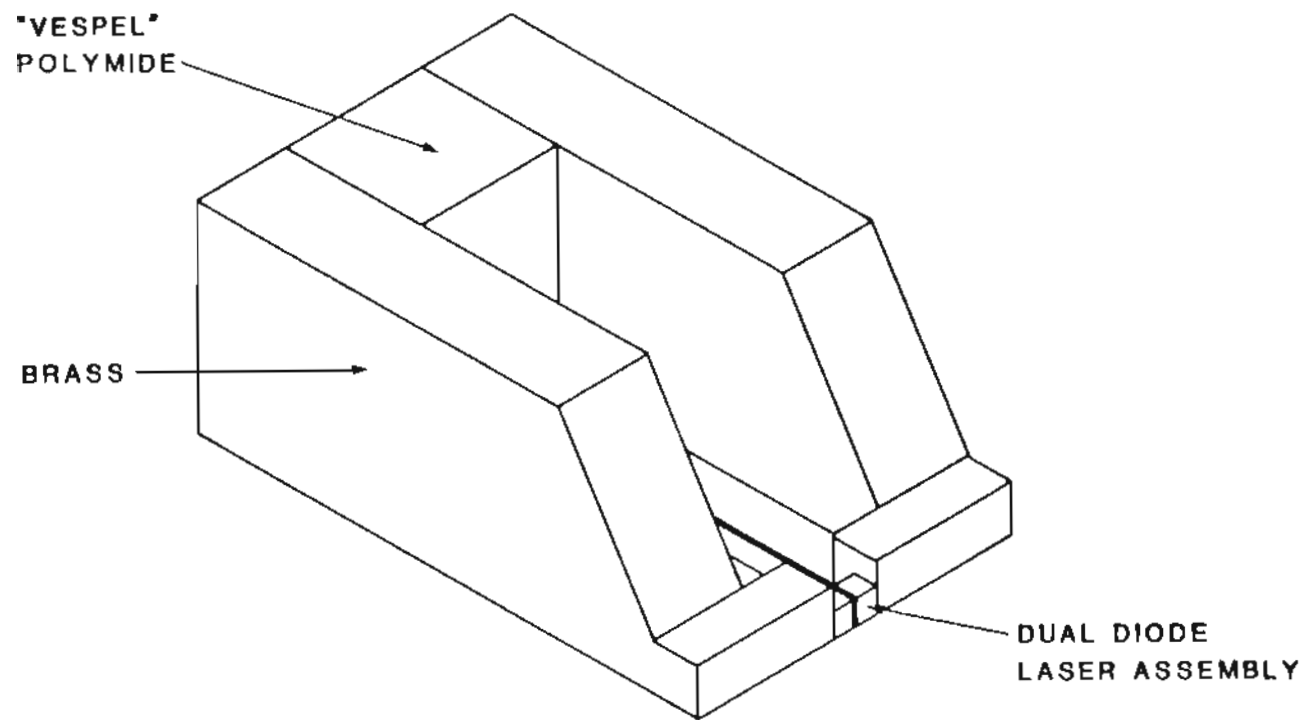


Figure 7.5 Perspective drawing of the dual diode laser mount.

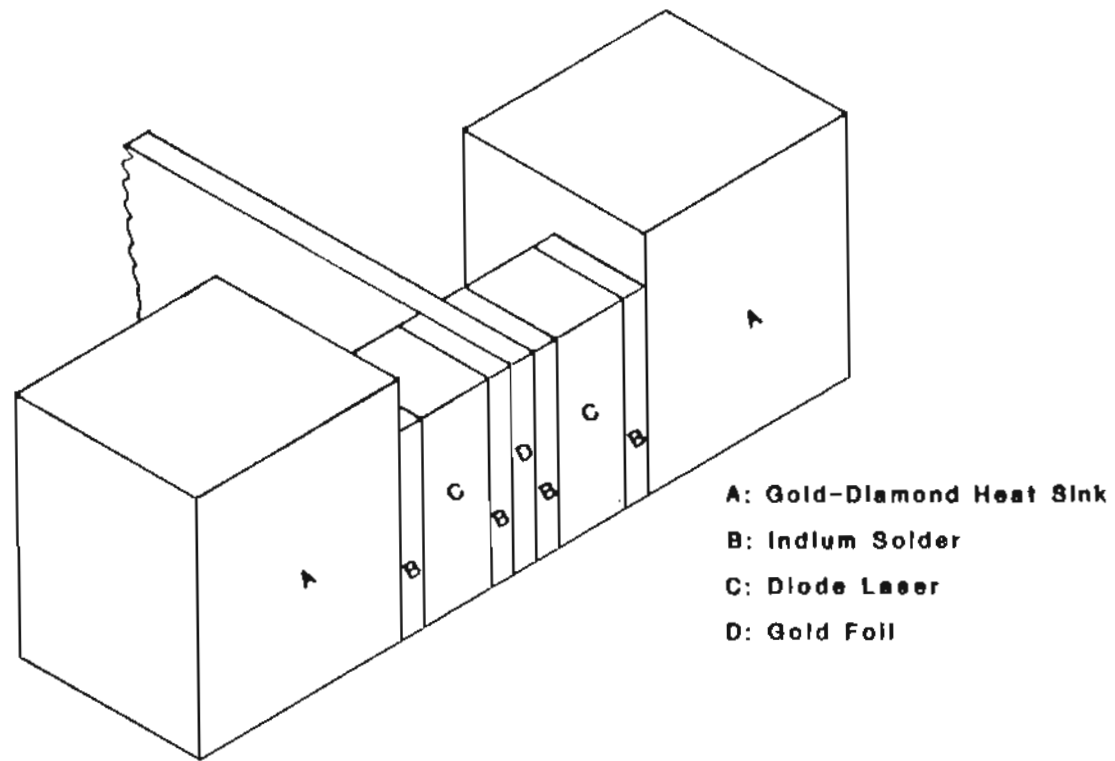


Figure 7.6 Detail drawing of the dual diode laser mount. Shown are the diode lasers and their heat sinks and indium bonding pads.

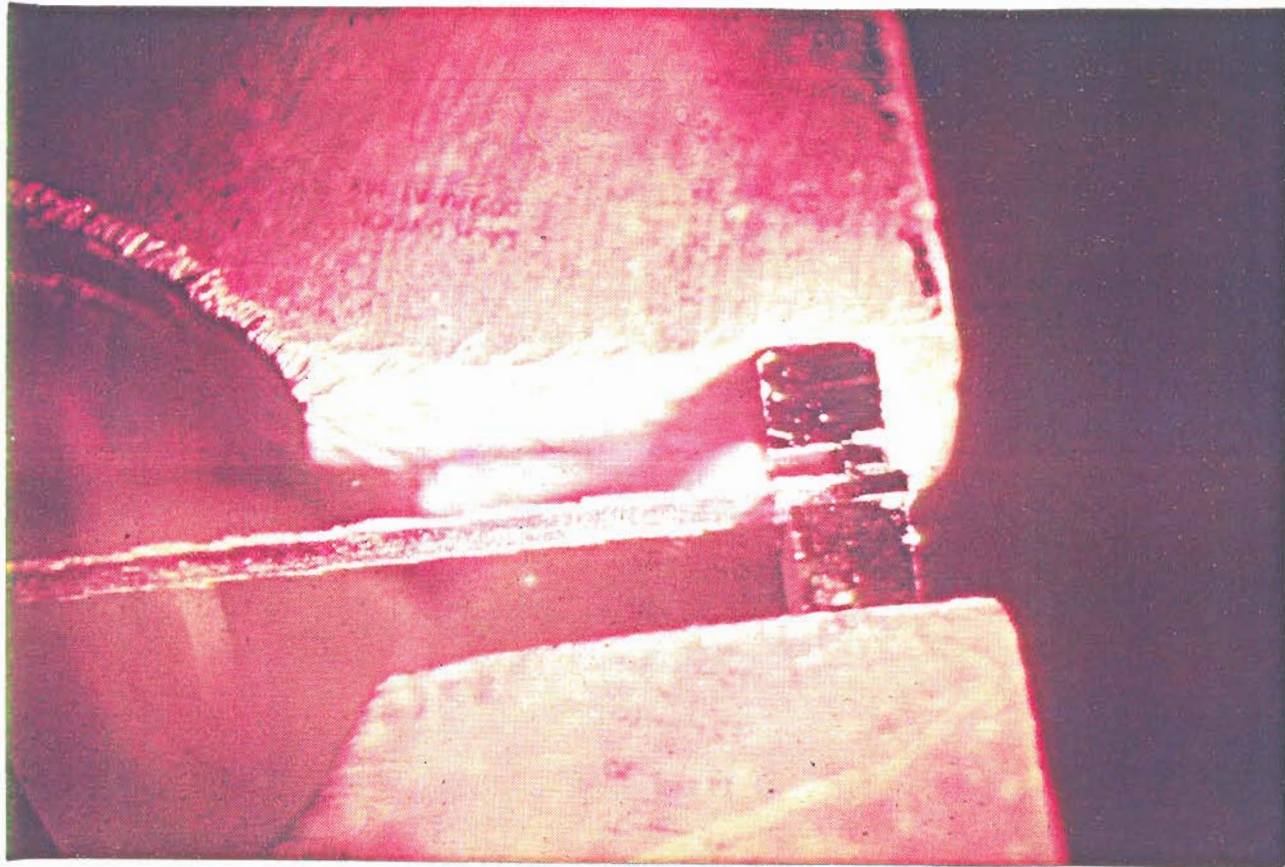


Figure 7.7 Photograph of that portion of the dual diode mount shown in Figure 7.6.

positioning stage shown in Figure 7.1 is a Klinger, Model MR-50, micropositioning device featuring manual micrometer adjustment in a plane parallel to the axis of rotation of the paraboloid and manual differential micrometer adjustment orthogonal to the axis. The former adjustments have a sensitivity of  $1 \mu\text{m}$  while the latter has a sensitivity of  $0.1 \mu\text{m}$ . This precision is necessitated by the aberration requirements discussed in Section 6.4 and is achieved with an enhanced version of the standard MR-50. Before the diode lasers were mounted in the dual diode mount and installed in the external cavity, they were AR coated to decouple their light output from their normal cavity modes. The antireflection coating process is the subject of the next section.

## 7.2 Antireflection Coating

Dielectric thin films are often used for antireflection coatings on semiconductor devices. A dielectric film with index of refraction given by

$$n_f = \left( n_L n_{\text{ext}} \right)^{1/2} \quad (7.2)$$

and thickness given by

$$t = \frac{\lambda}{4n_f} \quad (7.3)$$

gives a theoretical air-laser reflectivity of near zero (see Section 6.2). There are many methods<sup>238, 239</sup>, including thermal evaporation, sputtering, plasma deposition, and chemical vapor deposition, by which such a coating might be applied to a diode laser. However, most AR coatings for light emitting diodes and diode lasers that have been reported in the literature<sup>240-243, 183, 185, 179, 203</sup> have used coatings thermally or e-beam evaporated from  $\text{SiO}_2$ , although e-beam evaporation of  $\text{ZrO}_2$ ,<sup>186</sup>

and sputtering of  $\text{Si}_3\text{N}_4$ <sup>244</sup> among other techniques have also been successful. Because of the large amount of information available about thermally evaporated SiO and its properties, this method of creating AR coatings was used on the present project.

The physical properties of evaporated SiO coatings have been well studied<sup>245-248</sup>. The index of refraction of SiO rapidly evaporated ( $> 10$  Angstroms/second) under vacuum conditions of less than  $1 \times 10^{-5}$  torr has been shown to be approximately 1.85 with negligible absorption near a wavelength of  $1.65 \mu\text{m}$ . The effective index of refraction for the diode lasers used in the present project has been previously shown<sup>249</sup> to be 3.52. Since the square root of 3.52 is 1.88, SiO can be seen, through Equation 7.2, to be a good AR material for these lasers.

There are two methods to achieve an optimum index-thickness combination for a single layer film. One method is to calculate<sup>211,250,251</sup> the optimum index and thickness from the properties of the particular diode laser using guided wave theory and then to create those properties for the coating. This method requires strict knowledge and control of the coating process and has recently been put into use to sputter  $\text{Si}_3\text{N}_4$  onto laser facets<sup>244</sup>. The second, and much simpler, method<sup>242</sup> uses a substance with approximately the right index of refraction as given by Equation 7.2 and then monitors the reflectivity looking for a minimum as the coating thickness increases. This technique was used on this project.

The SiO AR coatings were deposited from a Drumheller oven, Electronic Space Products, Inc. (ESPI) Part No. ESPI KVAC-477, using evaporation grade SiO, ESPI K4698C, at a background pressure of  $10^{-7}$  to  $10^{-6}$  torr. Figure 7.8 shows the setup for monitoring the reflectivity in real time. In the figure, the current pulser drives



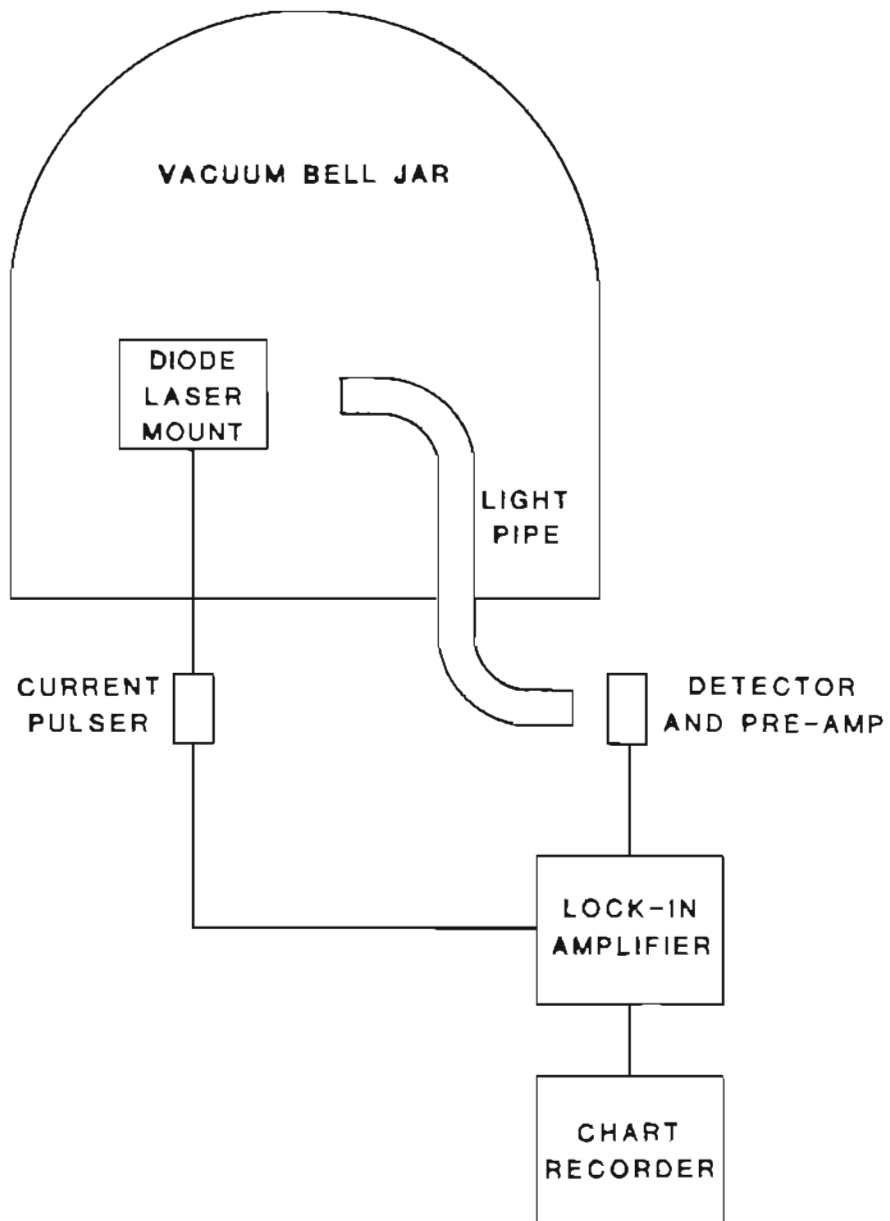


Figure 7.8 Setup for in situ monitoring of the antireflection coating thickness during deposition.

the diode laser at a point below lasing threshold so that the diode emits only spontaneous emission. The light pipe shown in the figure carries light from the vacuum chamber to a Ge detector and preamp outside the chamber. The resultant signal was synchronously detected with a lockin amplifier, EG&G 5101, at the pulse repetition rate. The output from the lockin amplifier was recorded with a stripchart recorder. As the SiO coating was deposited the amount of light escaping the diode laser facet varied thus giving a record in real time of the coating efficiency.

Figure 7.9 shows the recorder output for a test AR coating deposited on a Laser Diodes Labs Model LCW-5 continuous wave 5 milliwatt optical output diode laser. The recorder plot is light output versus time. For this run a sine-wave generator was substituted for the pulser since the lockin amplifier intrinsically responds more efficiently to such a modulation signal. In the figure, each peak in light output indicates an odd multiple of quarter wavelengths for the coating thickness, while the troughs indicate a half wavelength thickness. The coating rate is approximately 16 Angstroms/second. The overall trend downward with time is caused by increased scattering and absorption in the coating. The after-coating reflectivity may be estimated from

$$I_A = I_o \left( 1 - R_A \right) \quad (7.4)$$

and

$$I_B = I_o \left( 1 - R_B \right) \quad (7.5)$$

where  $I_A$  and  $I_B$  are the laser light outputs after and before coating, respectively,  $I_o$  is the light intensity inside the facet, and  $R_A$  and  $R_B$  are the facet reflectivities after and before coating. Equation 7.5 may be divided into Equation 7.4 to solve for  $R_A$

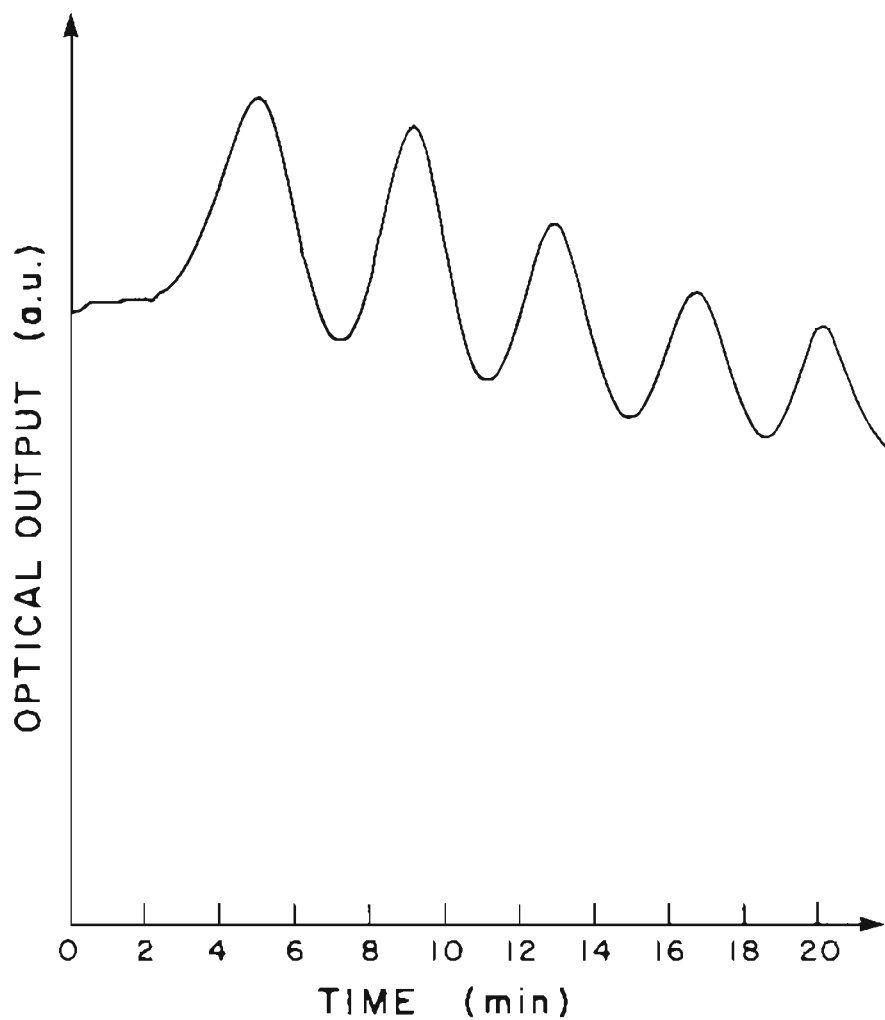


Figure 7.9 Optical output vs. time during deposition of a SiO<sub>2</sub> antireflection coating on a Laser Diode Labs Model LCW-5 diode laser. The evaporation process is stopped at a 3λ coating thickness.

using  $R_B \approx 0.32$  for the LDL laser and the  $\lambda/4$  peak in the figure. The resultant value of  $R_A$  is 0.10 and would have been lower had not the device already had a commercial  $\lambda/2$  coating on its output facet.

Figure 7.10 shows an example of a chart recorder trace for an AR coating applied to one of the diode lasers used in the present project. In this case, the evaporation process was terminated at a coating thickness of  $\lambda/4$  to achieve minimum absorption and scattering. Calculation of the residual reflectivity in the manner presented above yields  $R_A \approx 1\%$ . After the coating was applied to the laser, which had a lasing threshold of 2 Amps before coating, it did not lase at currents greater than 6 Amps. Figure 7.11 shows a typical before- and after-coating light output versus drive current curve. In the figure, the lower curve is the light output from the uncoated facet after AR coating. The effect of the AR film on the lasing threshold is obvious from the figure.

The first attempts at AR film deposition were not as successful as those represented in the figures above: the early films tended to peel from the diode laser facet along lines parallel to the active region. The probable cause of this defect was determined to be anisotropic stress<sup>252</sup> in the SiO film. Rotation of the evaporation angle of incidence to the laser facet from normal to 40 degrees off-normal eliminated the peeling problem. Subsequent film depositions exhibited another defect in which the films peeled off in narrow bands on the output facet along the facet intersection with the epitaxial layer interfaces. This type of defect occurred during prolonged operation in the external cavity and was attributed to localized heating at the interfaces, possibly to due to nonradiative carrier recombination at those sites. Careful chemical pre-cleaning of the diode laser facets along with argon glow discharge sputtering of the facet just before evaporation eliminated this coating

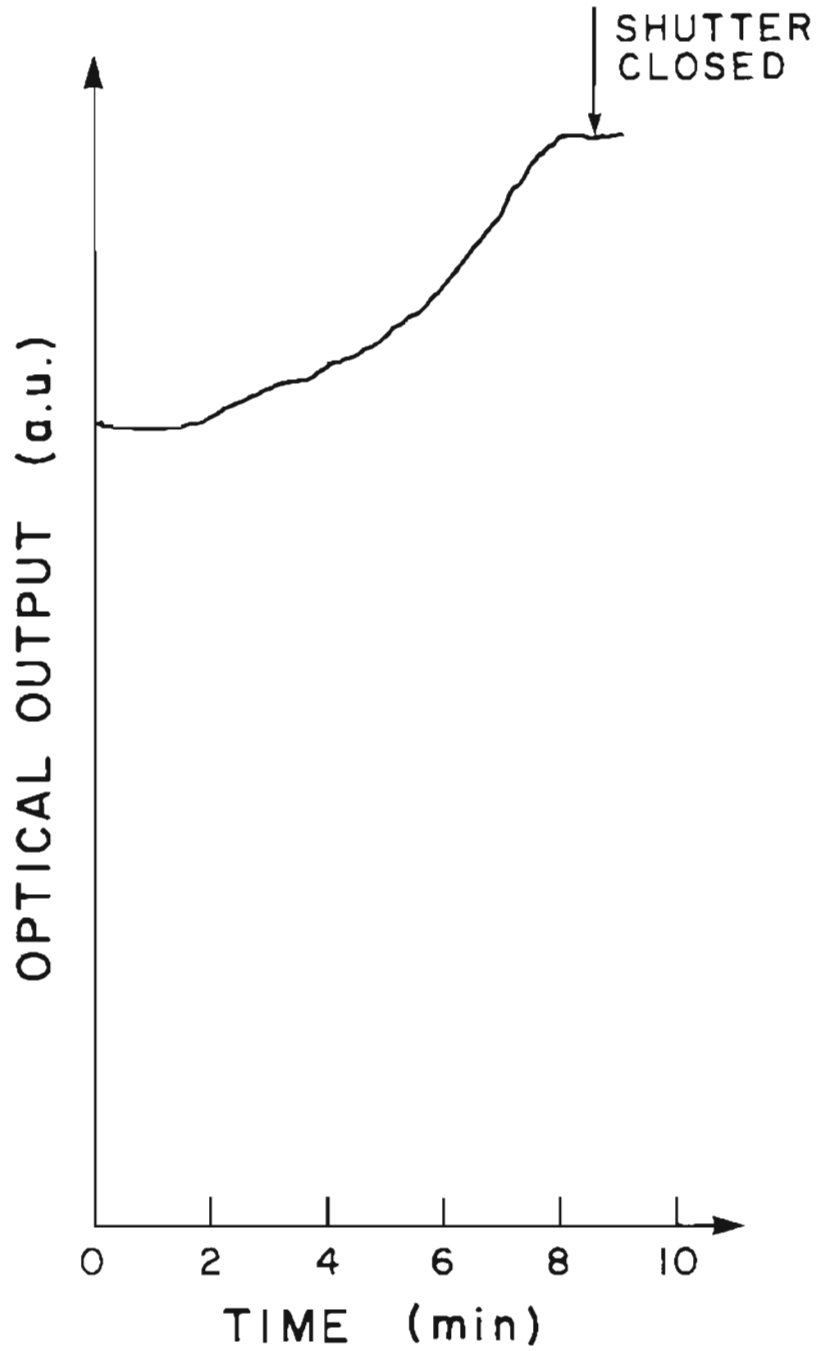


Figure 7.10 Optical output vs. time during deposition of a SiO antireflection coating on an InGaAs/InP diode laser. The evaporation process is stopped at a  $\lambda/4$  coating thickness.

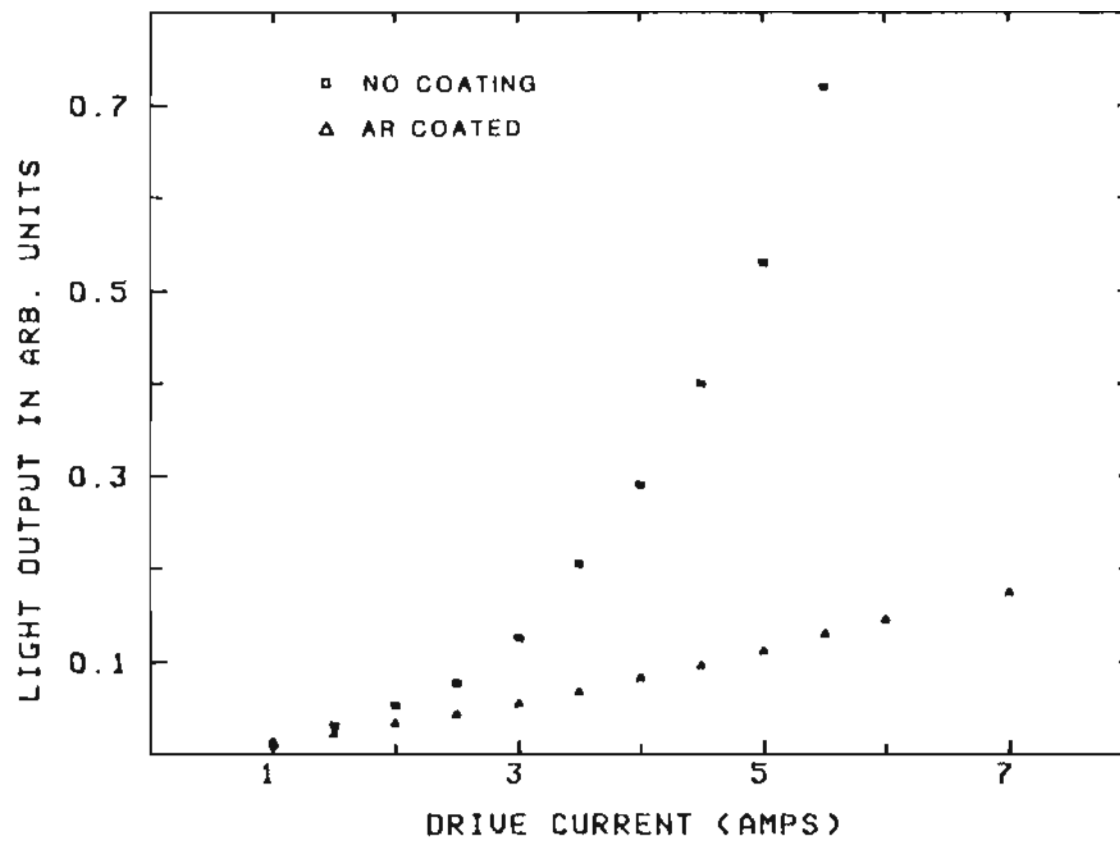


Figure 7.11 Optical output vs. drive current for an InGaAs/InP diode laser before and after coating with SiO<sub>2</sub>.

defect.

The cleaning and sputtering process was conducted as follows. After mounting of the diode lasers in their dual diode mount, the mount was ultrasonically washed in electronic grade acetone. After the washing was completed the mount was dried in a nitrogen jet. The mount was then placed in the evaporator and exposed for several minutes to Hg discharge- generated ozone to break down<sup>253</sup> any residual hydrocarbons from the acetone wash. Then the vacuum chamber was evacuated to a background pressure of 500 mtorr of argon and glow discharge sputtering<sup>254</sup> of the facet was achieved by placing the diode laser mount near the aluminum anode of a 2 mAmp/cm<sup>2</sup> current density discharge for several minutes. The discharge and subsequent film deposition were conducted in the presence of 200 mW of argon ion 514.5 nm laser light focussed on the facet. The laser light helped to keep the facet clean by heating it and by providing photons to the surface with energy greater than the binding energy of water vapor and hydrogen, the most common contaminants in high vacuum environments.

### 7.3 Electronic Construction

This section describes the electronic attributes of the dual diode laser cavity's wavelength controller and its current pulser. The wavelength controller was designed by this author and Mr. Robert Cary of Sunset Laboratory and OGC. The microprocessor coding was done by Mr. Cary. The electronic pulser was designed by Mr. John Hunt and constructed in the OGC electronics shop. Mr. Hunt is a Senior Electronics Engineer in the Applied Physics and Electrical Engineering Department at OGC. First, the wavelength controller will be described by paraphrasing and

summarizing its manual, "Dual Diode Cavity Wavelength Controller: Instrumentation for Automatic Laser Tuning". A definitive description of the controller, including hardware schematic diagrams and software code may be found in the manual. Second, the remaining part of the section will discuss the dual diode laser pulser.

The purpose of the wavelength controller is to cause automatic positioning of the grating angle relative to the external cavity so that maximum absorption in methane is achieved. The control process is designed to be a turn-key operation that is enabled whenever the diode laser electronics are turned on. Figure 7.12 is a block diagram of the physical layout of controller and its associated hardware. The hardware used in the controller consists of two circuits: the MotorMike (MM) motor control box and the analog signal board. Both of these connect to an Intel SBC 80/20 single-board computer.

The motor control box allows both forward and backward movement of the MM which positions the diffraction grating. It uses two of the TTL-compatible outputs from one 8255 Programmable Peripheral Interface (PPI) which is on board the 80/20. One output bit determines the motor direction while another bit turns the motor on and off.

The second circuit consists of analog signal conditioning amplifiers along with sample-and-hold (S/H) and analog-to-digital conversion (ADC) chips. This circuitry is constructed on a separate module which plugs onto one of the PPI edge connector ports. Two identical circuits are located on the module. The first circuit is for the reference optical signal and the second is dedicated to the signal from the optical power that has passed through a methane cell.

The signals are then conditioned. First, the reference and methane cell ger-



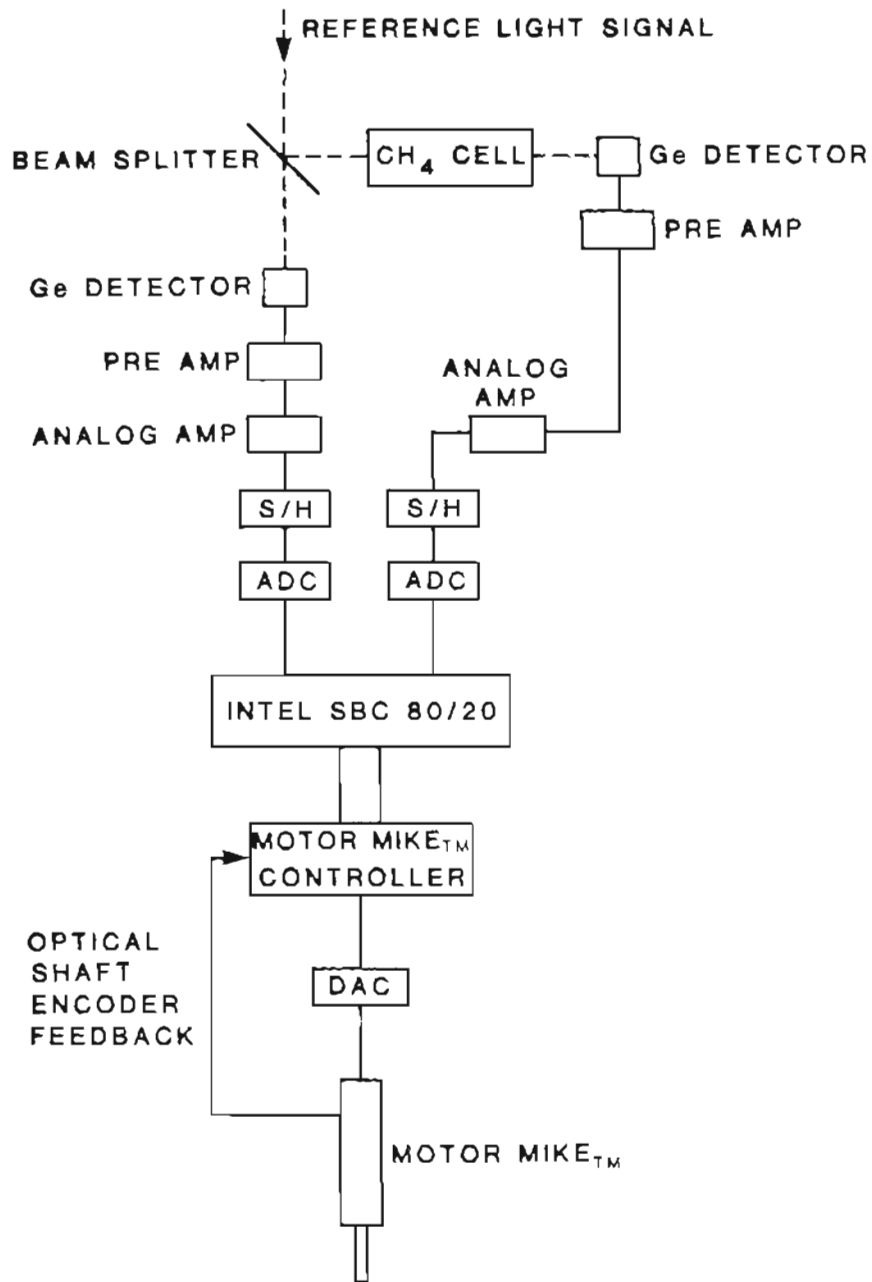


Figure 7.12 The wavelength controller and its associated hardware.

manium photodiode (Judson Infrared Model J-16) output is amplified using commercial preamps (Judson Infrared Model 700). The output from the preamps is then conditioned by a two-stage amplifier. The first stage is AC-coupled and noninverting with a gain of 12. This gain, coupled with that of the preamplifier, allows only a small portion of the optical output power to be used for this measurement. The next stage has a gain of 3 and includes an offset adjustable input. The offset allows the operator to calibrate a zero signal value while the light to the photodetectors is blocked.

The conditioned signals then go to sample-and-hold chips. These chips, as well as the following analog-to-digital converters, are controlled by the outputs from a dual monostable pulse generator which in turn is controlled by the TTL output of signal B from the diode laser pulser. The monostable pulse generator pulse widths are independently adjustable. This allows the operator to set the S/H-ADC operation to occur at the maximum for each photodetector pulse thus compensating for any difference in the time constants of the two channels. The rising edge of the pulse causes the S/H amplifiers to start sampling and sets up the ADCs. The falling edge of the pulse then causes the S/Hs to hold the peak value and simultaneously starts the conversions by the ADCs. The signal pulse from the optical detectors and their preamps and amplifiers occurs about 2 microseconds after the laser fires. After the ADC, the computer, which has been interrupted by the same TTL output B from the laser pulser, acquires the digital data.

The controlling software is written in assembly code and is stored in EPROMs. A complete listing of the software code is available in the controller manual. The code is located by functional blocks on separate EPROMs as follows. The first block contains power-up and interface chip initializations. The second block includes

several mathematical and setup routines called by the main operating system. The third EPROM includes several routines. One routine does 64 ADCs for each laser and then returns the ratio of the sums. Another scans the MM over a predetermined wavelength range seeking the minimum transmission through the methane cell. Other routines on this EPROM back up the MM to a predetermined point for rescanning of wavelength and output to a monitor raw signal values from each laser.

The main operating program contains the following functions:

1. Back up the MM 1024 counts (5.7 nm or  $21 \text{ cm}^{-1}$ ).
2. Scan forward 2048 counts (11.5 nm) moving the MM 3 or 4 counts ( $\approx 0.02 \text{ nm}$ ) each time saving the position where the minimum transmittance through the methane reference cell occurs.
3. Back up 128 counts beyond where the minimum was found.
4. Scan forward 256 counts, moving about 2 counts each time and again determine the location of minimum transmittance.
5. Compute a threshold value above the minimum value which will be looked for on the final scan. This has been implemented as 1/16 of the difference between the maximum and minimum ratios found during the first two scans but may be arbitrarily set.
6. Back up 64 counts beyond the most recently found minimum.
7. Scan forward, moving 1 count each time, until the threshold value is found.

The schematic diagrams for the dual diode current pulser are shown in Figures 7.13 and 7.14. Figure 7.13 shows the pulser timing circuitry. Figure 7.14 displays one channel of the current driver.

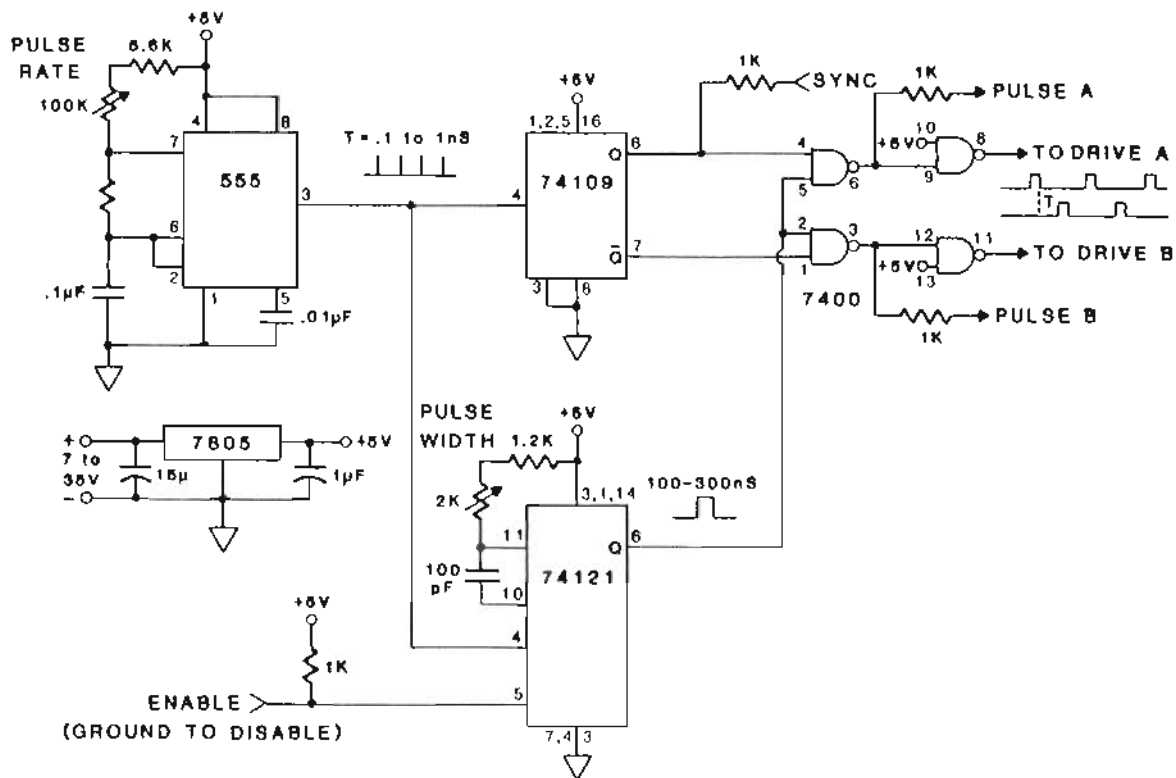


Figure 7.13 Timing circuitry for the dual diode laser pulser.

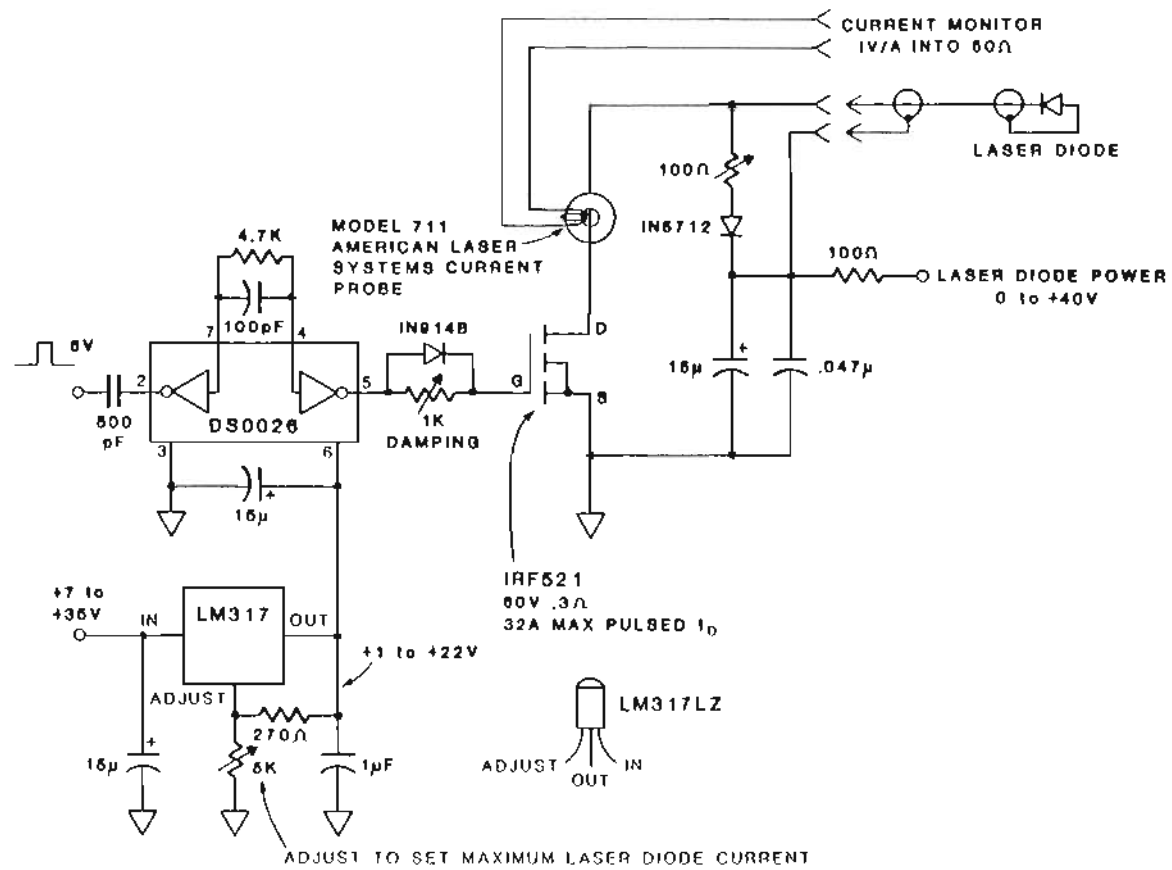


Figure 7.14 One current driver channel of the dual diode laser pulser.

The timing circuitry shown in Figure 7.13 has several notable features. The pulse repetition frequency may be set with the pulse rate potentiometer for inter-pulse periods of 0.1 to 1 ms. Another potentiometer controls the pulse width with a range of 100 to 300 ns available. An external enable (ground to disable) connector is provided to remotely turn the pulser on or off. Other external connection signals include a square wave synchronization signal at the PRF rate and TTL level pulse outputs, A and B, coincident in time with the laser current pulses. These three synchronization pulses allow for timing of external devices. Use of Pulse B was described above.

The diode driver shown in Figure 7.14 also has several notable features. The laser diode may be driven with a 0 to 10 Amp current pulse by varying the laser diode power voltage from 0 to  $\approx 40$  volts. This  $4 \Omega$  effective dynamic resistance compares favorably with the commercial diode laser pulsers, Laser Diode Labs (LDL) Model LPC-23C, used in the early parts of this study. The LDL pulser had an effective resistance of  $\approx 30 \Omega$  thus needing  $\approx 300$  volts to drive the a diode laser with 10 Amps. The improvement achieved is due to the use of low on-impedance FETs, IRF521, instead of SCRs as in the LDL devices. The rise time of the current pulse is approximately 15 ns when the diode laser is mounted at the pulser output and slightly longer when an external BNC cable connects to the laser. The driver has external connections that supply the current pulse waveforms using a single American Laser Systems Model 711 inductive current probe. Current to the dual diode laser mount is also supplied through external BNC connections.

## 7.4 Source Performance

This section presents the optical output characteristics of the dual diode laser source described in the last three sections. Specifically, the wavelength bandwidth and tunability are explained. The absorption of the optical output in methane is also discussed. Finally, automatic tuning of the diffraction grating to an absorption maximum in methane is demonstrated.

Figure 7.15 shows the tuning range accessible by the dual diode external cavity. The figure was generated by focussing the light output from one diode laser in the dual cavity onto the slit of a Jarell-Ash Mark-X 0.27 m spectrometer and scanning wavelength while synchronously detecting the spectrometer output with a Ge detector and lockin amplifier. It can be seen from the figure that a wavelength range of 1.624 to 1.648 ( $6158\text{-}6068\text{ cm}^{-1}$ ) was achieved in this instance. In other cases, both slightly shorter and longer wavelengths have been achieved. It may be seen that the spectral range of the figure includes several lines, notably R6, of the  $2\nu_3$  overtone band which was described in Chapter 3. However, not all wavelengths in this range were attainable.

Higher resolution spectral scans over a smaller region were in some instances conducted by placing a Fabry-Perot interferometer between the spectrometer output and the Ge detector. The interferometer consists of a piezoelectrically scanned Fabry-Perot device (Burleigh Model RC-110) driven by a dedicated ramp generator (Burleigh Model RC-42). The lockin amplifier output was then plotted on a chart recorder while holding the dual cavity grating fixed or the detector output was viewed on an oscilloscope screen while scanning the cavity grating. Figure 7.16 is an example of the chart recorder output. For this figure, the Fabry-Perot mirror

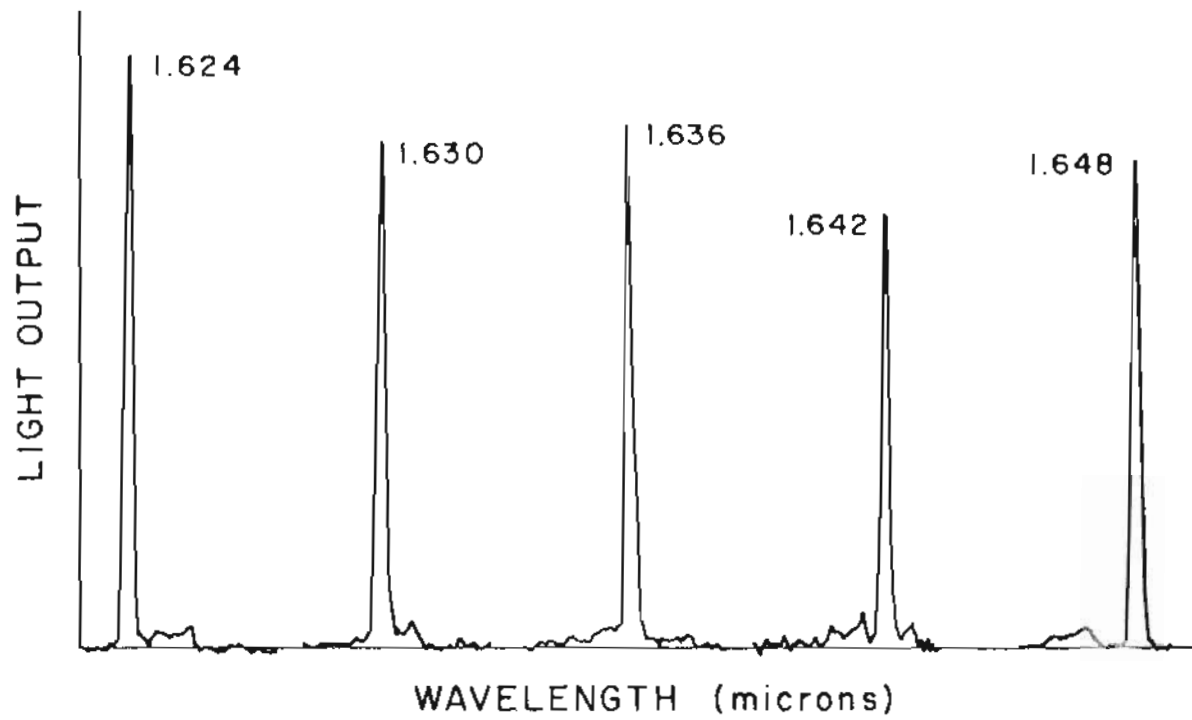


Figure 7.15 An example of the tuning range accessible by the dual diode external cavity.



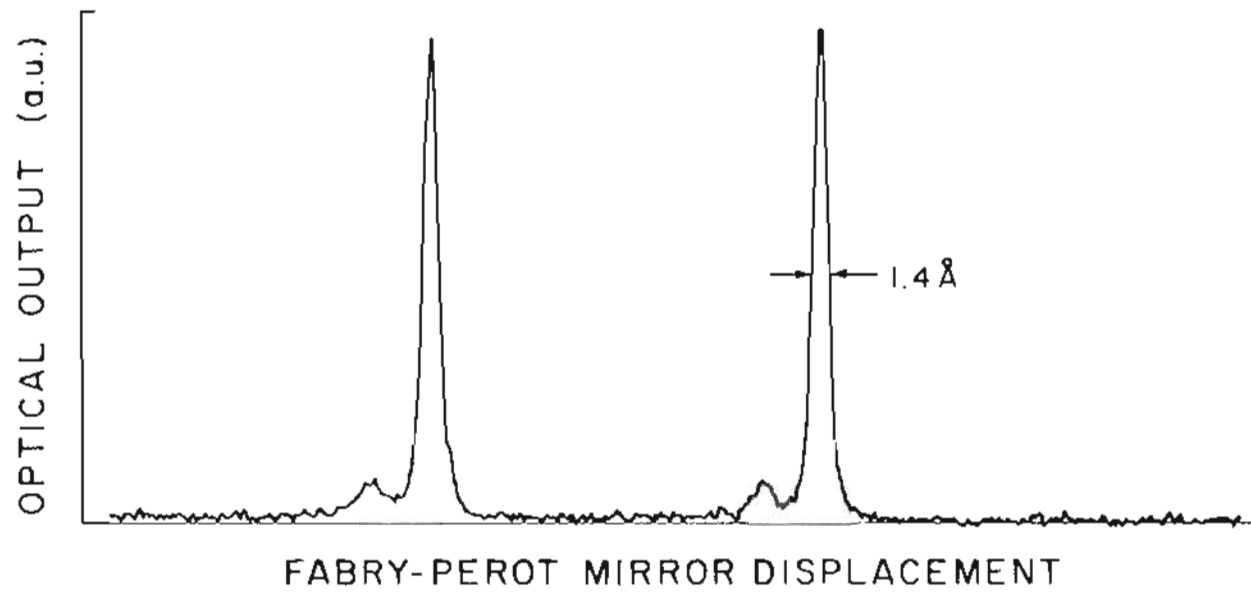


Figure 7.16 Optical output vs. Fabry-Perot mirror displacement for the dual diode external cavity.

separation was 0.013" yielding a interferometer free spectral range of 41 Angstroms. That is to say that the wavelength separation between the major peaks in the figure is 41 Angstroms. The slits of the spectrometer were adjusted to match this spectral range. From the figure, the calculated linewidth (FWHM) is 1.4 Angstroms. When the output was viewed on an oscilloscope and the grating was rotated, it was seen that for some positions of the grating the residual diode laser cavity modes, as determined by blocking the grating feed back while observing the spectrum, would appear. This was the cause of the inability mentioned above to achieve all wavelengths encompassed by the range of Figure 7.15. The source of such residual laser cavity modes is residual reflectivity which indicates that a more efficient AR coating would be required for more continuous tuning. It was also observed that tuning tended to be less efficient with usage over several days indicating possible degradation of the coatings.

Measurements of the optical absorption in a 30 cm methane cell were conducted. The cavity was tuned so that maximum absorption was attained for one diode while at the same time negligible absorption occurred for the other diode. The methane in the cell was at atmospheric pressure. The maximum absorption observed in the cell was slightly over 65%, which is equivalent to an absorption coefficient of  $0.04 \text{ cm}^{-1}\text{atm}^{-1}$ . In contrast, the maximum achievable absorption as shown in Figure 3.9 for a laser bandwidth of  $0.2 \text{ cm}^{-1}$  would be  $0.15\text{cm}^{-1}\text{atm}^{-1}$ . The increased spectral bandwidth described above is the cause of the decreased absorption.

To demonstrate the activity of the wavelength controller, the amount of absorption in the cell was also measured and recorded on magnetic tape by the wavelength controller described in Section 7.3 as it rotated the grating over a range

near maximum absorption seeking the minimum cell transmission. Figure 7.17 shows data for one wavelength search as stored on the tape. Although maximum absorption was not seen during this experiment because of inadequate cavity optical alignment, it can be seen in the figure that the dual diode laser output scans through a minimum in transmission and then retraces its steps through the minimum again. What is not shown in the figure is the final scan described in Section 7.3.

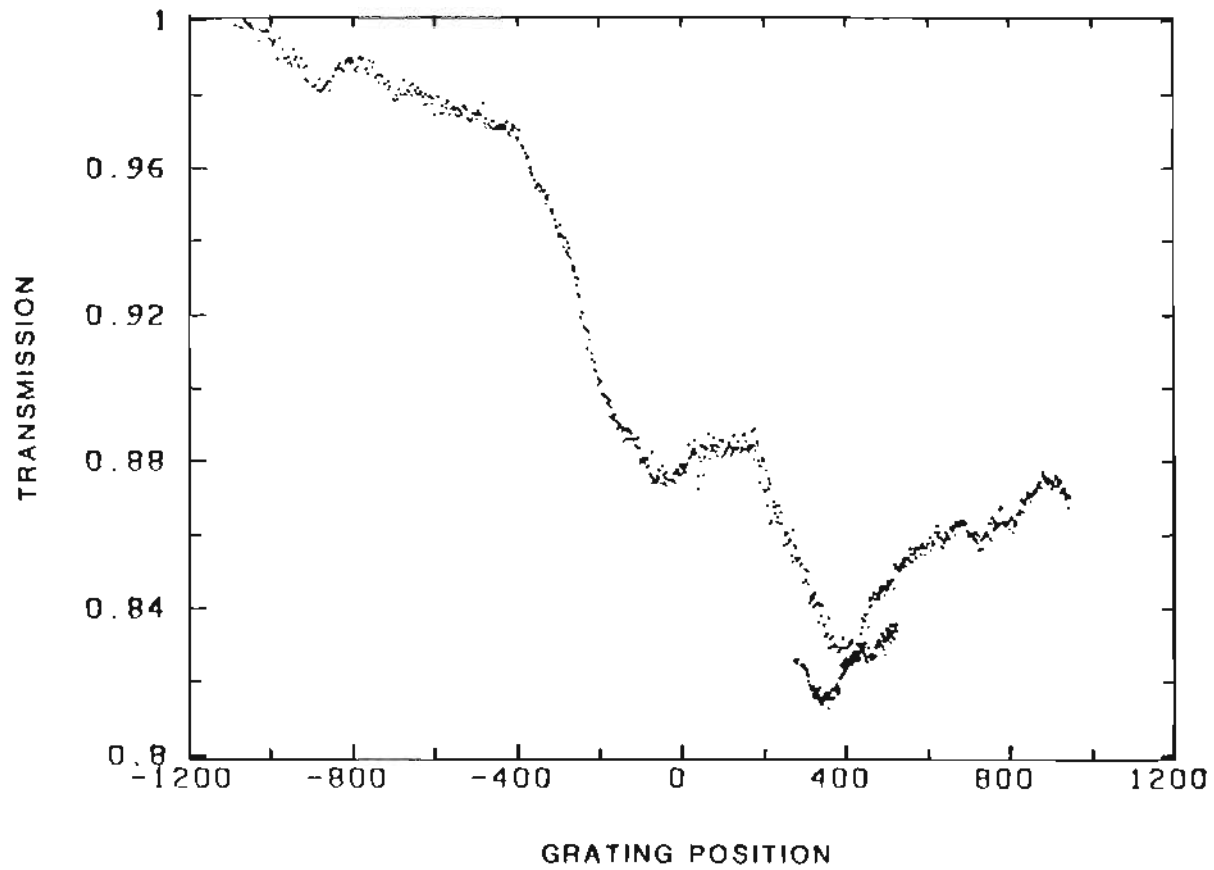


Figure 7.17 An example of the absorption as a function of wavelength measured by the dual diode laser cavity wavelength controller.

## 8. CONCLUSIONS

This research project has encompassed two tasks. The first was a study conducted to determine if room-temperature injection lasers could be used as the source for a DIAL methanometer for coal mine applications. As part of that study, prior DIAL measurements of methane were reviewed and the measurement technique was explored in a general way as reported in Chapter 2. Then, the absorption spectroscopy of methane was examined in detail and found to contain an appropriate absorption feature near a wavelength of  $1.65 \mu\text{m}$  when the spectral width of the light source was approximately  $0.2 \text{ cm}^{-1}$ . The spectroscopic studies are explained in Chapter 3. As an additional part of the study the operating characteristics of broad area high optical output InGaAs/InP injection lasers were examined. Chapter 4 reports on the operating characteristics found. A detailed calculation of the requirements for a diode laser DIAL measurement of methane in a coal mine was then carried out as presented in Chapter 5. By comparison of the diode laser properties reported in Chapter 4 with the DIAL requirements developed in Chapter 5, it was found that broad area InGaAs/InP injection lasers were suitable in most respects for coal methane measurements. The exception was the diode laser spectral bandwidth. It was found to be some 400 times too large.

The second task was the design and fabrication of an external grating cavity to reduce the bandwidth of the injection lasers described in Chapter 4. Chapter 6

develops the optical design of an off-axis parabolic mirror grating cavity. Using geometric optical design, the desired spectral bandwidth of  $0.2 \text{ cm}^{-1}$ , was used to determine the physical parameters for the external cavity. Chapter 7 describes the fabrication and performance of the external resonator source. The source was found to have a narrowed bandwidth two to three times larger than designed. An explanation of the resultant bandwidth based on coupled mode theory is presented in Chapter 7 and Appendix E. In summary, an external grating cavity for a diode laser was assembled which was able to approximate the optical properties required for a DIAL coal mine methane measurement.

Coupled cavity diode lasers may provide a convenient means to achieve the narrow spectral bandwidth and the high optical output necessary for remote sensing applications in coal mines. Cleaved-coupled-cavities ( $C^3$ ) have previously been used<sup>255-259</sup> to obtain frequency-stable, tunable, single-longitudinal mode operation in index-guided, single-emitter, InGaAsP diode lasers with optical outputs ranging from 0.5 to 2.5 mW. Recently, DeFreez et al. reported<sup>260</sup> CW operation of a  $C^3$  phase-locked array of gain-guided GaAlAs lasers. They obtained tunable, single-longitudinal mode operation to output powers as high as 50 mW as well as control of the radiation pattern emitted by the array. It is the opinion of the author that there are no fundamental physical obstacles to transferring this technology to the longer wavelength InGaAsP diode laser family. Thus, it would seem that small, efficient, safe sources for remote measurements of methane for coal mine, as well as other, applications can be available in the very near future.

## References

1. R. L. Marovelli and J. M. Karhnek, "The mechanization of mining," *Sci. Am.*, vol. 247, pp. 91-102, Sept. 1982.
2. *Federal Coal Mine Health and Safety Act of 1969.*
3. S. B. Eynon, "Leak detection-status & needs," *GRI Workshop*, Feb. 1983.
4. G. Schnakenberg, "Gas detection instrumentation... what's new and what's to come," *Coal Age*, pp. 84-92, Mar. 1975.
5. W. D. Egan, "General performance specifications for an instrument to remotely measure methane in a coal mine," Bethlehem Steel Corporation Homer Research Laboratories Internal Report, File #1006-3a, 15 May 1978.
6. *The Story of Coal*, Bethlehem Steel Corporation.
7. W. D. Egan, "Remote measurement of methane in coal mines," Report BX-41-78010 IR, Dec. 10 1979. Bethlehem Steel Corporation Homer Research Laboratories Internal Report, File #10066-3a
8. Letter from E. H. Kottkamp, Jr. to R. L. Whitely, Methane detection at the face in coal mines, May 23, 1977.
9. R. L. Byer, "Remote measurement of methane in a coal mine environment," Report from Stanford University Edward L. Ginzton Laboratory of Physics to Bethlehem Steel Corporation Homer Research Laboratories, Aug. 1978.
10. H. R. Wittman, "An Erbium laser target illuminator pumped by GaAs LEDs," *U.S. Army, Project No. 1T061102B23D*, 1970. MC Management Structure Code #501B.11.0310
11. "Electrical Equipment, Lamps, Methane Detectors; Tests for Permissibility; Fees," *Title 30, Sub-Chapter D, Part 18*, U.S. Dept. of Commerce, Mine and Safety Administration, July 1980.
12. M. A. Pollack, R. E. Nahory, J. C. DeWinter, and A. A. Ballman, "Liquid phase epitaxial  $\text{In}_{1-x}\text{Ga}_x\text{As}_y\text{P}_{1-y}$  lattice matched to  $\langle 100 \rangle$  InP over the complete wavelength range  $0.92 \leq \lambda \leq 1.65 \mu\text{m}$ ," *Appl. Phys. Lett.*, vol. 33, pp. 314-316, 15 Aug. 1978.
13. J. J. Hsieh, "Zn-diffused, stripe-geometry, double-heterostructure GaInAsP diode lasers," *IEEE J. Quantum Electron.*, vol. QE-15, pp. 694-697, Aug. 1979.
14. S. Arai, Y. Suematsu, and Y. Itaya, "1.11-1.67  $\mu\text{m}$  (100) GaInAsP/InP injection lasers prepared by liquid phase epitaxy," *IEEE J. Quantum Electron.*, vol. QE-16, pp. 197-205, Feb. 1980.
15. B. I. Miller, J. H. McFee, R. J. Martin, and P. K. Tien, "Room-temperature operation of lattice-matched  $\text{InP}/\text{Ga}_{0.47}\text{In}_{0.53}\text{As}/\text{InP}$ ," *Appl. Phys. Lett.*, vol. 33, pp. 44-47, 1 Jul. 1978.
16. G. H. Olsen, T. J. Zamerowski, and N. J. DiGiuseppe, "1.5-1.7  $\mu\text{m}$  V.P.E. InGaAsP/InP C.W. lasers," *Elect. Lett.*, vol. 16, pp. 516-517, 19 Jun. 1980.
17. W. T. Tsang, " $\text{Al}_{0.48}\text{In}_{0.52}\text{As}/\text{Ga}_{0.47}\text{In}_{0.53}\text{As}/\text{Al}_{0.48}\text{In}_{0.52}\text{As}$  double-heterostructure lasers grown by molecular-beam epitaxy with lasing wavelength at 1.65  $\mu\text{m}$ ," *J. Appl. Phys.*, vol. 52, pp. 3861-3865, Jun. 1981.

18. R. K. DeFreez, R. A. Elliott, J. S. Blakemore, B. J. Miller, J. H. McFee, and R. J. Martin, "High-output room-temperature pulsed operation for broad contact InP/In<sub>0.53</sub>Ga<sub>0.47</sub>As/InP lasers grown by molecular beam epitaxy," *J. Appl. Phys.*, vol. 54, pp. 2177-2182, May 1983.
19. J. S. Blakemore and R. K. DeFreez, "Methane detection research," , Oct. 1981. Report to Bethlehem Steel Corporation Homer Research Laboratories from Oregon Graduate Center
20. W. D. Egan. Homer Research Laboratories, Bethlehem Steel Corporation, Private Communications
21. H. Gerritsen, S. Renman, C. Taylor, E. Crisman, and J. Beall, "Use of room temperature diodes in monitoring specific gases in air, particularly methane and carbon monoxide," USBM Grant No. G0101740, Final Report, Brown University, Providence, R.I., Jul. 1974. NTIS: No. PB245912/As
22. P. L. Kebabian, *Gas detector*, 22 Nov. 1977. U.S. Patent No. 4,059,356
23. J. Carney, J. Abrokwah, R. Aagard, W. Walters, and U. Bonne, "An improved detector for natural gas," *GRI Workshop*, Feb. 1983.
24. G. Fiocco and L. D. Smullin, *Nature*, vol. 199, pp. 1275-1276, 1963.
25. H. Kildal and R. L. Byer, "Comparison of laser methods for the remote detection of atmospheric pollutants," *IEEE Proc.*, vol. 59, pp. 1644-1663, Dec. 1971.
26. R. L. Byer, "Review: remote air pollution measurement," *Opt. Quan. Electron.*, vol. 7, pp. 147-177, 1975.
27. K. Petri, A. Salik, and J. Cooney, "Variable-wavelength solar-blind raman lidar for remote measurement of atmospheric water-vapor concentration and temperature," *Appl. Opt.*, vol. 21, pp. 1212-1218, 1 Apr. 1982.
28. D. A. Leonard, "Remote raman measurement techniques," *Opt. Eng.*, vol. 20, pp. 91-94, Jan./Feb. 1981.
29. J. A. Cooney, "Uses of raman scattering for remote sensing of atmospheric properties of meteorological significance," *Opt. Eng.*, vol. 22, pp. 292-301, May/June 1983.
30. Letter from C. D. Litton, U.S.B.M., to R. Boos, HRL, 26 Jun. 1981.
31. W. D. Egan, "Technical concerns-bumines raman scattering technique for remote methane gas measurement," HRL File Memo, File 1006-3a, 10 July 1981.
32. R. L. Byer and M. Garbuny, "Pollutant detection by absorption using mie scattering and topographic targets as retroreflectors," *Appl. Opt.*, vol. 12, pp. 1496-1505, Jul. 1973.
33. M. J. Kavaya, R. T. Menzies, D. A. Haner, U. P. Oppenheim, and P. H. Flamant, "Target reflectance measurements for calibration of lidar atmospheric backscatter data," *Appl. Opt.*, vol. 22, pp. 2619-2628, 1 Sep. 1983.
34. W. B. Grant, "Effect of differential spectral reflectance on DIAL measurements using topographic targets," *Appl. Opt.*, vol. 21, pp. 2390-2394, 1 Jul. 1982.
35. R. M. Schotland, *Proc. 4th Symposium on Remote Sensing of the Environment*, Ann Arbor, Michigan, Apr. 1966.



36. B. Marthinsson, J. Johansson, and S. T. Eng, "Air pollution monitoring with a computer-controlled CO<sub>2</sub>-laser long-path absorption system," *Opt. Quan. Electron.*, vol. 12, pp. 327-334, 1980.
37. S. Lundqvist, C. Falt, U. Persson, B. Marthinsson, and S. T. Eng, "Air pollution monitoring with a Q-switched CO<sub>2</sub>-laser lidar using heterodyne detection," *Appl. Opt.*, vol. 20, pp. 2534-2538, 15 Jul. 1981.
38. N. Menyuk, D. K. Killinger, and W. E. DeFeo, "Laser remote sensing of hydrazine, MMH, and UDMH using a differential-absorption CO<sub>2</sub> LIDAR," *Appl. Opt.*, vol. 21, pp. 2275-2286, 15 Jun. 1982.
39. D. K. Killinger, N. Menyuk, and W. E. DeFeo, "Experimental comparison of heterodyne and direct detection for pulsed differential absorption CO<sub>2</sub> lidar," *Appl. Opt.*, vol. 22, pp. 682-689, 1 Mar. 1983.
40. T. Kobayasi, M. Hirama, and H. Inaba, "Remote monitoring of NO<sub>2</sub> molecules by differential absorption using optical fiber link," *Appl. Opt.*, vol. 20, pp. 3279-3280, 1 Oct. 1981.
41. M. Endemann and R. L. Byer, "Simultaneous remote measurements of atmospheric temperature and humidity using a continuously tunable IR lidar," *Appl. Opt.*, vol. 20, pp. 3211-3217, 15 Sep. 1981.
42. K. Fredriksson, B. Galle, K. Nystrom, and S. Svanberg, "Lidar system applied in atmospheric pollution monitoring," *Appl. Opt.*, vol. 18, pp. 2998-3003, 1 Sep. 1979.
43. K. Fredriksson, B. Galle, K. Nystrom, and S. Svanberg, "Mobile lidar system for environmental probing," *Appl. Opt.*, vol. 20, pp. 4181-4189, 15 Dec. 1981.
44. M. Alden, H. Edner, and S. Svanberg, "Laser monitoring of atmospheric NO using ultraviolet differential-absorption techniques," *Opt. Lett.*, vol. 7, pp. 543-545, Nov. 1982.
45. W. A. McClenny and G. M. Russwurm, "Laser-based long path monitoring of ambient gases- analysis of two systems," *Atmos. Envir.*, vol. 12, pp. 1443-1453, 1978.
46. J. Reid, J. Shewchun, B. K. Garside, and E. A. Ballik, "High sensitivity pollution detection employing tunable diode lasers," *Appl. Opt.*, vol. 17, pp. 300-307, 15 Jan. 1978.
47. D. T. Cassidy and J. Reid, "Atmospheric pressure monitoring of trace gases using tunable diode lasers," *Appl. Opt.*, vol. 21, pp. 1185-1190, 1 Apr. 1982.
48. C. R. Webster and W. B. Grant, "Laboratory simulation of tunable diode laser remote measurement of atmospheric gases using topographic targets," *Appl. Opt.*, vol. 22, pp. 1952-1954, 1 July 1983.
49. E. D. Hinkley, "Laser spectroscopic instrumentation and techniques: long-path monitoring by resonance absorption," *Opt. Quan. Electron.*, vol. 8, pp. 155-167, 1976.
50. W. B. Grant and R. T. Menzies, "A survey of laser and selected optical systems for remote measurement of pollutant gas concentrations," *J. Air Poll. Control Assoc.*, vol. 33, pp. 187-194, Mar. 1983.

51. M. A. K. Khalil and R. A. Rasmussen, "Sources, sinks, and seasonal cycles of atmospheric methane," *Jour. Geophys. Res.*, vol. 88, pp. 5131-5144, Jun. 1983.
52. B. N. Edwards and D. E. Burch, "Absorption of 3.39-micron helium-neon laser emission by methane in the atmosphere," *J. O. S. A.*, vol. 55, pp. 174-177, Feb. 1965.
53. K. O. White and S. A. Schleusener, "Coincidence of Er:YAG laser emission with methane absorption at 1645.1 nm," *Appl. Phys. Lett.*, vol. 21, pp. 419-420, 1 Nov. 1972.
54. E. R. Murray, J. E. van der Laan, and J. G. Hawley, "Remote measurement of HCl, CH<sub>4</sub>, and N<sub>2</sub>O using a single-ended chemical-laser lidar system," *Appl. Opt.*, vol. 15, pp. 3140-3148, Dec. 1976.
55. E. R. Murray, "Remote measurement of gases using discretely tunable infrared lasers," *Opt. Eng.*, vol. 16, pp. 284-290, May/June. 1977.
56. E. R. Murray, "Remote measurement of gases using differential-absorption LIDAR," *Opt. Eng.*, vol. 17, pp. 30-38, Jan./Feb. 1978.
57. R. A. Baumgartner and R. L. Byer, "Continuously tunable IR lidar with applications to remote measurements of SO<sub>2</sub> and CH<sub>4</sub>," *Appl. Opt.*, vol. 17, pp. 3555-3561, 15 Nov. 1978.
58. W. B. Grant and E. D. Hinkley, "Laser system for natural gas detection-phase I: laboratory feasibility studies," Report for Gas Research Institute, Jet Propulsion Lab., Pasadena, Calif., 21 Jul. 1982.
59. W. B. Grant, "Helium-Neon laser remote sensing of methane leaks," *GRI Workshop*, Feb. 1983.
60. W. B. Grant and C. R. Webster, "Measurement of gases using CW lasers, differential absorption, and topographic targets," *O. S. A. Winter Topical Meeting on Atmospheric Optics*, Jan. 1983.
61. A. Rosengreen and L. L. Altpeter, "Portable remote sensing system (DIAL) for leak detection of natural gases," *GRI Workshop*, Feb. 1983.
62. K. Chan, H. Ito, and H. Inaba, "Optical remote monitoring of CH<sub>4</sub> gas using low-loss optical fiber link and InGaAsP light-emitting diode in 1.33- $\mu$ m region," *Appl. Phys. Lett.*, vol. 43, pp. 634-636, 1 Oct. 1983.
63. K. O. White and W. R. Watkins, "Erbium laser as a remote sensor of methane," *Appl. Opt.*, vol. 14, pp. 2812-2813, Dec. 1975.
64. W. R. Watkins and K. O. White, "Wedge absorption remote sensor," *Rev. Sci. Instrum.*, vol. 52, pp. 1682-1684, Nov. 1981.
65. W. D. Egan, R. T. Boos, R. K. DeFreez, and R. L. Byer, "Remote differential absorption and scattering measurement of methane near a coal mine working face," *Technical Digest of the Conference on Lasers and Electro-Optics*, Baltimore, MD, May 1983. Paper ThK3
66. W. D. Egan, R. Boos, R. K. DeFreez, and R. L. Byer, *Remote Measurement of Concentration of a Gas Specie by Resonance Absorption*, 7 Dec. 1982. U.S. Patent # 4,362,388
67. R. K. DeFreez, "Remote DIAL Measurements of Methane in Coal Mines," *Technical Digest of the Optical Society of America Topical Meeting on Optical*

- Remote Sensing of the Atmosphere*, Incline Village, January, 1985. Invited Paper ThB2
68. R. K. DeFreez and R. A. Elliott, "Laser diode source for methane detection in coal gas," *Technical Digest of the Conference on Lasers and Electro-Optics*, Baltimore, MD, May 1983. Paper ThK2
  69. R. K. DeFreez and R. A. Elliott, "External grating-tuned dual-diode-laser source for remote detection of coal gas methane," (*A*) *J. O. S. A.*, vol. 73, p. 1854, Dec. 1983.
  70. G. H. B. Thompson, *Physics of Semiconductor Laser Devices*, John Wiley & Sons, New York, N.Y., 1980.
  71. R. A. McClatchey, W. S. Benedict, S. A. Clough, D. E. Burch, R. F. Calfee, K. Fox, L. S. Rothman, and J. S. Garing, *AFCRL Atmospheric Absorption Line Parameters Compilation*, Air Force Cambridge Research Laboratories, Bedford, Mass., 1973.
  72. R. S. Eng, J. F. Butler, and K. J. Linden, "Tunable diode laser spectroscopy: an invited review," *Opt. Eng.*, vol. 19, pp. 945-960, Nov./Dec. 1980.
  73. K. Fox, G. W. Halsey, and D. E. Jennings, "High resolution spectrum and analysis of  $2\nu_3$  of  $^{13}\text{CH}_4$  at  $1.67 \mu\text{m}$ ," *J. Mol. Spectrosc.*, vol. 83, pp. 213-222, 1980.
  74. L. S. Rothman, R. R. Gamache, A. Barbe, A. Goldman, J. R. Gillis, L. R. Brown, R. A. Toth, J.-M. Flaud, and C. Camy-Peyret, "AFGL atmospheric absorption line parameters compilation. 1982 edition," *Appl. Opt.*, vol. 22, pp. 2247-2256, 1 Aug. 1983.
  75. L. S. Rothman, "AFGL atmospheric absorption line parameters compilation: 1980 version," *Appl. Opt.*, vol. 20, pp. 791-795, 1 Mar. 1981.
  76. G. Herzberg, *Molecular Spectra and Molecular Structure: II. Infrared and Raman Spectra of Polyatomic Molecules*, D. Van Nostrand Co., Inc., Princeton, N.J., 1968.
  77. K. Chan, H. Ito, and H. Inaba, "Absorption measurement of  $\nu_2+2\nu_3$  Band of  $\text{CH}_4$  at  $1.33 \mu\text{m}$  using an InGaAsP light emitting diode," *Appl. Opt.*, vol. 22, pp. 3802-3804, 1 Dec. 1983.
  78. W. V. Norris and H. J. Unger, "Infrared absorption bands of methane," *Phys. Rev.*, vol. 43, pp. 467-472, 15 Mar. 1933.
  79. K. Chan, H. Ito, and H. Inaba, "Remote sensing system for near-infrared differential absorption of  $\text{CH}_4$  gas using low-loss optical fiber link," *Appl. Opt.*, vol. 23, pp. 3415-3420, 1 Oct. 1984.
  80. K. Fox, "High-resolution spectra of isotopic methanes near  $1645\text{nm}$ ," *Appl. Opt.*, vol. 23, pp. 3040-3042, 15 Sep. 1984.
  81. K. Fox, "Coincidence of Er:YAG laser emission with methane absorption at  $6077 \text{cm}^{-1}$ ," *Appl. Phys. Lett.*, vol. 24, pp. 24-26, 1 Jan. 1974.
  82. Optical Society of America, *Handbook of Optics*, McGraw-Hill, 1978.
  83. *Handbook of Physics and Chemistry*, CRC Press, 1980-1981. 51st ed.

84. E. J. McCartney, *Absorption and Emission by Atmospheric Gases: The Physical Processes*, John Wiley and Sons, New York, N.Y., 1983.
85. A. G. Kim, *The composition of coalbed gas*, U. S. Bureau of Mines, 1973. Report of Investigations 7762
86. N. Kobayashi and Y. Horikoshi, "Liquid phase epitaxial growth of  $\text{InAs}_{1-x-y}\text{P}_x\text{Sb}_y$  on an InAs Substrate," *Jpn. Jnl. Appl. Phys.*, vol. 20, pp. 2301-2305, Dec. 1981.
87. L. M. Dolginov, A. E. Drakin, L. V. Druzhinina, P. G. Eliseev, M. G. Milvidsky, V. A. Skripkin, and B. N. Sverdlov, "Low threshold heterojunction AlGaAsSb/GaSb lasers in the wavelength range of 1.5-1.8  $\mu\text{m}$ ," *IEEE J. Quantum Electron.*, vol. QE-17, pp. 593-597, May 1981.
88. N. Kobayashi, Y. Horikoshi, and C. Uemura, "Room temperature operation of the InGaAsSb/AlGaAsSb DH laser at 1.8  $\mu\text{m}$  wavelength," *Jpn. J. Appl. Phys.*, vol. 19, pp. L30-L32, Jan. 1980.
89. B. Bobin, "Interpretation de la bande harmonique  $2\nu_3$  du methane  $^{12}\text{CH}_4$  (De 5,890 A 6,107  $\text{cm}^{-1}$ )," *J. Physique*, vol. 33, pp. 345-352, Apr. 1972.
90. R. L. Byer, "Erbium doped YAG laser measurement results," Report from Edward L. Ginzton Laboratory of Physics to Homer Research Labs, May 1979.
91. D. J. Brassington, R. C. Felton, B. W. Jolliffe, B. R. Marx, J. T. M. Moncrieff, W. R. C. Rowley, and P. T. Woods, "Errors in spectroscopic measurements of  $\text{SO}_2$  due to nonexponential absorption of laser radiation, with application to the remote monitoring of atmospheric pollutants," *Appl. Opt.*, vol. 23, pp. 469-475, 1 Feb. 1984.
92. D. E. Burch and D. Williams, "Total absorptance of carbon monoxide and methane in the infrared," *Appl. Opt.*, vol. 1, pp. 587-594, Sep. 1962.
93. D. E. Burch, E. B. Singleton, and D. Williams, "Absorption line broadening in the infrared," *Appl. Opt.*, vol. 1, pp. 359-363, May 1962.
94. A. Anderson, An-Ti Chai, and D. Williams, "Self-broadening effects in the infrared bands of gases," *J. O. S. A.*, vol. 57, pp. 240-246, Feb. 1967.
95. R. L. Moon, G. A. Antypas, and L. W. James, "Bandgap and lattice constant of GaInAsP as a function of alloy composition," *J. Electron. Mater.*, vol. 3, pp. 635-645, 1974.
96. J. J. Hsieh, "Room-temperature operation of GaInAsP/InP double-heterostructure diode lasers emitting at 1.1  $\mu\text{m}$ ," *Appl. Phys. Lett.*, vol. 28, pp. 283-285, 1 Mar. 1976.
97. G. H. Olsen, "InGaAsP laser diodes," *Opt. Eng.*, vol. 20, pp. 440-445, May/June 1981.
98. M. Ettenberg and G. H. Olsen, "Diode lasers for the 1.2 to 1.7 micrometer region," *Las. Foc.*, pp. 61-66, Mar. 1982.
99. "Opto-coupled integrated transistors," *Electro-Optics*, Aug. 1983.
100. K. J. Bachmann and J. L. Shay, "An InGaAs detector for the 1.0-1.7- $\mu\text{m}$  wavelength range," *Appl. Phys. Lett.*, vol. 32, pp. 446-448, 1 Apr. 1978.

101. C. E. Hurwitz, "Detectors for the 1.1 to 1.6  $\mu\text{m}$  wavelength region," *Opt. Eng.*, vol. 20, pp. 658-664, Jul./Aug. 1981.
102. T. P. Pearsall, M. Piskorski, A. Brochet, and J. Chevrier, "A  $\text{Ga}_{0.47}\text{In}_{0.53}\text{As}/\text{InP}$  heterophotodiode with reduced dark current," *IEEE J. Quantum Electron.*, vol. QE-17, pp. 255-259, Feb. 1981.
103. T. Izawa, N. Shibata, and A. Takeda, "Optical attenuation in pure and doped fused silica in the IR wavelength region," *Appl. Phys. Lett.*, vol. 31, pp. 33-35, 1 Jul. 1977.
104. J. C. Gammel, H. Ohno, and J. M. Ballantyne. "High-speed photoconductive detectors using GaInAs," *IEEE J. Quantum Electron.*, vol. QE-17, pp. 269-272, Feb. 1981.
105. T. P. Pearsall and M. Papuchon, "The  $\text{Ga}_{0.47}\text{In}_{0.53}\text{As}$  homojunction photodiode - a new avalanche photodetector in the near infrared between 1.0 and 1.6  $\mu\text{m}$ ," *Appl. Phys. Lett.*, vol. 33, pp. 640-642, 1 Oct. 1978.
106. T. P. Pearsall, " $\text{Ga}_{0.47}\text{In}_{0.53}\text{As}$ : a ternary semiconductor for photodetector applications," *IEEE J. Quantum Electron.*, vol. QE-16, pp. 709-719, Jul. 1980.
107. A. W. Mabbitt, "Detectors for eye-safe laser range finders," *Electro-Optics*, pp. 30-32, Aug. 1983.
108. J. Shah, R. E. Nahory, R. F. Leheny, J. Degani, and A. E. DiGiovanni, "Hot-carrier relaxation in p- $\text{In}_{0.53}\text{Ga}_{0.47}\text{As}$ ," *Appl. Phys. Lett.*, vol. 40, pp. 505-507, 15 Mar. 1982.
109. D. R. Scifres, R. D. Burnham, C. Lindstrom, W. Streifer, and T. L. Paoli. "Phase-locked (GaAl)As laser emitting 1.5 W CW per mirror," *Appl. Phys. Lett.*, vol. 42, pp. 645-647, 15 Apr. 1983.
110. D. R. Scifres, C. Lindstrom, R. D. Burnham, W. Streifer, and T. L. Paoli, "Phase-locked (GaAl)As laser diode emitting 2.6 W CW from a single mirror," *Electron. Lett.*, vol. 19, pp. 169-171, 3 Mar. 1983.
111. T. R. Chen, K. L. Yu, B. Chang, A. Hasson, S. Margalit, and A. Yariv, "Phase-locked InGaAsP laser array with diffraction coupling," *Appl. Phys. Lett.*, vol. 43, pp. 136-137, 15 Jul. 1983.
112. B. I. Miller and J. H. McFee, "Growth of  $\text{Ga}_y\text{In}_{1-y}\text{As}/\text{InP}$  heterostructures by molecular beam epitaxy," *J. Electrochem. Soc.*, vol. 125, pp. 1310-1317, Aug. 1978.
113. H. C. Casey and M. B. Panish, *Heterostructure Lasers: Part A: Fundamental Principles*, Academic Press, New York, N.Y., 1978.
114. D. Botez, "Effective refractive index and first-order-mode cutoff conditions in InGaAsP/InP DH laser structures ( $\lambda = 1.2-1.6 \mu\text{m}$ )," *IEEE J. Quantum Electron.*, vol. QE-18, pp. 865-870, May 1982.
115. D. Botez, "Near and far-field analytical approximations for the fundamental mode in symmetric waveguide DH lasers," *RCA Rev.*, vol. 39, pp. 577-603, Dec. 1978.
116. D. Marcuse, *Theory of Dielectric Optical Waveguides*, Academic Press, New York, 1974.

117. H. Kressel and J. K. Butler, *Semiconductor Lasers and Heterojunction LEDs*, Academic Press, London, 1977.
118. D. Botez, "InGaAsP/InP double-heterostructure lasers: simple expressions for wave confinement, beamwidth, and threshold current over wide ranges in wavelength (1.1-1.65  $\mu\text{m}$ )," *IEEE J. Quantum Electron.*, vol. QE-17, pp. 178-186, Feb. 1981.
119. J. Buus, "Analytical approximation for the reflectivity of DH lasers," *IEEE J. Quantum Electron.*, vol. QE-17, pp. 2256-2257, Dec. 1981.
120. H. C. Casey and M. B. Panish, *Heterostructure Lasers: Part B: Materials and Operating Characteristics*, Academic Press, New York, N.Y., 1978.
121. T. Ikegami, "Reflectivity of mode at facet and oscillation mode in double-heterostructure injection lasers," *IEEE J. Quantum Electron.*, vol. QE-8, pp. 470-476, Jun. 1972.
122. M. A. A. Pudensi and L. G. Ferreira, "Method to calculate the reflection and transmission of guided waves," *J. O. S. A.*, vol. 72, pp. 126-130, Jan. 1982.
123. J. K. Butler and H. Kressel, "Design curves for double-heterojunction laser diodes," *RCA Rev.*, vol. 38, pp. 543-558, Dec. 1977.
124. H. C. Casey, M. B. Panish, and J. L. Merz, "Beam divergence of the emission from double-heterostructure injection lasers," *J. Appl. Phys.*, vol. 44, pp. 5470-5475, Dec. 1973.
125. L. Lewin, "Obliquity-factor correction to solid-state radiation patterns," *J. Appl. Phys.*, vol. 46, pp. 2323-2324, May 1975.
126. D. Botez and M. Ettenberg, "Beamwidth approximations for the fundamental mode in symmetric double-heterojunction lasers," *IEEE J. Quantum Electron.*, vol. QE-14, pp. 827-830, Nov. 1978.
127. N. K. Dutta and R. J. Nelson, "Temperature dependence of threshold of InGaAsP/InP double-heterostructure lasers and auger recombination," *Appl. Phys. Lett.*, vol. 38, pp. 407-409, 15 Mar. 1981.
128. A. Mozer, K. M. Romanek, W. Schmid, and M. H. Pilkuhn, "Evidence for auger and free-carrier losses in GaInAsP/InP lasers: spectroscopy of a short wavelength emission," *Appl. Phys. Lett.*, vol. 41, pp. 964-966, 15 Nov. 1982.
129. L. C. Chiu, P. C. Chen, and A. Yariv, "Interband auger recombination in InGaAsP," *IEEE J. Quantum Electron.*, vol. QE-18, pp. 938-941, Jun. 1982.
130. R. J. Nelson and N. K. Dutta, J. E. Swain, W. H. Lowdermilk, and D. Milam, "Raising damage thresholds of gradient-index antireflecting surfaces by pulsed laser irradiation," *Appl. Phys. Lett.*, vol. 41, pp. 782-783, 1 Nov. 1982.
131. A. Haug, "Auger recombination in InGaAsP," *Appl. Phys. Lett.*, vol. 42, pp. 512-514, 15 Mar. 1983.
132. T. Uji, K. Iwamoto, and R. Lang, "Nonradiative recombination in InGaAsP/InP light sources causing light emitting diode output saturation and strong laser-threshold-current-temperature sensitivity," *Appl. Phys. Lett.*, vol. 38, pp. 193-195, 15 Feb. 1981.
133. L. C. Chiu, K. L. Yu, S. Margalit, T. R. Chen, U. Koren, A. Hasson, and A. Yariv, "Field and hot carrier enhanced leakage in InGaAsP/InP

- heterojunctions," *IEEE J. Quantum Electron.*, vol. QE-19, pp. 1335-1338, Sep. 1983.
134. A. R. Adams, . Asada, Y. Suematsu, and S. Arai, "The temperature dependence of the efficiency and threshold current of  $\text{In}_{1-x}\text{Ga}_x\text{As}_y\text{P}_{1-y}$  lasers related to intervalence band absorption," *Japan. Jnl. Appl. Phys.*, vol. 19, pp. L621-L624, Oct. 1980.
  135. H. Higuchi, H. Namizaki, E. Oomura, R. Hirano, Y. Sakakibara, W. Susaki, and K. Fujikawa, "Internal loss of InGaAsP/InP buried crescent ( $\lambda=1.3\mu\text{m}$ ) laser," *Appl. Phys. Lett.*, vol. 41, pp. 320-321, 15 Aug. 1982.
  136. N. Tamari, M. Oron, B. I. Miller, A. A. Ballman, R. E. Nahory, R. J. Martin, H. Shtrikman, and L. A. Coldren, "High quantum efficiency InGaAsP/InP lasers," *Appl. Phys. Lett.*, vol. 41, pp. 1025-1027, 1 Dec. 1982.
  137. T. Yamamoto, K. Sakai, and S. Akiba, "10,000-h continuous CW operation of  $\text{In}_{1-x}\text{Ga}_x\text{As}_y\text{P}_{1-y}$ /InP DH lasers at room temperature," *IEEE J. Quantum Electron.*, vol. QE-15, pp. 684-687, Aug. 1979.
  138. K. Wakita, H. Takaoka, M. Seki, and M. Fukuda, "Transmission electron microscope observation of dark defects appearing in InGaAsP/InP double heterostructure lasers aged at accelerated operation," *Appl. Phys. Lett.*, vol. 40, pp. 525-527, 15 Mar. 1982.
  139. M. Fukuda, K. Takahei, G. Iwane, and T. Ikegami, "Facet degradation and passivation of InGaAsP/InP lasers," *Appl. Phys. Lett.*, vol. 41, pp. 18-21, 1 Jul. 1982.
  140. M. Morimoto, H. Imai, K. Hori, M. Takusagawa, and M. Fukuda, "Facet degradation of InGaAsP/InP double-heterostructure lasers," *Appl. Phys. Lett.*, vol. 37, pp. 1082-1084, 15 Dec. 1980.
  141. H. Temkin, S. Mahajan, M. A. DiGiuseppe, and A. G. Dentai, "Optically induced catastrophic degradation in InGaAsP/InP layers," *Appl. Phys. Lett.*, vol. 40, pp. 562-565, 1 Apr. 1982.
  142. J. E. A. Whiteaway and G. H. B. Thompson, "Optimisation of power efficiency of (GaAl)As injection lasers operating at high power levels," *Solid State & Electron Dev.*, vol. 1, pp. 81-88, Apr. 1977.
  143. R. Ito, M. Suyama, and N. Ogasawara, "Transient frequency and temperature variation of GaInPAs lasers under pulsed excitation," *Appl. Phys. Lett.*, vol. 40, pp. 214-216, 1 Feb. 1982.
  144. "Portable Methane Detectors," *Title 30, Sub-Chapter D, Part 22*. U.S. Dept. of Commerce, Mine and Safety Administration, July 1980.
  145. *American National Standard for the Safe Use of Lasers*, American National Standards Institute, Inc., New York, N.Y., 1980.
  146. *Title 21, Chapter 21, Subchapter J: Radiological Health*, 40 No. 148, pp. 32252-32266, Federal Register, 31 Jul. 1975.
  147. R. K. DeFreez,  $\text{CH}_4$  Laboratory Notebook, Homer Research Laboratories, Bethlehem Steel Corporation, 1979.
  148. A. Yariv, *Introduction to Optical Electronics*, Holt, Rinehart and Winston, New York, N.Y., 1976.

149. R. H. Hamstra and P. Wendland, "Noise and frequency response of silicon photodiode operational amplifier combination," *Appl. Opt.*, vol. 11, pp. 1539-1547, Jul. 1972.
150. *Germanium photodiode application note #501*, Judson Infrared Inc., 1981.
151. D. N. Payne and W. A. Gambling, "Zero dispersion in optical fibers," *Elect. Lett.*, vol. 11, pp. 176-178, 1975.
152. H. Ando, H. Kanbe, T. Kimura, T. Yamaoka, and T. Kaneda, "Characteristics of germanium avalanche photodiodes in the wavelength region of 1-1.6  $\mu\text{m}$ ," *IEEE J. Quantum Electron.*, vol. QE-14, pp. 804-809, Nov. 1978.
153. T. Mikawa, S. Kagawa, T. Kaneda, T. Sakurai, H. Ando, and O. Mikami, "A low-noise  $n^+np$  germanium avalanche photodiode," *IEEE J. Quantum Electron.*, vol. QE-17, pp. 210-216, Feb. 1981.
154. R. F. Leheny, R. E. Nahory, and M. A. Pollack, " $\text{In}_{0.53}\text{Ga}_{0.47}\text{As}$  p-i-n photodiodes for long-wavelength fibre-optic systems," *Elect. Lett.*, vol. 15, pp. 713-715, 25 Oct. 1979.
155. T. P. Lee, C. A. Burrus, A. Y. Cho, K. Y. Cheng, and D. D. Manchon, "Zn-diffused back-illuminated p-i-n photodiodes in InGaAs/InP grown by molecular beam epitaxy," *Appl. Phys. Lett.*, vol. 37, pp. 730-731, 15 Oct. 1980.
156. J. C. Campbell, A. G. Dentai, C. A. Burrus, and J. F. Ferguson, "InP/InGaAs heterojunction phototransistors," *IEEE J. Quantum Electron.*, vol. QE-17, pp. 264-269, Feb. 1981.
157. V. Diadiuk, S. H. Groves, C. E. Hurwitz, and G. W. Iseler, "Low dark-current, high gain GaInAs/InP avalanche photodetectors," *IEEE J. Quantum Electron.*, vol. QE-17, pp. 260-264, Feb. 1981.
158. T. P. Lee, C. A. Burrus, and A. G. Dentai, "InGaAs/InP p-i-n photodiodes for lightwave communications at the 0.95-1.65  $\mu\text{m}$  wavelength," *IEEE J. Quantum Electron.*, vol. QE-17, pp. 232-238, Feb. 1981.
159. K. Kasahara, J. Hayashi, K. Makita, K. Taguchi, A. Suzuki, H. Nomura, and S. Matuhita, "Monolithically integrated  $\text{In}_{0.53}\text{Ga}_{0.47}\text{As}$  -pin/InP-misfet photoreceiver," *Electron. Lett.*, vol. 20, pp. 314-315, 12 Apr. 1984.
160. C. Y. Chen, B. L. Kasper, and H. M. Cox, "High-sensitivity  $\text{Ga}_{0.47}\text{In}_{0.53}\text{As}$  photoconductive detectors prepared by vapor phase epitaxy," *Appl. Phys. Lett.*, vol. 44, pp. 1142-1144, 15 Jun. 1984.
161. *Technical data sheet for detector model QD*, Lasertron Corporation, Burlington, MA.
162. M. H. DeGroot, *Probability and Statistics*, Addison-Wesley, 1975.
163. G. K. Klauminzer, "The basics of boxcars," *Laser Focus*, 1981.
164. K. Neelakantan and S. Dattagupta, "Analysis of signal-to-noise enhancement of box-car averagers," *Pramana*, vol. 11, pp. 295-306, Sep. 1978.
165. A. G. Kjelaas, P. E. Nordal, and A. Bjerkestrand, "Scintillation and multiwavelength coherence effects in a long-path laser absorption spectrometer," *Appl. Opt.*, vol. 17, pp. 277-284, 15 Jan. 1978.



166. N. Menyuk and D. K. Killinger, "Temporal correlation measurements of pulsed dual CO<sub>2</sub> Lidar returns," *Opt. Lett.*, vol. 6, pp. 301-303, Jun. 1981.
167. J. C. Petheram, "Differential backscatter from the atmospheric aerosol: the implications for IR differential absorption lidar," *Appl. Opt.*, vol. 20, pp. 3941-3946, 15 Nov. 1981.
168. J. L. Bufton, T. Itabe, and D. A. Grolemond, "Dual-wavelength correlation measurements with an airborne pulsed carbon dioxide lidar system," *Opt. Lett.*, vol. 7, pp. 584-586, Dec. 1982.
169. S. F. Clifford and L. Lading, "Monostatic diffraction-limited LIDARs: the impact of optical refractive turbulence," *Appl. Opt.*, vol. 22, pp. 1696-1701, 1 Jun. 1983.
170. D. K. Killinger and N. Menyuk, "Effect of turbulence-induced correlation on laser remote sensing errors," *Appl. Phys. Lett.*, vol. 38, pp. 968-970, 15 Jun. 1981.
171. D. K. Killinger and N. Menyuk, "Remote probing of the atmosphere using a CO<sub>2</sub> DIAL system," *IEEE J. Quantum Electron.*, vol. QE-17, pp. 1917-1929, Sep. 1981.
172. N. Menyuk, D. K. Killinger, and C. R. Menyuk, "Limitations of signal averaging due to temporal correlation in laser remote-sensing measurements," *Appl. Opt.*, vol. 21, pp. 3377-3383, 15 Sep. 1982.
173. N. Menyuk and D. K. Killinger, "Assessment of relative error sources in IR DIAL measurement accuracy," *Appl. Opt.*, vol. 22, pp. 2690-2698, 1 Sep. 1983.
174. R. C. Harney, "Laser prf considerations in differential absorption lidar applications," *Appl. Opt.*, vol. 22, pp. 3747-3750, 1 Dec. 1983.
175. P. A. Pineus, R. A. Elliott, and J. R. Kerr, "Conditional fading statistics of scintillation," *J. O. S. A.*, vol. 68, pp. 756-760, Jun. 1978.
176. N. Menyuk, D. K. Killinger, and C. R. Menyuk, "Error reduction in laser remote sensing: combined effects of cross correlation and signal averaging," *Appl. Opt.*, vol. 24, pp. 118-131, 1 Jan. 1985.
177. L. A. Glasser, "C. W. modelocking of a GaInAsP diode laser," *Elect. Lett.*, vol. 14, pp. 725-726, 9 Nov. 1978.
178. P. T. Ho, L. A. Glasser, E. P. Ippen, and H. A. Haus, "Picosecond pulse generation with a CW GaAlAs laser diode," *Appl. Phys. Lett.*, vol. 33, pp. 241-242, 1 Aug. 1978.
179. P. T. Ho, "Coherent pulse generation with a GaAlAs laser by active modelocking," *Elect. Lett.*, vol. 15, pp. 526-527, 16 Aug. 1979.
180. H. Ito, H. Yokoyama, and H. Inaba, "Bandwidth limited picosecond optical pulse generation from actively mode-locked AlGaAs diode laser," *Elect. Lett.*, vol. 16, pp. 620-621, 31 Jul. 1980.
181. J. P. van der Ziel and R. M. Mikulyak, "Mode locking of strip buried heterostructure (AlGa)As lasers using an external cavity," *J. Appl. Phys.*, vol. 51, pp. 3033-3037, Jun. 1980.

182. N. A. Olsson and W. T. Tsang, "Transient effects in external cavity semiconductor lasers," *IEEE J. Quantum Electron.*, vol. QE-19, pp. 1479-1481, Oct. 1983.
183. R. Ludeke and E. P. Harris, "Tunable GaAs laser in an external dispersive cavity," *Appl. Phys. Lett.*, vol. 20, pp. 499-500, 15 Jun. 1972.
184. J. A. Rossi, S. R. Chinn, and H. Heckscher, "High-power narrow-linewidth operation of GaAs diode lasers," *Appl. Phys. Lett.*, vol. 23, pp. 25-27, 1 Jul. 1973.
185. D. Akkerman, A. P. Bogatov, P. G. Eliseev, Z. Raab, and B. N. Sverdlov, "Injection laser with a diffraction grating in its resonator," *Sov. J. Quant. Electron.*, vol. 4, pp. 626-628, Nov. 1974.
186. H. Heckscher and J. A. Rossi, "Flashlight-size external cavity semiconductor laser with narrow-linewidth tunable output," *Appl. Opt.*, vol. 14, pp. 94-96, Jan. 1975.
187. E. M. Philipp-Rutz, "Spatially coherent radiation from an array of GaAs lasers," *Appl. Phys. Lett.*, vol. 26, pp. 475-477, 15 Apr. 1975.
188. C. Voumard, "External-cavity-controlled 32-MHz narrow-band CW GaAlAs diode lasers," *Opt. Lett.*, vol. 1, pp. 61-63, Aug. 1977.
189. H. Sato, K. Itoh, M. Fukai, and N. Suzuki, "Single longitudinal mode control of semiconductor lasers by rectangular conical diffractor system for wavelength-division-multiplexing transmission," *IEEE J. Quantum Electron.*, vol. QE-18, pp. 328-332, Mar. 1982.
190. H. Sato, H. Asakura, M. Fukai, and N. Suzuki, "Design of nondispersion optical feedback system using diffraction grating for semiconductor laser multiple longitudinal modes control," *IEEE J. Quantum Electron.*, vol. QE-18, pp. 155-157, Feb. 1982.
191. R. Wyatt and W. J. Devlin, "10 kHz linewidth 1.5  $\mu\text{m}$  InGaAsP external cavity laser with 55nm tuning range," *Elect. Lett.*, vol. 19, pp. 110-111, 3 Feb. 1983.
192. J. R. Andrews, "Single mode operation of a current pulsed GaAlAs laser with dispersive external feedback," *Appl. Phys. Lett.*, vol. 44, pp. 5-7, 1 Jan. 1984.
193. E. Mohn, "Properties of a GaAs laser coupled to an external cavity," *1968 Symposium on GaAs*, pp. 101-109, 1968.
194. R. F. Broom, E. Mohn, C. Risch, and R. Salathe, "Microwave self-modulation of a diode laser coupled to an external cavity," *IEEE J. Quantum Electron.*, vol. QE-6, pp. 328-334, Jun. 1970.
195. P. D. Wright, J. J. Coleman, N. Holonyak, M. J. Ludowise, and G. E. Stillman, "Homogeneous or inhomogeneous line broadening in a semiconductor laser: observations on  $\text{In}_{1-x}\text{Ga}_x\text{P}_{1-z}\text{As}_z$  double heterojunctions in an external grating cavity," *Appl. Phys. Lett.*, vol. 29, pp. 18-20, 1 Jul. 1976.
196. T. Kanada and K. Nawata, "Injection laser characteristics due to reflected optical power," *IEEE J. Quantum Electron.*, vol. QE-15, pp. 559-565, Jul. 1979.

197. P. D. Wright, E. A. Rezek, M. J. Ludowise, and N. Holonyak, Jr., "Near-infrared  $\text{In}_{1-x}\text{Ga}_x\text{P}_{1-z}\text{As}_z$  double-heterojunction lasers: constant-temperature LPE growth and operation in an external-grating cavity," *IEEE J. Quantum Electron.*, vol. QE-13, pp. 637-642, Aug. 1977.
198. R. Lang and K. Kobayashi, "External optical feedback effects on semiconductor injection laser properties," *IEEE J. Quantum Electron.*, vol. QE-16, pp. 347-355, Mar. 1980.
199. L. A. Glasser, "A Linearized Theory for the diode laser in an external cavity," *IEEE J. Quantum Electron.*, vol. QE-16, pp. 525-531, May 1980.
200. Y. Mitsuhashi, T. Morikawa, J. Shimada, K. Sakurai, and S. Mitsutsuka, "Polarization-rotated optical feedback in self-coupled optical pickup," *Opt. co.*, vol. 34, pp. 309-310, Sep. 1980.
201. S. Saito and Y. Yamamoto, "Direct observation of Lorentzian lineshape of semiconductor laser and linewidth reduction with external grating feedback," *Elect. Lett.*, vol. 17, pp. 325-327, 30 Apr. 1981.
202. A. Olsson and C. L. Tang, "Coherent optical interference effects in external-cavity semiconductor lasers," *IEEE J. Quantum Electron.*, vol. QE-17, pp. 1320-1323, Aug. 1981.
203. M. Fleming and A. Mooradian, "Spectral characteristics of external-cavity controlled semiconductor lasers," *IEEE J. Quantum Electron.*, vol. 17, pp. 44-59, Jan. 1981.
204. R. H. Rediker, "Communications: Fiber-Coupled External Cavity Semiconductor Laser," (U. S. O. N. R. Contrac # N00014-80-C-0941), Res. Lab. of Electronics, M. I. T., Cambridge, Mass., Jul. 1981.
205. Y. Mitsuhashi, J. Shimada, and S. Mitsutsuka, "Voltage change across the self-coupled semiconductor laser," *IEEE J. Quantum Electron.*, vol. QE-17, pp. 1216-1225, Jul. 1981.
206. L. Goldberg, H. F. Taylor, A. Dandridge, J. F. Weller, and R. O. Miles, "Spectral characteristics of semiconductor lasers with optical feedback," *IEEE J. Quantum Electron.*, vol. QE-18, pp. 555-563, Apr. 1982.
207. R. P. Salathe, "Diode lasers coupled to external resonators," *Appl. Phys.*, vol. 20, pp. 1-18, 1979.
208. T. Yabuzaki, A. Ibaragi, H. Hori, M. Kitano, and T. Ogawa, "Frequency-locking of a GaAlAs Laser to a doppler-free spectrum of the Cs-D<sub>2</sub> line," *Japan. Jnl. Appl. Phys.*, vol. 20, pp. 451-453, Jun. 1981.
209. S. Yamaguchi and M. Suzuki, "Frequency locking of an InGaAsP semiconductor laser to the first overtone vibration-rotation lines of hydrogen fluoride," *Appl. Phys. Lett.*, vol. 41, pp. 1034-1036, 1 Dec. 1982.
210. E. Hecht and A. Zajac, *Optics*, Addison-Wesley, Reading, MA, 1976.
211. V. N. Smiley, "Conditions for zero reflectance of thin dielectric films on laser materials," *J. O. S. A.*, vol. 58, pp. 1469-1475, Nov. 1968.
212. A. Yariv, *Introduction to Optical Electronics*, Holt, Rinehart and Winston, New York, N.Y., 1976.

213. A. Yariv, "Coupled-mode theory for guided-wave optics," *IEEE J. Quantum Electron.*, vol. QE-9, pp. 919-933, Sep. 1973.
214. R. G. Hunsperger, A. Yariv, and A. Lee, "Parallel end-butt coupling for optical integrated circuits," *Appl. Opt.*, vol. 16, pp. 1026-1032, Apr. 1977.
215. R. R. Rice, "Injection laser waveguide coupler," Final Report for NRL Contract #N00173-78-C-0087, pp. 1-73, Defense Technical Information Center, Jun. 1979.
216. C. T. Mueller, C. T. Sullivan, W. S. C. Chang, D. G. Hall, J. D. Zino, and R. R. Rice, "An analysis of the coupling of an injection laser diode to a planar LiNbO<sub>3</sub> waveguide," *IEEE J. Quantum Electron.*, vol. QE-16, pp. 363-372, Mar. 1980.
217. W. L. Emkey, "Optical coupling between single-mode semiconductor lasers and strip waveguides," *Jour. Lightw. Tech.*, vol. LT-1, pp. 436-443, Jun. 1983.
218. M. Born and E. Wolf, *Principles of Optics*, Pergamon Press, New York, N.Y., 1975. Fifth Edition
219. D. K. Killinger and N. Menyuk, "Remote probing of the atmosphere using a CO<sub>2</sub> DIAL system," *IEEE J. Quantum Electron.*, vol. QE-17, pp. 1917-1929, Sep. 1981.
220. W. D. Egan, R. T. Boos, R. K. DeFreez, and R. L. Byer, "Remote differential absorption and scattering measurement of methane near a coal mine working face," *Technical Digest of the Conference on Lasers and Electro-Optics*, Baltimore, MD, May 1983. Paper ThK3
221. W. G. Driscoll, Ed., *Handbook of Optics*, McGraw-Hill, New York, 1978.
222. W. G. Fastie, "A small plane grating monochromator," *J. O. S. A.*, vol. 42, pp. 641-647, Sep. 1952.
223. A. S. Filler, "Stigmatic Ebert-type plane grating mounting," *J. O. S. A.*, vol. 54, 1964.
224. W. T. Welford, "Stigmatic Ebert-type plane grating mounting," *J. O. S. A.*, vol. 53, p. 766, 1963.
225. V. L. Chupp and P. C. Grantz, "Coma cancelling monochromator with no slit mismatch," *Appl. Opt.*, vol. 8, pp. 925-929, May 1969.
226. M. A. Gil and J. M. Simon, "Coma compensation in a parabolized Ebert monochromator," *Appl. Opt.*, vol. 18, pp. 2280-2285, 1 Jul. 1979.
227. M. A. Gil and J. M. Simon, "New plane grating monochromator with off-axis parabolical mirrors," *Appl. Opt.*, vol. 22, pp. 152-158, 1 Jan. 1983.
228. J. M. Lerner and A. Thevenon, "Optimizing grating-based systems," *Las. Appl.*, pp. 89-93, Jan. 1984.
229. *A Designers Guide to Diamond Machined Optics*, Pneumo Precision, Inc., Keene, N. H., Apr. 1983.
230. K. Spanner and H. Marth, "Precise positioning with piezoelectric translators," *Las. Appl.*, pp. 61-63, Aug. 1983.

231. E. Slingland, "Microstepping for fine position control," *Las. Appl.*, pp. 55-58, Aug. 1983.
232. C. Hudson, "A guide to optical shaft encoders," *Instr. & Control Syst.*, May 1978.
233. C. B. Swan, "Improved performance of silicon avalanche oscillators mounted on diamond heat sinks," *IEEE Proc.*, pp. 1617-1618, 1967.
234. R. Berman, *Diamonds as heat sinks-a review*, D. Drukker & Zn., Amsterdam, 1970.
235. E. A. Burgemeister, "Thermal resistance at metal/diamond interfaces in relation to the mounting of microwave diodes," *J. Phys. D: Appl. Phys.*, vol. 10, pp. 1923-1929, 1977.
236. E. A. Burgemeister, "Thermal conductivity of natural diamond between 320 and 450 K," *Physica*, vol. 93B, pp. 165-179, 1978.
237. E. A. Burgemeister, "Thermal conductivity measurements by means of radiation thermometry," *Proceedings SPIE*, vol. 197, pp. 305-310, Soc. Photo. Instrum. Eng., 1979.
238. J. A. Amick, G. L. Schnable, and J. L. Vossen, "Deposition techniques for dielectric films on semiconductor devices," *J. Vac. Sci. Technol.*, vol. 14, pp. 1053-1063, Sep./Oct. 1977.
239. H. A. Macleod and A. F. Turner, "New thin-film coating processes," *Opt. Spect.*, pp. 67-68, Sep. 1981.
240. O. A. Weinreich, "Antireflection films on GaAs electroluminescent diodes," *J. Electrochem. Soc.*, vol. 110, pp. 1124-1126, Nov. 1963.
241. T. Yamamoto and K. Kawamura, "SiO evaporation on a GaAs electroluminescent diode," *Proc. IEEE*, vol. 54, pp. 1967-1968, Dec. 1966.
242. H. D. Edmonds, C. DePalma, and E. P. Harris, "Preparation and properties of SiO antireflection coatings for GaAs injection lasers with external resonators," *Appl. Opt.*, vol. 10, pp. 1591-1596, Jul. 1971.
243. M. Ettenberg, H. S. Sommers, H. Kressel, and H. F. Lockwood, "Control of facet damage in GaAs laser diodes," *Appl. Phys. Lett.*, vol. 18, pp. 571-573, 15 Jun. 1971.
244. G. Eisenstein and L. W. Stulz, "High quality antireflection coatings on laser facets by sputtered silicon nitride," *Appl. Opt.*, vol. 23, pp. 161-164, 1 Jan 1984.
245. G. Hass, "Preparation, structure, and applications of thin films of silicon monoxide and titanium dioxide," *Jour. Am. Ceram. Soc.*, vol. 33, pp. 353-360, Dec. 1950.
246. G. Hass and C. D. Salzberg, "Optical properties of silicon monoxide in the wavelength region from 0.24 to 14.0 microns," *J. O. S. A.*, vol. 44, pp. 181-187, Mar. 1954.
247. G. Hass, "Filmed surfaces for reflecting optics," *J. O. S. A.*, vol. 45, pp. 945-952, Nov. 1955.

248. A. P. Bradford, G. Hass, M. McFarland, and E. Ritter, "Effect of ultraviolet irradiation on the optical properties of silicon oxide films," *Appl. Opt.*, vol. 4, pp. 971-976, Aug. 1965.
249. J. S. Blakemore and R. K. DeFreez, "Methane detection research," , Oct. 1981. Report to Bethlehem Steel Corporation Homer Research Laboratories from Oregon Graduate Center
250. V. N. Smiley, "Mismatch of single layer antireflection coatings on laser materials," *Appl. Opt.*, vol. 7, pp. 986-987, May 1968.
251. G. Eisenstein, "Theoretical design of single-layer antireflection coatings on laser facets," *B. L. T. J.*, vol. 63, pp. 357-364, Feb. 1984.
252. R. W. Hoffman, "The Mechanical Properties of Thin Films," in *The Use of Thin Films in Physical Investigations*, ed. J. C. Anderson, pp. 261-281, Academic Press, New York, N. Y., 1966.
253. J. R. Vig, "UV/Ozone Cleaning of Surfaces: A Review," in *Surface Contamination*, ed. K. L. Mittal, vol. 1, pp. 235-254, Plenum Press, New York, N. Y..
254. W.W. Balwanz, "Plasma Cleaning of Surfaces," in *Surface Contamination*, ed. K. L. Mittal, vol. 1, pp. 255-270, Plenum Press, New York, N. Y..
255. W. T. Tsang, N. A. Olsson, and R. A. Logan, "High-speed direct single-frequency modulation with large tuning rate and frequency excursion in cleaved-coupled-cavity semiconductor lasers," *Appl. Phys. Lett.*, vol. 42, pp. 650-652, 15 Apr. 1983.
256. H. Temkin, J. P. van der Ziel, R. A. Linke, and R. A. Logan, "Single mode operation of 1.5  $\mu\text{m}$  cleaved-coupled-cavity InGaAsP lasers," *Appl. Phys. Lett.*, vol. 43, pp. 723-725, 15 Oct. 1983.
257. L. A. Coldren, T. L. Koch, C. A. Burrus, and R. G. Swartz, "Intercavity coupling gap width dependence in coupled-cavity lasers," *Electron. Lett.*, vol. 19, pp. 350-352, 12 Apr. 1984.
258. G. P. Agrawal, N. A. Olsson, and N. K. Dutta, "Reduced chirping in coupled-cavity-semiconductor lasers," *Appl. Phys. Lett.*, vol. 45, pp. 119-121, 15 Jul. 1984.
259. T. P. Lee, C. A. Burrus, P. L. Liu, W. B. Sessa, and R. A. Logan, "An investigation of the frequency stability and temperature characteristics of 1.5  $\mu\text{m}$  coupled-cavity injection lasers," *IEEE J. Quantum Electron.*, vol. QE-20, pp. 374-384, Apr. 1984.
260. R. K. DeFreez, T. L. Paoli, M. Bernstein, and R. D. Burnham, "CW operation of a cleaved-coupled-cavity array of phased-locked GaAlAs lasers," *Electron. Lett.*, vol. 21, pp. 241-242, 14 Mar. 1985.
261. R. A. McClatchey, W. S. Benedict, S. A. Clough, D. E. Burch, R. F. Calfee, K. Fox, L. S. Rothman, and J. S. Garing, *AFCRL Atmospheric Absorption Line Parameters Compilation*, Air Force Cambridge Research Laboratories, Bedford, Mass., 1973.
262. *American National Standard for the Safe Use of Lasers*, American National Standards Institute, Inc., New York, N.Y., 1980.

263. E. M. Pugh and G. H. Winslow, *The Analysis of Physical Measurements*, Addison-Wesley, Reading, MA, 1966.
264. D. K. Killinger and N. Menyuk, "Remote probing of the atmosphere using a CO<sub>2</sub> DIAL system," *IEEE J. Quantum Electron.*, vol. QE-17, pp. 1917-1929, Sep. 1981.
265. A. Yariv, *Introduction to Optical Electronics*, Holt, Rinehart and Winston, New York, N.Y., 1976.
266. *Germanium photodiode application note #501*, Judson Infrared Inc., 1981.
267. C. T. Mueller, C. T. Sullivan, W. S. C. Chang, D. G. Hall, J. D. Zino, and R. R. Rice, "An analysis of the coupling of an injection laser diode to a planar LiNbO<sub>3</sub> waveguide," *IEEE J. Quantum Electron.*, vol. QE-16, pp. 363-372, Mar. 1980.
268. W. L. Emkey, "Optical coupling between single-mode semiconductor lasers and strip waveguides," *Jour. Lightw. Tech.*, vol. LT-1, pp. 436-443, Jun. 1983.
269. E. Hecht and A. Zajac, *Optics*, Addison-Wesley, Reading, MA, 1976.
270. G. H. B. Thompson, *Physics of Semiconductor Laser Devices*, John Wiley & Sons, New York, N.Y., 1980.
271. H. C. Casey and M. B. Panish, *Heterostructure Lasers: Part A: Fundamental Principles*, Academic Press, New York, N.Y., 1978. Chapter 2

## APPENDIX A

This appendix lists the computer source program used to generate data for plots of optical transmission versus wavenumber, for a specified methane concentration, and for a specified spectral resolution. Plots for the P, Q, and R branches of the  $2\nu_3$  methane absorption so generated are shown in Figures 3 through 11 in Chapter 3.

This program is a modification of a listing presented in an AFCRL document<sup>261</sup>.



## REQUESTED OPTIONS:

OPTIONS IN EFFECT: NAME(MAIN) OPTIMIZE(2) LINE(COUNT) SIZE(MAX) AUTO(LENGTH) SOURCE(BASIC) MULTI(MODFLK) OBJ(CC) MAP(NOFOR) MAT(GUST) NOK(REF) NOALC(NOANSF) TERM(CM FLAG(1))

```

C      PROGRAM MATRNS                                MX100010
ISN 0002      IMPLICIT REAL*8 (A-H,O-Z)              MX100020
ISN 0003      DIMENSION GND(5000), S(5000), ALPHA(5000), LDP(5000) MX100030
ISN 0004      DIMENSION UPD(5000), FNU(5000), TRANS(5000) MX100040
ISN 0005      DEFINE FILE 1(20000,110,F,111) MX100050
ISN 0006      DEFINE FILE 7(5000,110,F,122) MX100060
ISN 0007      DEFINE FILE 8(5000,110,F,122) MX100070
ISN 0008      DEFINE FILE 9(5000,110,F,122) MX100080
ISN 0009      DEFINE FILE 10(5000,110,F,122) MX100090
ISN 0010      DEFINE FILE 11(5000,110,F,122) MX100100
ISN 0011      DEFINE FILE 12(5000,110,F,122) MX100110
ISN 0012      DEFINE FILE 13(5000,110,F,122) MX100120
ISN 0013      DEFINE FILE 14(5000,110,F,122) MX100130
ISN 0014      DEFINE FILE 15(5000,110,F,122) MX100140
ISN 0015      REAL*8 LAMBDA MX100150
ISN 0016      INTEGER*4 LNTB MX100160
ISN 0017      NAMELIST/NAME1/P1,F/NAME2/W/NAME3/V1,V2,DV,BOUND,A,DELV/NAME4/Z1
ISN 0018      NAMELIST/NAME5/V1,V2,A MX100180
C
C
C
C
C      PROGRAM BY RICK DEFREEZ
C
C
C      THIS PROGRAMS GENERATES A TRANSMITTANCE SPECTRUM WITH OUTPUT
C      RESULTS PRINTED EVERY 0.1% WAVENUMBERS BETWEEN THE INITIAL
C      FREQUENCY, V1, AND THE FINAL FREQUENCY, V2.
C      CALCULATIONS ARE PERFORMED FOR A UNIFORM CONSTANT PRESSURE, CON-
C      STANT TEMPERATURE PATH CONTAINING THE MOLECULAR SPECIES IN THE
C      REPERENCED FILE IN ARBITRARY AMOUNTS. MOLECULAR ABUNDANCES MUST
C      BE SPECIFIED IN THE UNITS: MOLECULES/CM**2. MINICHROMATIC
C      CALCULATIONS ARE MADE AT 0.1% FREQUENCY INTERVALS AND A TRIANGULAR
C      SLIT FUNCTION OF HALF-WIDTH, A, IS CONVOLVED WITH THE MINICH-
C      ROMATIC RESULTS.
ISN 0019      14 DEPTH=.0001 MX100190
ISN 0020      P1=1.141502E3 MX100200
ISN 0021      SUM=0.0 MX100210
ISN 0022      IV=1 MX100220
C      READ INPUT PARAMETERS: P=PRESSURE IN MBARS, T=TEMPERATURE IN
C      K, V1 AND V2 ARE THE FREQUENCY LIMITS FOR WHICH OUTPUT RESULTS
C      ARE REQUIRED. DV IS MINICHROMATIC FREQUENCY INCREMENT. BOUND
C      IS THE FREQUENCY FROM ANY LINE CENTER BEYOND WHICH THE LINE
C      WILL BE NEGLECTED. A IS THE HALF-WIDTH OF A TRIANGULAR SLIT
C      FUNCTION. DELV IS THE FREQUENCY INCREMENT OF CONVOLVED OUTPUT
C      TRANSMITTANCE RESULTS.
ISN 0023      C IF (11.EQ.1) GO TO 44 MX100230
ISN 0024      LNTB=7 MX100240
ISN 0025      NBL(15,1000) MX100250
ISN 0026      NAME(15,NAME1) MX100260
ISN 0027      NAME(15,NAME2) MX100270
ISN 0028      NAME(15,NAME3) MX100280

```

```

LEVEL 2-3.0 (JUNE 76)      NAME      OS/360 FORTRAN H EXTENDED      DATE 80.224/17.36.37      PAGE 2

ISN 0029      WRITE(6,1010)                                MXT00540
ISN 0030      READ(5,NAM2)                                  MXT00550
ISN 0031      WRITE(6,NAM2)                                  MXT00560
ISN 0032      WRITE(6,1020)                                  MXT00570
ISN 0033      READ(5,NAM3)                                  MXT00580
ISN 0034      WRITE(6,NAM3)                                  MXT00590
ISN 0035      GO TO 24                                       MXT00600
ISN 0036      44      CONTINUE                                MXT00610
ISN 0037      WRITE(6,2400)                                  MXT00620
ISN 0038      READ(5,NAM5)                                  MXT00630
ISN 0039      WRITE(6,NAM5)                                  MXT00640
C
C
C
C      IF (A*Z/DV+1.GT.5000) CALCULATION CANNOT BE DONE.
C      IF THERE ARE READ MORE THAN 5000 LINES IN A FREQUENCY RANGE OF
C      Z(A+BOUND) CALCULATION CANNOT BE DONE.
C
C
C
C
ISN 0040      24      VDOT=V1-A-BOUND                                MXT00710
ISN 0041      VTOP=V2+A+BOUND                                MXT00740
ISN 0042      J=1                                             MXT00750
ISN 0043      DO 9 K=1,20000                                MXT00760
ISN 0044      READ(11,K,95) GNU(1), S(1), ALPHA(1), EDP(1)
ISN 0045      IF (GNU(1).L1.VNU(1)) GO TO 9
ISN 0046      PATH=S(1)*V/(P1+.0001/1013.0)
ISN 0047      IF (PATH.LT.0.EP(1)) GO TO 9
ISN 0048      IF (GNU(1).GT.VTOP) GO TO 11
ISN 0049      I=1+1
ISN 0050      9      CONTINUE
ISN 0051      11      I=I+1
ISN 0052      WRITE(6,97) VDOT,VTOP,GNU(1),I
ISN 0053      IS=1
ISN 0054      VZF=GNU(1)-BOUND-A
ISN 0055      IS=1
ISN 0056      PD=1013.00
ISN 0057      TD=296.00
ISN 0058      CS1=(10-I)/(10+I+.59*6)
ISN 0059      C
ISN 0060      ROTATIONAL PARTITION FUNCTION IS DEFINED BELOW.
ISN 0061      C
ISN 0062      CS2=(TD/Y1)+1.5
ISN 0063      CA=((TD/Y1)+4.5)*(D/PD)
C
C      TEMPERATURE DEPENDENCE OF ALL LINE INTENSITIES COMPUTED HERE
C
C
ISN 0064      DO 23 I=1,11
ISN 0065      S(I)=S(1)*CS2*DEXP(-EDP(1)+CS1)
ISN 0066      ALPHA(I)=ALPHA(1)+CA
ISN 0067      23      CONTINUE
ISN 0068      V=V1-A
ISN 0069      25      CATI=0.0
ISN 0070      SUMI=0.0
C
C      DETERMINE INDICES (15 AND 16) INDICATING WHICH SPECTRAL LINES
C      ARE TO BE USED IN THE CALCULATION AT FREQUENCY V.
C

```

```

ISN 0071      DO 33 I=15,11                                MXT01130
ISN 0072      IF (V-UBOUND-GNU(I))29,29,33                MXT01140
ISN 0073      33 CONTINUE                                  MXT01150
ISN 0074      GO TO 34                                     MXT01160
ISN 0075      29 I5=I                                      MXT01170
ISN 0076      GO TO 35                                     MXT01180
ISN 0077      34 I5=I1                                     MXT01190
ISN 0078      GO TO 49                                     MXT01200
ISN 0079      35 DO 39 J=25,11                            MXT01210
ISN 0080      27 (V+DBOUND+GNU(J)) 37,37,39              MXT01220
ISN 0081      37 I6=J-1                                    MXT01230
ISN 0082      GO TO 43                                     MXT01240
ISN 0083      39 CONTINUE                                  MXT01250
ISN 0084      I6=I1                                       MXT01260
C
C COMPUTE THE OPTICAL DEPTH AND TRANSMITTANCE AT FREQUENCY V. MXT01270
C
C
ISN 0085      43 DO 45 I=15,16                              MXT01300
ISN 0086      Z=DABS(V-GNU(I))                             MXT01310
ISN 0087      S=1/(1+ALPHA(I))/(Z**2+ALPHA(I)**2)         MXT01320
ISN 0088      CAY=CAY1+S*H1                                 MXT01330
ISN 0089      45 CONTINUE                                  MXT01340
ISN 0090      CAY=CAY1*W                                    MXT01350
ISN 0091      OPD(I)=CAY*0.3183                            MXT01360
ISN 0092      GO TO 51                                     MXT01370
ISN 0093      49 OPD(I)=0.0                                  MXT01380
ISN 0094      51 OPD(I)=0.0EXP(-OPD(I)*I)                 MXT01390
ISN 0095      IF (V+DV).GT.V2P) GO TO 53                  MXT01400
ISN 0097      IF (V+GE.V2+A) GO TO 53                     MXT01410
ISN 0099      IF (V-GE.V000) GO TO 53                     MXT01420
ISN 0101      ZV=V+1                                       MXT01430
ISN 0102      V=V+DV                                       MXT01440
ISN 0103      GO TO 25                                     MXT01450
C
C AT THIS POINT, CYCLE BACK TO STATEMENT 25 AND COMPUTE THE MXT01460
C MONOCHROMATIC TRANSMITTANCE AT V+DV.                    MXT01470
C IF STATEMENT 53 IS REACHED, ALL POSSIBLE MONOCHROMATIC TRANS- MXT01480
C MITTANCE VALUES HAVE BEEN COMPUTED, AND THE SLIT FUNCTION CON- MXT01490
C VOLUTION WILL NOW BE PERFORMED IN LOOP 57.              MXT01500
C
C
ISN 0104      53 FREQ=V1                                     MXT01510
ISN 0105      F1NAL=V1+5000.*DV-A-DELV                    MXT01520
ISN 0106      V=V1-A                                       MXT01530
ISN 0107      JFNU=1                                        MXT01540
ISN 0108      L=0.5*LV/DV+.01                              MXT01550
ISN 0109      ZA=1                                         MXT01560
ISN 0110      55 S=0.0                                      MXT01570
ISN 0111      DO 57 I=14,1V                                MXT01580
ISN 0112      S=S+(A-DABS(V-FREQ))+OPD(I)                 MXT01590
ISN 0113      V=V+DV                                       MXT01600
ISN 0114      IF (V-(FREQ+A)) 57,59,59                    MXT01610
ISN 0115      57 CONTINUE                                  MXT01620
ISN 0116      59 TRANSMIT(S)=S*0.5/(1+A*A)               MXT01630
ISN 0117      FNU(JFNU)=FNU0                                MXT01640
ISN 0118      IF (FREQ.GT.V2) GO TO 61                     MXT01650
ISN 0120      IF (FREQ.GE.V2P) GO TO 61                     MXT01660
ISN 0122      IF (FREQ.LE.F1NAL) GO TO 61                  MXT01670

```

LEVEL 2,3,0 (JUNE 78)	MAIN	US/360 FORTRAN II EXTENDED	DATE 80-224/17,36,32	PAGE 4
15N 0124		FRPO=FRQ*DELTA		NXT01710
15N 0125		IF (JFNU-GE,5000) GO TO 61		NXT01720
15N 0127		JFNU=JFNU+1		NXT01730
15N 0129		IA=IA+L		NXT01740
15N 0129		V=FRQ-A		NXT01750
15N 0130		GO TO 55		NXT01760
	C			NXT01770
	C	CONVOLVED TRANSMITTANCE RESULTS NOW PRINTED OUT		NXT01780
	C			NXT01790
15N 0131	61	WRITE(CNTR*2,2002)W		NXT01800
15N 0132		WRITE(CNTR*3,2003)P,T		NXT01810
15N 0133		WRITE(CNTR*4,2004)V1,V2		NXT01820
15N 0134		WRITE(CNTR*5,2005)A,B,BOUND		NXT01830
15N 0135		WRITE(CNTR*6,2006)DV,DELTA		NXT01840
15N 0136		JFNU=JFNU+1		NXT01850
15N 0137		DO 64 J,T,JFNU		NXT01860
15N 0136		LAMBDA=1.0E4/FNU(J-6)		NXT01870
15N 0139		WRITE(CNTR*J,105) FNU(J-6),LAMBDA,TRANS(J-6)		NXT01880
15N 0140				NXT01890
15N 0141	64	CONTINUE		NXT01900
15N 0141		IF(FREQ-GE,V2) GO TO 75		NXT01910
15N 0141		IF(JFNU-GE,5000) GO TO 65		NXT01920
15N 0145		IF(FREQ-GE,FINAL) GO TO 63		NXT01930
15N 0147		GO TO 75		NXT01940
15N 0148	63	V=FINAL*DFLV		NXT01950
15N 0149		IS=1		NXT01960
15N 0150		IV=1		NXT01970
15N 0151		JFNU=1		NXT01980
15N 0152		V=V-A		NXT01990
15N 0153		GO TO 25		NXT02000
15N 0154	65	IA=IA+L		NXT02010
	C			NXT02020
	C	IF STATEMENT 65 IS REACHED, ADDITIONAL MINICHROMATIC CALCULATIONS		NXT02030
	C	ARE REQUIRED TO SATISFY THE TOTAL THROUGHLY RANGE OVER WHICH		NXT02040
	C	CONVOLVED RESULTS ARE REQUIRED		NXT02050
	C			NXT02060
15N 0155		JFNU=1		NXT02070
15N 0156		V=FRQ-A		NXT02080
15N 0157		GO TO 55		NXT02090
15N 0158	75	WRITE(6,1200)		NXT02100
15N 0159		HEAD(5,NAM4)		NXT02110
15N 0160		IF(11.EQ,1) GO TO 14		NXT02120
15N 0162		CALL EXIT		NXT02130
15N 0163		STOP		NXT02140
15N 0164	95	FORMAT(10,3,F10.3,F5.3,F10.3)		NXT02150
15N 0165	97	FORMAT(1X,'VIB=' F12.3,'VIBP=' F12.3,'GNUM=' F12.3,'II=' F10.3)		NXT02160
15N 0166	105	FORMAT(10,3,F10.5,F12.5)		NXT02170
15N 0167	1000	FORMAT(' INPUT P,T: F12.5,F7.2 NAM1')		NXT02180
15N 0168	1010	FORMAT(1X,'INPUT CONCENTRATION IN MOLECULES/CM^2:F10.3 NAM2')		NXT02190
15N 0169	1020	FORMAT(1X,'INPUT F10.3:V1,V2,DV,BOUND,A,DELTA NAM3')		NXT02200
15N 0170	1200	FORMAT(1X,'DO YOU WISH TO TRY NEW FREQUENCY RANGE AND A NEW		NXT02210
		CRAND=1 THY NAM4 11E1 FOR YES')		NXT02220
15N 0171	2002	FORMAT(40X,'CONCENTRATION=' F10.3)		NXT02230
15N 0172	2003	FORMAT(40X,'PRESSURE=' F12.5,'TEMP=' F7.2)		NXT02240
15N 0173	2004	FORMAT(40X,'NU LOW=' F10.3,'NU HIGH=' F10.3)		NXT02250
15N 0174	2005	FORMAT(40X,'BANDWIDTH=' F10.3,'X,WIDTH=' F10.3)		NXT02260
15N 0175	2006	FORMAT(40X,'DV=' F10.3,'X,DELTA=' F10.3)		NXT02270
15N 0176	2400	FORMAT(1X,'INPUT V1,V2,A NAM1')		NXT02280
15N 0177		END		NXT02290

## APPENDIX B

This appendix presents a safety calculation for a 1.6  $\mu\text{m}$  collimated repetitively pulsed diode laser. It is based on the "American National Standard for the Safe Use of Lasers"<sup>262</sup>. The explanation below is paraphrased from Section B.3.1.2 of that document. The calculation presented is similar to Example 4 therein.

To determine the maximum safe exposure for a repetitively pulsed laser, the wavelength, PRF, duration of a single pulse, and duration of a complete exposure must be known. This determination requires two analyses and a conclusion. Steps 1 and 2 and Step 3, respectively, in the following calculation.

The calculation determines the intrabeam direct-viewing exposure for a  $\text{In}_{0.53}\text{Ga}_{0.47}\text{As}/\text{InP}$  ( $\lambda \approx 1.6 \mu\text{m}$ ) laser of pulse duration ( $\tau$ ) equal to 100 ns and PRF = 10 kHz. Since the 1.6  $\mu\text{m}$  wavelength light will not cause a natural eye aversion response, as a visible-wavelength laser would, a 1 second exposure duration (T) is assumed.

### Step 1. Individual Pulse Limitation

This step requires the calculation of the maximum exposure based on the limitation that a single-pulse exposure shall not exceed the single pulse maximum per-

missible exposure (MPE) (ANSI Sections 8.5.1.1 and 8.5.1.5) multiplied by a correction factor ( $F_1$ ) of ANSI Figure 12. From that figure,  $F = 0.06$  for a PRF = 10 kHz. The maximum exposure for an individual pulse is given by

$$H_i = F_1(\text{MPE}) = (0.06)(10^{-2} \text{ Jcm}^{-2}) = 6.0 \times 10^{-4} \text{ Jcm}^{-2}. \quad (\text{B.1})$$

On this basis, the maximum exposure for a train of pulses is given by

$$H = H_i(\text{PRF})T = (6.0 \times 10^{-4})(10^3 \text{ Hz})(1 \text{ Sec}) = 6 \times 10^{-1} \text{ Jcm}^{-2}. \quad (\text{B.2})$$

### Step 2. Average Power Limitation

The average power limitation requires the calculation of the total radiant exposure for the total pulse duration. From ANSI Figure 6, for  $T = 1 \text{ Sec}$  the maximum exposure is given by

$$H = 5.6 \times 10^{-1} \text{ Jcm}^{-2}. \quad (\text{B.3})$$

### Step 3. Conclusion

Comparing the results of Step 1 and Step 2, the more restrictive limitation applies. Step 2 is more restrictive and hence applicable. This implies that the maximum single pulse exposure is given by

$$H_i = 5.6 \times 10^{-5} \text{ Jcm}^{-2}. \quad (\text{B.4})$$

This result then gives a peak power density for each pulse

$$D_p = \frac{H_i}{\tau} = \frac{5.6 \times 10^{-5} \text{ Jcm}^{-2}}{10^{-7} \text{ Sec}} = 560 \text{ Wcm}^{-2}. \quad (\text{B.5})$$

Assuming a 1 mm laser beam diameter (ANSI Section 3.2.3.3), the resulting peak power is

$$P_p = D_p \pi \frac{D^2}{4} = 4.3 \text{ W} \quad (\text{B.6})$$

where  $D$  is the beam diameter. This power value is the upper limit to exempt laser status.

## APPENDIX C

The relationship between the RDIAL measurement accuracy and the measurement precision of voltage is presented in this appendix. This relationship is derived from the fundamental RDIAL expression, Equation 2.5.

The derivation proceeds in two steps. In the first step, Equation 2.5 is inverted to solve for the gas concentration implicit in the absorption coefficient. In the second step, error propagation analysis is applied to the inverted Equation, C.17.

### C.1 Inversion

The fundamental expression, Equation 2.5, is given by

$$P_r(R) = \left( \frac{\beta \Delta R}{4\pi} \right) K P_o \left( \frac{A}{R^2} \right) e^{-2 \int_0^R \alpha(r) dr} \quad (C.1)$$

where  $\beta$  = Mie backscatter coefficient,  $\Delta R$  = sample depth,  $R$  = distance to the sample volume center,  $P_o$  = power transmitted,  $P_r$  = power returned,  $K$  = optical system efficiency,  $A$  = receiver area, and  $\alpha$  = methane absorption coefficient.

As is explained in Chapter 5, the geometrically range resolved DIAL process requires two light pulses each returning light from two locations, at  $R_1$  and  $R_2$ , respectively. In what follows, pulse #1 refers to the on absorption line pulse in the



DIAL process. Pulse #2 refers to the off line pulse. Also,  $R_2 - R_1 = \Delta R$ . For pulse #1:

$$P_{r,on}(R_2) = \frac{\beta_{Mie}(R_2)}{4\pi} K_2 A_2 P_{o,1} \frac{\Delta R}{R_2^2} \exp\left(-2\bar{\alpha}_{ABS,on,2} R_2\right) \quad (C.2)$$

$$P_{r,on}(R_1) = \frac{\beta_{Mie}(R_1)}{4\pi} K_1 A_1 P_{o,1} \frac{\Delta R}{R_1^2} \exp\left(-2\bar{\alpha}_{ABS,on,1} R_1\right). \quad (C.3)$$

For pulse #2:

$$P_{r,off}(R_2) = \frac{\beta_{Mie}(R_2)}{4\pi} K_2 A_2 P_{o,2} \frac{\Delta R}{R_2^2} \exp\left(-2\bar{\alpha}_{ABS,off,2} R_2\right) \quad (C.4)$$

$$P_{r,off}(R_1) = \frac{\beta_{Mie}(R_1)}{4\pi} K_1 A_1 P_{o,2} \frac{\Delta R}{R_1^2} \exp\left(-2\bar{\alpha}_{ABS,off,1} R_1\right). \quad (C.5)$$

In Equations C.2 through C.5 the superscript bar indicates the average absorption coefficient over the given range  $R$ . Also,  $\alpha = \alpha_{ABS}$  as explained in Chapter 5.

Writing the light powers of the above equations as voltages through the use of square law detectors, the following definitions are made:

$$N_{on} \equiv \ln \left[ \frac{V_{r,on}(R_2)}{V_{r,on}(R_1)} \right] \quad (C.6)$$

and

$$N_{off} \equiv \ln \left[ \frac{V_{r,off}(R_2)}{V_{r,off}(R_1)} \right] \quad (C.7)$$

As a first step toward inversion of Equations C.2 through C.5, substitution of

those equations into C.6 and C.7 and subtraction gives:

$$N_{\text{on}} - N_{\text{off}} = -2\bar{\alpha}_{\text{ABS,on},2}R_2 + 2\bar{\alpha}_{\text{ABS,on},1}R_1 + 2\bar{\alpha}_{\text{ABS,off},2}R_2 - 2\bar{\alpha}_{\text{ABS,off},1}R_1. \quad (\text{C.8})$$

It is convenient to introduce the following definitions:

$$\bar{\alpha}_{\text{ABS,on},2}R_2 \equiv \bar{\alpha}_{\text{ABS,on},1}R_1 + \bar{\alpha}_{\text{ABS,on}}(R_2 - R_1) \quad (\text{C.9})$$

and

$$\bar{\alpha}_{\text{ABS,off},2}R_2 \equiv \bar{\alpha}_{\text{ABS,off},1}R_1 + \bar{\alpha}_{\text{ABS,off}}(R_2 - R_1). \quad (\text{C.10})$$

Here  $\bar{\alpha}_{\text{ABS,on}}$  is the average value of  $\alpha_{\text{ABS,on}}$  on  $[R_1, R_2]$ , and likewise for the off component.

The inversion is then nearly complete with the following observation:

$$N_{\text{on}} - N_{\text{off}} = 2(R_1 - R_2)(\bar{\alpha}_{\text{ABS,on}} - \bar{\alpha}_{\text{ABS,off}}) \quad (\text{C.11})$$

The absorption coefficients may be written as a product of the average gas concentration and the absorption cross section as follows:

$$\bar{\alpha}_{\text{ABS,on}} = \bar{C}\sigma(\lambda_{\text{on}}) \quad (\text{C.12})$$

and

$$\bar{\alpha}_{\text{ABS,off}} = \bar{C}\sigma(\lambda_{\text{off}}) \quad (\text{C.13})$$

where  $\sigma$  is the absorption cross section at wavelength  $\lambda$  and  $\bar{C}$  is the average gas concentration on  $[R_1, R_2]$ . The average gas concentration may then be written:

$$\bar{C} = \frac{N_{on} - N_{off}}{2(R_1 - R_2)[\sigma(\lambda_{on}) - \sigma(\lambda_{off})]} \quad (C.14)$$

The inversion of Equation C.1 for the gas concentration is complete with the exception that the two  $\sigma$  variables have yet to be expressed in terms of measurable parameters.

The variables  $\sigma_{on}$  and  $\sigma_{off}$  can be calculated from:

$$T = \exp \left[ -\sigma(\lambda_{on})C'l \right] = \frac{V_{on,2}}{V_{on,1}} \quad (C.15)$$

$$T = \exp \left[ -\sigma(\lambda_{off})C'l \right] = \frac{V_{off,2}}{V_{off,1}} \quad (C.16)$$

where  $C'$  is the known gas concentration in a reference cell,  $l = r_2 - r_1$ , the length of the reference cell, and  $V_{on}$  and  $V_{off}$  are reference detector voltages. The completed inversion of Equation C.1 is given by:

$$\bar{C} = \frac{C'(r_2 - r_1)}{2(R_1 - R_2)} \frac{\ln \left( \frac{V_{r,on}(R_2)}{V_{r,on}(R_1)} \right) - \ln \left( \frac{V_{r,off}(R_2)}{V_{r,off}(R_1)} \right)}{\ln \left( \frac{V_{on,1}}{V_{on,2}} \right) - \ln \left( \frac{V_{off,1}}{V_{off,2}} \right)}. \quad (C.17)$$

## C.2 Error Propagation

Error propagation analysis is now applied to the inverted Equation C.17. The analysis is carried out in terms of standard deviations of the various measured voltages and the calculated methane concentration.

The standard deviation in the concentration for small, random, and uncorrelated voltage fluctuations is given by<sup>263</sup>:

$$\sigma_{\mathcal{C}} = \left[ \sum_{i=1}^8 \left( \frac{\partial \mathcal{C}}{\partial V_i} V_i \frac{\sigma_{V_i}}{V_i} \right)^2 \right]^{1/2} \quad (\text{C.18})$$

where  $\sigma_x$  represents the standard deviation in  $x$ . The partial derivative factors in C.18 may be written:

$$\left[ \frac{\partial \mathcal{C}}{\partial V_i} \right] = \left[ \kappa \frac{1}{V_i} \right] \quad (\text{C.19})$$

where  $\kappa$  is given by:

$$\kappa = \pm \frac{C'(r_2 - r_1)}{2(R_1 - R_2)} \frac{1}{\ln \left( \frac{V_{\text{on},1}}{V_{\text{on},2}} \right) - \ln \left( \frac{V_{\text{off},1}}{V_{\text{off},2}} \right)} \quad (\text{C.20})$$

for the returned signal voltages,  $V_r$ , and

$$\left[ \frac{\partial \mathcal{C}}{\partial V_i} \right] = \left[ \kappa' \frac{1}{V_i} \right] \quad (\text{C.21})$$

where  $\kappa'$  is given by:

$$\kappa' = \pm \frac{C'(r_2 - r_1)}{2(R_1 - R_2)} \frac{\ln \left( \frac{V_{r,\text{on}}(R_2)}{V_{r,\text{on}}(R_1)} \right) - \ln \left( \frac{V_{r,\text{off}}(R_2)}{V_{r,\text{off}}(R_1)} \right)}{\left[ \ln \left( \frac{V_{\text{on},1}}{V_{\text{on},2}} \right) - \ln \left( \frac{V_{\text{off},1}}{V_{\text{off},2}} \right) \right]^2} \quad (\text{C.22})$$

for the references voltages.

The assumption is made that equal signal to noise ratios can be achieved for each measured return voltage. That is, assume:

$$\left( \frac{\sigma_V}{V} \right)_i = \left( \frac{\sigma_V}{V} \right)_j \equiv \frac{\sigma_V}{V} \quad (C.23)$$

for all  $i$  and  $j$  for the returned signals. Also it is assumed that the reference signal to noise ratios are much greater than the returned signal ratios due to the larger optical power available to the reference detectors. If the reference cell gas concentration is adjusted to obtain the absorption typically found in the remote sample volume (ie. population distribution of absorbing molecules and pressure broadened linewidths are the same)<sup>264</sup>, the following approximations can be made:

$$\ln \left[ \frac{V_{r,on}(R_2)}{V_{r,on}(R_1)} \right] \approx \ln \left[ \frac{V_{on,1}}{V_{on,2}} \right] \quad \text{and} \quad \ln \left[ \frac{V_{r,off}(R_2)}{V_{r,off}(R_1)} \right] \approx \ln \left[ \frac{V_{off,1}}{V_{off,2}} \right] \quad (C.24)$$

Equation C.24 implies  $\kappa \approx \kappa'$ .

Substitution of C.23 into C.18 then gives:

$$\sigma_C = \frac{2\sigma_V|\kappa|}{V} \quad (C.25)$$

where the  $\kappa'$  term is removed because of the large reference signal to noise ratios.

Substitution of Equation C.20 into Equation C.25 divided by Equation C.17 yields:

$$\frac{\sigma_C}{C} = 2 \frac{\sigma_V}{V} \left[ \ln \left( \frac{V_{r,on}(R_2)}{V_{r,on}(R_1)} \right) - \ln \left( \frac{V_{r,off}(R_2)}{V_{r,off}(R_1)} \right) \right]. \quad (C.26)$$

Since the absorption cross section is small in the off line portion of the RDIAL process, simplifications can be made to Equation C.26. Specifically, the small

amount of absorption implies:

$$\frac{V_{r,\text{off}}(R_2)}{V_{r,\text{off}}(R_1)} \approx 1 \quad (\text{C.27})$$

Finally, substitution of Equation C.27 into Equation C.26 gives a simple expression for the maximum allowable normalized standard deviation in the measured voltages as a function of the required gas concentration measurement accuracy and the amount of absorption in the sample volume during the on line portion of the RDIAL process:

$$\frac{\sigma_V}{V} = \frac{1}{2} \frac{\sigma_C}{C} \left[ \ln \left( \frac{V_{r,\text{on}}(R_2)}{V_{r,\text{on}}(R_1)} \right) \right] \quad (\text{C.28})$$

## APPENDIX D

Standard expressions <sup>265</sup> for, and numerical values of, the various detection noise sources of Section 5.3 are presented in this appendix.

### D.1 Background Noise

Here it is assumed that the detection system views, in addition to signal back-scattered from coal dust, a Lambertian blackbody wall. The wall is assumed to be at temperature of 20°C. The optical power received by the detection system is given by

$$P_{r, \text{BB}} = W_{\Delta\lambda} A \Omega_o \Delta\lambda \epsilon \quad (\text{D.1})$$

where  $W_{\Delta\lambda}$  is the spectral blackbody radiance,  $A$  is the area of the sources seen,  $\Omega_o$  is the solid angle of the receiver optics subtended at the source,  $\Delta\lambda$  is the spectral bandwidth of the receiving system ( $\approx 10$  nm), and  $\epsilon$  is the source emittance which is assumed to be  $\frac{1}{\pi}$ . This implies

$$P_{r, \text{BB}} = 1 \times 10^{-13} \text{watts} \quad (\text{D.2})$$

where numerical values typical to the HRL methane detection system have been

used. The calculated optical power yields the following background averaged squared noise current:

$$\overline{i_B^2} = \frac{3e^2 P_{r,BB} \eta \Delta\nu}{h\nu} = 3 \times 10^{-32} \Delta\nu \text{ Amps}^2 \quad (\text{D.3})$$

where  $e$  is the electronic charge,  $\eta$  is the detector efficiency ( $\approx 0.5$ ),  $\Delta\nu$  is the detection system electronic bandwidth in Hz,  $h\nu$  is the laser photon energy, and where 100% optical efficiency has been assumed. Additionally, an implicit assumption of no artificial light sources in the detector field of view was made.

## D.2 Detector Dark Current Noise

The averaged squared detector dark current for photodiodes, which are typically used in the near infrared, is given by

$$\overline{i_D^2} = 2e i_d \Delta\nu = 3 \times 10^{-19} i_d \Delta\nu \text{ Amps}^2 \quad (\text{D.4})$$

where  $i_d$  is the detector dark current in Amps.

## D.3 Signal Shot Noise

The averaged squared signal shot current is given by

$$\overline{i_{SN}^2} = \frac{3e^2 P_r \eta \Delta\nu}{h\nu} = 3 \times 10^{-28} \Delta\nu \text{ Amps}^2 \quad (\text{D.5})$$

where a returned optical power,  $P_r = 10^{-9}$  watts is assumed.



#### D.4 Load (Johnson) and Amplifier Noise

The averaged squared load and amplifier current noise for a voltage amplifying circuit is given by

$$\overline{i_A^2} = \frac{4K_B T_e \Delta\nu}{R_L} \quad (D.6)$$

where  $R_L$  is the load resistance,  $K_B$  is the Boltzmann constant, and the equivalent temperature is given by

$$T_e \approx (F)(290^\circ\text{K}) \quad (D.7)$$

where  $F$  is the noise figure of the amplifier. A typical value of good amplifiers is  $F = 1.3$ ;  $T_e \approx 380^\circ\text{K}$ .  $R_L$  is limited by the system time constant,  $\tau$ , through the relation

$$\tau = R_L C \quad (D.8)$$

where  $C$  is the total amplifier input capacitance. This implies

$$R_L = \frac{1}{2\Delta\nu C} \quad (D.9)$$

Thus the averaged squared noise current is given by

$$\overline{i_A^2} = 8K_B T_e C (\Delta\nu)^2 \quad (D.10)$$

where  $C$  is in units of farads. Substitution of a typical capacitance value<sup>266</sup>,  $C = 10^{-11}$  F, for a small area Ge photodiode at zero bias gives

$$\overline{i_A^2} = 4 \times 10^{-31} (\Delta\nu)^2 \text{Amps}^2 \quad (\text{D.11})$$

## APPENDIX E

This appendix presents a derivation of the spectral bandwidth for the off-axis parabolic mirror/grating diode laser cavity used in this project. This derivation uses, as was mentioned in Section 6.2., coupled mode theory as its basis.

Figure E.1 shows schematically an external grating diode laser cavity. The spatial dependence perpendicular to the diode active region of the laser waveguide circulating mode and the optical mode incident on the laser facet may be written, respectively, as:

$$\Psi_L(z=0) = A \exp \left[ \frac{-x^2}{\omega_o^2} \right] \quad (\text{E.1})$$

and

$$\Psi_I(z=0) = A' \exp \left[ \frac{-(x-a)^2}{(\beta\omega_o)^2} \right] \quad (\text{E.2})$$

where  $\omega_o$  is the spotsize of the waveguide circulating mode in the diode laser,  $\beta$  is the ratio of the spotsize of the incident wave to that of the guided wave,  $a$  is the relative displacement in the  $x$  direction of the two spots, and  $A$  and  $A'$  are proportionality constants.

The coupling efficiency between the guided and incident modes is given by<sup>267, 268</sup>

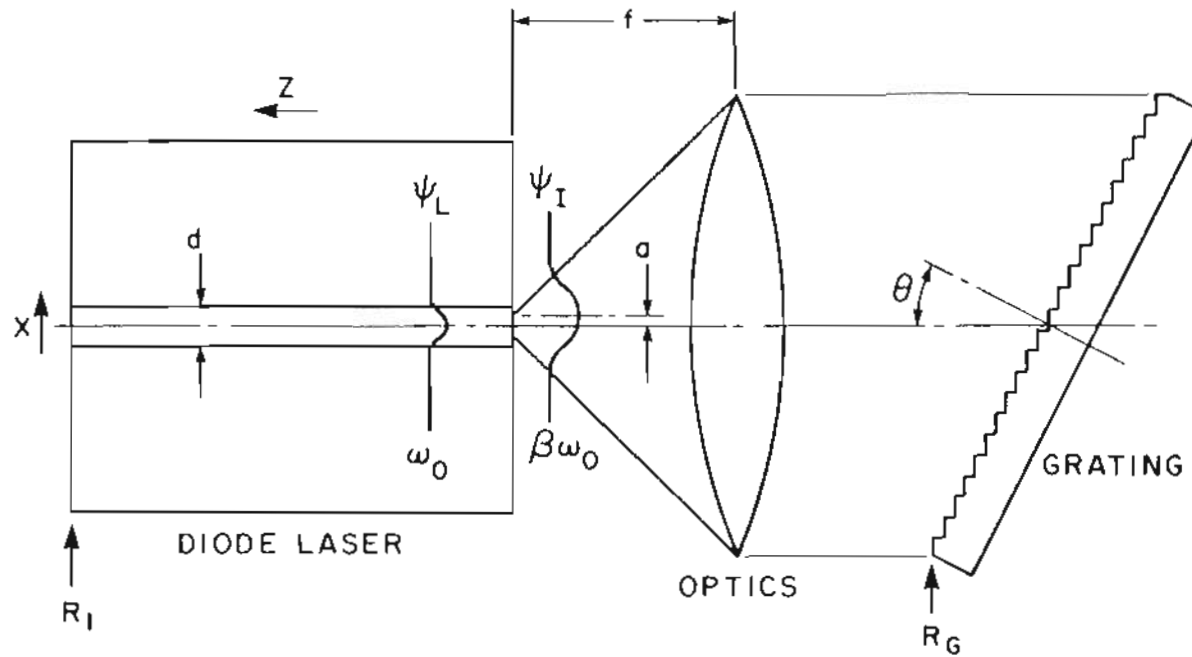


Figure E.1 Schematic representation of the dual diode laser cavity showing the diode laser circulating guided wave and the grating returned optical mode.

$$\eta = \frac{\left[ \int_{-\infty}^{\infty} \Psi_L \Psi_L^* dx \right]^2}{\int_{-\infty}^{\infty} \Psi_L \Psi_L^* dx \int_{-\infty}^{\infty} \Psi_1 \Psi_1^* dx} \quad (\text{E.3})$$

This implies by substitution that  $\eta$  may be written as

$$\eta(a, \beta) = \frac{\left[ \int_{-\infty}^{\infty} \exp \left[ -\frac{x^2}{\omega_o^2} - \frac{(x-a)^2}{(\beta\omega_o)^2} \right] dx \right]^2}{\int_{-\infty}^{\infty} \exp \left[ -2\frac{x^2}{\omega_o^2} \right] dx \int_{-\infty}^{\infty} \exp \left[ -2\frac{(x-a)^2}{(\beta\omega_o)^2} \right] dx} \quad (\text{E.4})$$

Evaluation of the integrals in Equation E.4 leads to the following expression for  $\eta$

$$\eta(a, \beta) = \frac{2\beta}{\beta^2+1} \exp \left[ \frac{-2a^2}{\omega_o^2 (\beta^2+1)} \right] \quad (\text{E.5})$$

In Figure E 1,  $2a = f\Delta\theta$  where  $f$  is the focal length of the focussing optics and where  $\Delta\theta$  is the full width angular deviation of the grating feedback light from the center wavelength. Substitution of Equation E.5 into the fundamental dispersion relation for a Littrow mounted grating<sup>269</sup>

$$\Delta\theta = \frac{2 \tan(\theta) \Delta\lambda}{\lambda} \quad (\text{E.6})$$

yields

$$\eta = \frac{2\beta}{\beta^2+1} \exp \left[ \frac{-2(f \tan(\theta) \Delta\lambda)^2}{\lambda^2 \omega_o^2 (\beta^2+1)} \right] \quad (\text{E.7})$$

It is known that<sup>270</sup>

$$I_{th} \propto \alpha + \frac{1}{2L} \ln \left( \frac{1}{R_1 R_G} \right) \quad (\text{E.8})$$

where  $I_{th}$  is the laser threshold current,  $\alpha$  represents the laser internal losses including the loss associated with the current required to achieve zero gain, and  $L$  is the laser length,  $R_1$  is the laser output facet power reflectivity and  $R_G$  is the effective grating reflectivity.

$R_G$  may be expressed as:

$$R_G = R_m^2 \epsilon \eta \quad (E.9)$$

where  $R_m$  is the mirror reflectivity  $\approx 0.95$ , and  $\epsilon$  is the Littrow mount grating efficiency  $\approx 0.70$ . Both  $R_m$  and  $\epsilon$  are nearly independent of wavelength on the scale of the present discussion. Let the following definitions be made:

$$I_o \equiv I_{th}(\lambda=\lambda_o) \quad (E.10)$$

$$I_{\Delta\lambda} \equiv I_{th} \left( \lambda = \lambda_o \pm \frac{\Delta\lambda}{2} \right) \quad (E.11)$$

$$Z_{\Delta\lambda} \equiv \frac{I_o}{I_{\Delta\lambda}} \quad (E.12)$$

which implies that

$$Z_{\Delta\lambda} = \frac{\alpha + \frac{1}{2L} \ln \left( \frac{1}{R_1 R_m^2 \epsilon \eta_o} \right)}{\alpha + \frac{1}{2L} \ln \left( \frac{1}{R_1 R_m^2 \epsilon \eta_{\Delta\lambda}} \right)} \quad (E.13)$$

where  $\eta_o$  is  $\eta(\lambda_o)$  and  $\eta_{\Delta\lambda}$  is  $\eta(\lambda = \lambda_o \pm \frac{\Delta\lambda}{2})$ .

Let  $R'$  be the current overdrive:

$$R' = \frac{I}{I_o} \quad (E.14)$$

where  $I$  is the diode laser drive current. Then if  $R' > \frac{1}{Z_{\Delta\lambda}}$  the laser oscillator modes at  $\lambda_o \pm \frac{\Delta\lambda}{2}$  will be above lasing threshold and, conversely, if  $R' < \frac{1}{Z_{\Delta\lambda}}$  those modes will be below threshold.

The optical power emitted into a mode near  $\lambda_o \pm \frac{\Delta\lambda}{2}$  is then given by

$$P_{\Delta\lambda} = \eta_D \left[ \frac{I}{I_{th}} - \frac{1}{Z_{\Delta\lambda}} \right] I_{th} \quad (E.15)$$

where  $\eta_D$  is the laser external differential quantum efficiency and where the term in brackets must be non-negative to be meaningful. In the case that  $Z_{\Delta\lambda}=1$  (ie.  $R_{\Delta\lambda}=R_o$  or  $\Delta\lambda=0$ ) it may be seen that Equation E.15 reduces to the standard formula for output versus drive current:

$$P = \eta_D (I - I_{th}) \quad (E.16)$$

Substitution yields:

$$P_{\Delta\lambda} = \eta_D \left( R' - \frac{1}{Z_{\Delta\lambda}} \right) I_{th} \quad (E.17)$$

To find the spectral width (FWHM),  $\Delta\lambda_{\frac{1}{2}}$ , of the optical power, let

$$P(Z_{\Delta\lambda_{\frac{1}{2}}}) = \frac{1}{2} P(Z_{\Delta\lambda} = 1) \quad (E.18)$$

Define

$$Z_{\Delta\lambda_{\frac{1}{2}}} = Z' \quad (E.19)$$

Substitution of Equation E.19 into Equation E.18 and evaluation gives:

$$Z' = \frac{2}{R'+1} \quad (E.20)$$

and

$$\eta_{\Delta\lambda_{\frac{1}{2}}} = \frac{1}{R_1 R_m^2 \epsilon} \exp \left[ -2L \left[ \left( \alpha + \frac{1}{2L} \ln \left( \frac{1}{R_1 R_m^2 \epsilon \eta_o} \right) \right) \frac{R'+1}{2} - \alpha \right] \right]. \quad (\text{E.21})$$

Setting the right sides Equations E.21 and E.7 equal then allows for solution for  $\Delta\lambda_{\frac{1}{2}}$ .

$$\Delta\lambda_{\frac{1}{2}} = \frac{\lambda \omega_o \left( \beta^2 + 1 \right)^{\frac{1}{2}}}{f \tan(\theta)} \left[ \left( L\alpha + \frac{1}{2} \ln \left( \frac{1}{R_1 R_m^2 \epsilon \eta_o} \right) \right) \frac{R'+1}{2} - L\alpha - \frac{\gamma}{2} \right]^{\frac{1}{2}} \quad (\text{E.22})$$

where  $\gamma$  is given by

$$\gamma = \ln \left( \frac{\beta^2 + 1}{2\beta R_1 R_m^2 \epsilon} \right) \quad (\text{E.23})$$

Several numerical values are needed for the evaluation of Equation E.22.  $\omega_o$  is calculated with use of the fundamental eigenvalue equation <sup>271</sup> for TM modes in a symmetric waveguide:

$$\tan \left( \frac{\kappa d}{2} \right) = \frac{n_2^2 \Gamma}{n_1^2 \kappa} \quad (\text{E.24})$$

where  $\kappa$  is the complex waveguide propagation constant,  $d$  is the active region thickness,  $n_2$  is the active region index of refraction, where  $\Gamma$  is given by

$$\Gamma^2 = \chi^2 - n_1^2 k_o^2 \quad (\text{E.25})$$

and where  $n_1$  is the waveguide cladding layer index of refraction,  $\chi$  is  $\frac{2\pi}{\lambda}$  in the waveguide, and  $k_o$  is given by



$$k_o = 2 \frac{\pi}{\lambda_o} \quad (\text{E.26})$$

where  $\lambda_o$  is the free-space lasing wavelength. Numerical solution of the transcendental equation E.24 gives  $\omega_o = 0.2\mu\text{m}$ . A diffraction-limited spotsize for the off-axis parabolic mirror used in the present project may be calculated to be  $\approx 0.9\mu\text{m}$ . Thus,  $\beta$  is  $\approx 4.5$ .

Numerical values for the various parameters of Equation E.22 are as follows:

$$\lambda = 1.65\mu\text{m},$$

$$\omega_o = 0.2\mu\text{m},$$

$$\beta = 4.5,$$

$$f = 35\text{mm},$$

$$\tan(\theta) = 0.56,$$

$$L = 400\mu\text{m},$$

$$R_1 = 0.26,$$

$$R_m = 0.95,$$

$$\epsilon = 0.70,$$

$$\eta_o = \frac{2\beta}{(\beta^2+1)} = 0.42,$$

$$\gamma = 2.6,$$

$$\alpha \approx 100 \text{ cm}^{-1},$$

and

$$R' = 2 \text{ to } 3.$$

Substitution into Equation E.22 gives a numerical value

$$\Delta\lambda_{\frac{1}{2}} = 1.0 \text{ to } 1.5 \text{ Angstroms.}$$

## APPENDIX F

This appendix is a source listing of the Basic language source program CAVITY. The program is documented in several OGC CH<sub>4</sub> laboratory notebooks. The most recent version of the program is located in lab book CH<sub>4</sub>-7. The uses of the program are explained in Chapter 6.

```
1  DEFINE FILE #4='X', ASC SEP
2  DEFINE FILE #5='Y', ASC SEP
3  DEFINE FILE #6='Z', ASC SEP
4  DIM M(100)
5  B$='YES'
6  K=3 1415926536/180
8  Q=0
9  DEFINE FILE #3='IMAGE', ASC SEP
10 DEFINE FILE #1='RATRAS', ASC SEP
11 DEFINE FILE #2='SPOTSZ'
12 PRINT 'INPUT TILT OF LASER TO Z AXIS (90DEGREES)'
13 INPUT H3
14 PRINT 'INPUT MAX ANGLE SEPARATION OF RAYS (DEGREES) PER RAD'
15 PRINT ' PARALLEL TO ACTIVE REGION'
16 INPUT H4,H5
18 PRINT ' DO YOU WANT RAYS DRAWN'
19 INPUT A$
20 PRINT 'DO YOU WISH RANDOM RAYS FOR 100 RAYS'
21 INPUT D$
22 PRINT 'DO YOU WISH WIDEST RAYS DRAWN'
23 INPUT G$
24 IF D$<>'YES' THEN 70
25 DEFINE FILE #7='SPOTSTAT', ASC SEP
26 PRINT 'INPUT NUMBER OF PREVIOUS SPOTSTAT POINTS TO BE BYPASSED'
27 U9=20 61
28 U8=28.88
29 INPUT R
30 REM CONSTANTS FOR GAUSSIAN IMPROVEMENT ROUTINE-ABRAMOWITZ
31 REM AND STEGUN PAGE 953 CORRECTED
32 A(0)=.98746
33 A(2)=.0039439
34 A(4)=7.474E-05
35 A(6)=-5.102E-07
36 A(8)=1.141E-07
37 P1=3.14159
40 GOTO 105
70 PRINT 'DO YOU WISH AUTOMATIC ANGLE READING FOR START PT '
71 INPUT F$
72 IF F$<>'YES' THEN 105
73 PRINT 'INPUT NUMBER OF ANGLES TO BE READ'
74 INPUT J
105 PRINT 'INPUT PARABOLA FOCAL LENGTH IN MM.'
106 INPUT F
107 REM G1 IS GAUSSIAN VARIABLE COUNTER
108 G1=1
112 PRINT 'INPUT Z COORDINATE OF GRATING'
113 INPUT Z9
114 L=0
115 PRINT 'INPUT Y0,Z0 START PTS. WITH FOCUS AT (0,0,F)'
116 INPUT Y0,Z0
125 PRINT 'INPUT X COORDINATE OF LASER FACET'
126 INPUT W7
130 XO=TAN(K*(-H3))*(Z0-F)+W7
131 IF D$='YES' THEN 191
150 IF B$<>'YES' THEN 205
180 REM
```

```
181 REM
182 REM FIND LINE 1
183 REM E0 IS END VALUE OF T
184 REM A0,B0,C0 ARE DIRECTION COSINES FOR LINE 1
189 IF F*( > )'YES' THEN 201
190 GOTO 193
191 GOSUB 5000
192 GOTO 204
193 READ H1,H2
194 GOTO 204
201 PRINT 'INPUT INITIAL RAY DIVERGENCE FROM FACET NORMAL'
202 PRINT 'PERPENDICULAR, PARALLEL TO ACT. REGION DEGREES'
203 INPUT H1,H2
204 GOSUB 3500
205 A=A0
206 B=B0
207 C=C0
208 X=X0
209 Y=Y0
210 Z=Z0
211 GOSUB 4000
212 E0=E
213 A0=A0
214 B0=B0
215 C0=C0
217 IF A*( > )'YES' THEN 240
220 FOR T0=0,E0,E0/100
225 U=X+T0*A
226 V=Y+T0*B
227 W=Z+T0*C
228 GOSUB 6000
235 NEXT T0
240 U=X+E0*A
241 V=Y+E0*B
242 W=Z+E0*C
238 REM
299 REM
300 REM FIND LINE 2
301 REM E1 IS END VALUE OF T
302 REM A1,B1,C1 ARE DIRECTION COSINES
310 X=U
311 Y=V
312 Z=W
320 S0=2*SQR(F*Z+F^2)
322 H1=X/S0
323 H2=Y/S0
324 H3=-2*F/S0
330 A=A0
331 B=B0
332 C=C0
340 GOSUB 4500
342 A1=A0
344 B1=B0
346 C1=C0
348 E1=(29-Z)/C1
355 IF A*( > )'YES' THEN 390
```

```
360 FOR T1=0,E1,E1/100
370 U=X+T1*A1
371 V=Y+T1*B1
372 W=Z+T1*C1
373 GOSUB 6000
380 NEXT T1
390 U=X+E1*A1
391 V=Y+E1*B1
392 W=Z+E1*C1
438 REM
499 REM
500 REM FIND LINE 3
501 REM E2 IS END VALUE OF T
502 REM A2,B2,C2 ARE DIRECTION COSINES
510 X=U
511 Y=V
512 Z=W
520 A=A1
521 B=B1
522 C=-C1
525 GOSUB 4000
530 X2=X
536 E2=E
540 IF A$(<>'YES' THEN 580
550 FOR T2=0,E2,E2/100
560 U=X+T2*A
561 V=Y+T2*B
562 W=Z+T2*C
563 GOSUB 6000
570 NEXT T2
580 U=X+E2*A
581 V=Y+E2*B
592 W=Z+E2*C
638 REM
699 REM
700 REM FIND LINE 4
701 REM E3 IS END VALUE FOR T
702 REM A3,B3,C3 ARE DIRECTION COSINES
710 X=U
711 Y=V
712 Z=W
730 S0=2*SQR(F*Z+F^2)
740 H1=X/S0
741 H2=Y/S0
742 H3=-2*F/S0
750 GOSUB 4500
760 A3=A9
761 B3=B9
762 C3=C9
765 E3=(TAN(K*(-H3))*(Z-F)-X)/(A3-TAN(K*(-H3))*C3)
767 IF A$(<>'YES' THEN 800
770 FOR T3=0,E3,E3/100
780 U=X+T3*A3
781 V=Y+T3*B3
782 W=Z+T3*C3
783 GOSUB 6000
```

```
6520 GOTO 193
7000 REM
7001 REM
7002 REM CREATE FILE WITH X,Z PTS. FOR GRAPHICS
7003 REM
7025 REWIND #4
7026 REWIND #5
7027 REWIND #6
7028 FOR T=1,L
7029 READ #4,U
7035 READ #6,W
7040 WRITE #1,W,U
7045 NEXT T
7099 IF D<>'YES' THEN 9999
8000 REM
8001 REM
8002 REM ROUTINE TO CALCULATE THE STANDARD DEVIATION AND FULL
8003 REM WIDTH HALF MAXIMUM (FWHM) SIZE OF THE RETURNED SPOT IF
8004 REM RANDOM (GAUSSIAN DENSITY) INITIAL ANGLES ARE USED
8005 REM
8006 REM
8009 N=100
8010 REWIND #3
8020 S6=0
8021 S7=0
8022 S8=0
8023 S9=0
8030 FOR I=1,N
8040 READ #3,X,Y
8050 S6=S6+X
8060 S7=S7+X^2
8070 S8=S8+Y
8080 S9=S9+Y^2
8090 NEXT I
8099 REM CALCULATE STANDARD DEVIATION IN VARIATES X,Y
8100 X1=SQR(N*S7-S6^2)/N
8110 X2=SQR(N*S9-S8^2)/N
8120 REM CONVERT S.D. TO FWHM DIAMETERS ASSUMING GAUSSIAN DIST
8130 X1=X1*2*SQR(-2*LOG(.5))
8140 X2=X2*2*SQR(-2*LOG(.5))
8150 PRINT ' FWHM SPOT SIZE PERP. TO JUNCTION IN MICRONS'
8160 PRINT X1
8170 PRINT ' FWHM SPOT SIZE PARALLEL TO JUNCTION IN MICRONS'
8180 PRINT X2
8190 FOR I=1,2*R
8191 IF R=0 THEN 8210
8200 READ #7,R9
8210 NEXT I
8250 WRITE #7,W7,X1
8260 WRITE #7,W7,X2
9500 DATA -35,0,-25,0,-15,0,0,0,15,0,25,0,35,0
9501 DATA -35,-20,-25,-20,-15,-20,0,-20,15,-20,25,-20,35,-20
9502 DATA -35,20,-25,20,-15,20,0,20,15,20,25,20,35,20
9999 END
```

```
790 NEXT T3
800 U=X+E3*A3
801 V=Y+E3*B3
802 W=Z+E3*C3
897 REM
898 REM FINAL PTS IN LASER FACET PLANE
899 REM
900 X4=U
901 Y4=V
902 Z4=W
999 IF D$='YES' THEN 1010
1000 PRINT X0,Y0,Z0
1001 PRINT X4,Y4,Z4
1002 PRINT
1010 WRITE #2,X0,Y0,Z0,A0,B0,C0
1011 WRITE #2,X4,Y4,Z4
1020 WRITE #3,1000*(Z4-F)/COS(K*H3),Y4*1000
1022 IF D$='YES' THEN 191
1030 IF F$='YES' THEN 6500
1050 PRINT ' DO YOU WISH NEW ANGLES'
1051 INPUT B$
1060 PRINT ' DO YOU WISH NEW STARTING PT '
1061 INPUT C$
1070 IF B$='YES' THEN IF C$='YES' THEN 115
1080 IF B$='YES' THEN IF C$<>'YES' THEN 201
1082 IF C$='YES' THEN 115
1100 IF A$<>'YES' THEN 9999
1507 GOSUB 6000
1520 REM
1521 REM
1522 REM CALCULATE LINES FOR WIDEST RAYS IN X,Z PLANE
1523 REM STARTING AT FOCUS,
1524 REM
1530 X0=0
1531 Y0=0
1532 Z0=F
1540 H1=H4
1541 IF Q>1.5 THEN 1700
1542 H2=H5
1550 GOSUB 3500
1555 X=X0
1556 Y=Y0
1557 Z=Z0
1558 A=A0
1559 B=B0
1560 C=C0
1570 GOSUB 4000
1585 FOR T4=0,E,E/100
1600 U=X+T4*A
1601 V=Y+T4*B
1602 W=Z+T4*C
1603 IF C$<>'YES' THEN 1610
1604 IF D$='YES' THEN 1610
1605 GOSUB 6000
1610 NEXT T4
1612 IF Q<.5 THEN 1620
```

```
1613 X6=U
1614 Y6=V
1615 Z6=W
1616 GOTO 1630
1620 X5=U
1621 Y5=V
1622 Z5=W
1630 H1=-H4
1635 Q=Q+1
1640 GOTO 1541
1700 REM
1701 REM
1702 REM CALC. PTS ON PARABOLA BETWEEN EXTREME RAYS IN
1703 REM XZ PLANE
1704 REM
1710 FOR T=1.1*X5,.9*X6,(.9*X6-1.1*X5)/100
1720 W=T^2/(4*F)
1725 U=T
1726 V=0
1727 GOSUB 6000
1730 NEXT T
1800 REM
1801 REM
1802 REM CALCULATE PTS ON GRATING
1803 REM
1820 FOR T=X5,X6,(X6-X5)/100
1830 W=Z9
1831 V=0
1840 U=T
1841 GOSUB 6000
1850 NEXT T
1900 GOTO 7000
3490 REM
3491 REM
3492 REM
3493 REM MISC. ROUTINES
3494 REM
3495 REM
3496 REM
3498 REM
3499 REM
3500 REM CALCULATE INITIAL DIRECTION COSINES
3501 REM
3520 H3=H3*K
3530 H1=H1*K
3540 H2=H2*K
3550 AB=COS(H1)*COS(H2)*COS(H3)-SIN(H1)*SIN(H3)
3560 B8=COS(H1)*SIN(H2)
3570 C8=COS(H1)*COS(H2)*SIN(H3)+SIN(H1)*COS(H3)
3575 H1=H1/K
3580 H2=H2/K
3585 H3=H3/K
3600 RETURN
3998 REM
3999 REM
4000 REM FIND END PT FOR T WHEN APPROACHING PARABOLA
```



```

4001 REM
4002 IF A^2+B^2>F/10000 THEN 4010
4003 E=(X^2+Y^2)/(4*F*C)-2*C
4004 GOTO 4060
4010 S0=A^2+B^2
4020 S1=2*F*C-B*Y-A*X
4030 S2=S1^2
4040 S3=S0*(X^2+Y^2-4*F*Z)
4050 E=(S1+SQR(S2-S3))/S0
4060 RETURN
4498 REM
4499 REM
4500 REM CALCULATE DIRECTION COSINES AFTER PARABOLA
4501 REM
4510 A9=(1-2*N1^2)*A-2*N1*N2*B-2*N1*N3*C
4520 B9=-2*N1*N2*A+(1-2*N2^2)*B-2*N2*N3*C
4530 C9=-2*N1*N3*A-2*N2*N3*B+(1-2*N3^2)*C
4600 RETURN
4998 REM
4999 REM
5000 REM ROUTINE TO GENERATE 100 GAUSSIAN RANDOM INIT ANGLES
5001 REM
5100 IF G1>100 THEN 1520
5300 U1=RND(J)
5310 U2=RND(J)
5320 U3=(-2*LOG(U1))^*.5*COS(2*PI*U2)
5330 U4=(-2*LOG(U1))^*.5*SIN(2*PI*U2)
5340 H1=0
5350 H2=0
5399 REM LOOP FOR IMPROVEMENT ROUTINE
5400 FOR K9=0,8,2
5410 H1=H1+A(K9)*U3^K9
5420 H2=H2+A(K9)*U4^K9
5430 NEXT K9
5440 H1=H1*U3*U8
5450 H2=H2*U4*U9
5454 REM CHECK IF INITIAL GAUSSIAN ANGLE FALLS ON MIRROR
5455 IF ABS(H1)>ABS(H4) THEN 5300
5456 IF ABS(H2)>ABS(H5) THEN 5300
5800 G1=G1+1
5900 RETURN
5998 REM
5999 REM
6000 REM ROUTINE FOR LINE DRAWING ITERATION
6002 REM
6003 WRITE #4,U
6004 WRITE #5,V
6005 WRITE #6,W
6006 L=L+1
6007 RETURN
6500 REM
6501 REM
6502 REM ROUTINE TO READ ANGLES AUTOMATICALLY
6503 REM
6510 J=J-1
6515 IF J=0 THEN 1100

```

## VITA

Richard K. DeFreez was born in Racine, Wisconsin on February 24, 1945. He received the B.S. degree (Cum Laude, Distinction) from Sonoma State University, Rohnert Park, California in January, 1980.

Mr. DeFreez was an American Physical Society Graduate Industrial Intern to the Homer Research Laboratories of the Bethlehem Steel Corporation in 1979 and 1980. He holds a patent for a remote methane sensor as a result of work conducted there. He was an Assistant Professor of Physics and Mathematics at Sonoma State University during the spring semester of 1980. He recently spent three months as a Visiting Scientist at Xerox Palo Alto Research Center where he successfully demonstrated the first cleaved-coupled-cavity phased array laser.

In September 1980, he began his studies at Oregon Graduate Center. Since that time he has coauthored several technical publications and presented papers at several conferences.

## PUBLICATIONS AND CONFERENCES

R. K. DeFreez, T. L. Paoli, M. Bernstein, and R. D. Burnham, **CW Operation of a Cleaved-Coupled-Cavity Array of Phase-Locked GaAlAs Lasers**, To be published in Electron. Lett.

R. A. Elliott, R. K. DeFreez, T. L. Paoli, R. D. Burnham, and W. Streifer, **Dynamic Characteristics of Phase-Locked Array Multiple Quantum Well Injection Lasers**, To be published in IEEE J Quantum Electron, June 1985.

R. K. DeFreez, **Remote DIAL Measurements of Methane in Coal Mines**, Optical Society of America Topical Meeting on Optical Remote Sensing of the Atmosphere, Incline Village, January 1985, Invited Paper ThB2

R. K. DeFreez, R. A. Elliott, T. L. Paoli, R. D. Burnham, and W. Streifer, **Dynamic Properties of Phased-Array Multiple Quantum Well Injection Lasers**, Technical Digest of the XIII International Conference on Quantum Electronics, 1984, Paper PD-B3

R. K. DeFreez and R. A. Elliott **External Grating-Tuned Dual-Diode-Laser Source for Remote Detection of Coal Gas Methane (A)** J. Opt. Soc. Am., **73** Dec. 1983, 1854

W. D. Egan, R. T. Boos, R. K. DeFreez, and R. L. Byer, **Remote Differential Absorption and Scattering Measurement of Methane Near a Coal Mine Working Face** Technical Digest of the Conference on Lasers and Electro-Optics, Baltimore, 1983, Paper ThK3

R. K. DeFreez and R. A. Elliott, **Laser Diode Source for Methane Detection in Coal Gas**, Technical Digest of the Conference on Lasers and Electro-Optics, Baltimore, 1983, Paper ThK2

R. A. Elliott, H. DeXiu, R. K. DeFreez, J. M. Hunt, and P. G. Rickman, **Picosecond Optical Pulse Generation by Impulse Train Current Modulation of a Semiconductor Laser**, Appl. Phys. Lett., **42**, 15 June 1983, 1012-1014

R. K. DeFreez, R. A. Elliott, J. S. Blakemore, B. I. Miller, J. H. McFee and R. J. Martin, **High-Output Room Temperature Pulsed Operation for Broad Contact InP/In<sub>0.53</sub>Ga<sub>0.47</sub>As /InP Lasers Grown by Molecular Beam Epitaxy**, J. Appl. Phys., **54**, May 1983, 2177-2182